

Proposal of extension of the CLAS12 run-group Cb (ND_3 target)

S. Niccolai^{1,2}

Institut de Physique Nucléaire d'Orsay, 91406 Orsay, France

A. Biselli¹

Fairfield University, Fairfield Connecticut 06824

C. Keith¹

Thomas Jefferson National Laboratory, Newport News, VA 23606

S. Pisano¹

INFN, Laboratori Nazionali di Frascati, 00044 Frascati, Italy

D. Sokhan¹

University of Glasgow, Glasgow, Scotland

S. Kuhn¹

Old Dominion University, Norfolk, VA 23529

¹co-spokesperson

²contact person, email: silvia@jlab.org

Abstract

The multi-dimensional mapping of the structure of the nucleon in terms of its partonic degrees of freedom is nowadays one of the main challenges of hadronic physics, and is at the core of the CLAS12 experimental program. Precise measurements of polarized parton distribution functions (PDFs) via deep inelastic scattering (DIS) give information on the spin content of the nucleon; the extraction of transverse momentum dependent distributions (TMDs) from semi-inclusive DIS (SIDIS) data provides the correlation between the transverse spin and momentum of the quarks; the generalized parton distributions (GPDs), accessible in exclusive electroproduction channels, finally, encode the interplay between the longitudinal momentum, the transverse position, and the spin of the quarks in the nucleon. An extensive experimental program geared towards the extraction of all the cited distributions is already scheduled for CLAS12, mainly on proton target. In particular, 120 days on polarized NH3 target are approved. However, in order to perform the flavor separation of PDFs, TMDs, and GPDs, measurements on neutron target, with comparable statistical precision, are necessary as well. This proposal aims at extending the running time of the approved run-group Cb, which currently requires 50 days of an 11-GeV electron beam impinging on a longitudinally polarized deuterium target (plus 15 days for target overhead and beam-polarization measurements), to 100 days of duration (plus 25 days of overhead). The driving motivations for this extension are the measurements of single and double target-spin asymmetries for deeply virtual Compton scattering on longitudinally polarized neutrons (nDVCS), of double and single spin asymmetries for SIDIS (with both pions and kaons), and double spin asymmetries for DIS on the deuteron. Considering the lower polarization of the neutron on ND3 (40%) with respect to the one of the proton in NH3 (80%) and the smaller cross sections on neutrons than on protons, the overall neutron figure-of-merit is up to a factor of 4 smaller than for the proton. At least, matching the integrated luminosity on protons with that on neutrons is necessary to perform the flavor separation of the aforementioned parton distributions, binned in the relevant kinematic variables. These data will also allow pioneering first-time measurements, such as polarized timelike Compton scattering on the neutron and deeply-virtual meson electroproduction off a polarized neutron.

Chapter 1

DIS on Longitudinally Polarized Deuterium

Proposal to increase the beam time allocation for the ND₃ part of Experiment 12-06-109
(approved by PAC 30 and rated “A” by PAC 36.)

Sebastian Kuhn^{1,2}

Old Dominion University, Norfolk VA 23529.

¹co-spokesperson

²contact person, email: skuhn@odu.edu

Abstract

We are proposing to add 50 more days of running to the 50 days already approved for the portion of Experiment 12-06-109 with CLAS12 and 11 GeV polarized electrons on longitudinally polarized deuterons (ND_3). This additional beam time (plus 10-15 days overhead) will significantly reduce the uncertainty on polarized parton distributions, in particular for d quarks, in the limit of large x , as well as for gluons and the strange quark sea at moderate to large x . It will bring the deuteron data at least closer to parity with the already approved 120 days of data on the proton, thus maximizing the information that can be extracted from a single experiment, as well as making more significant comparisons with other experiments (e.g. on ${}^3\text{He}$) possible. This will be important to assess the impact of nuclear effects on the extraction of Δd at high x , and to guarantee that the unique opportunity to finally map out the asymptotic behavior of all quark distribution provided by Jefferson Lab's 12 GeV beam will be optimally utilized. In this proposal, we are providing updated estimates of various quantities that can be extracted from these data under the assumption of a doubling for the integrated luminosity on the deuteron.

1.1 Introduction

Experiment 12-06-109 is a comprehensive program to map out the x - and Q^2 -dependence of the helicity structure of the nucleon in the region of moderate to very large x . By collecting inclusive (DIS) and semi-inclusive (SIDIS) data over a wide kinematic range with CLAS12 and 11 GeV polarized electrons on both longitudinally polarized protons (NH_3) and deuterons (ND_3), this program aims to constrain global fits of polarized parton (quark and gluon) distributions, extract higher twist corrections to the DIS structure functions, and evaluate moments connected to local operators in the Operator Product Expansion (OPE). Experiment 12-06-109 was originally approved by PAC 30 (with a further review and scientific rating of “A” by PAC 36) for a total of 80 days, 30 days on NH_3 and 50 days on ND_3 (both including overhead).

In the meantime, additional experiments on longitudinally polarized *protons* have been approved, with high rating. These experiments have brought the total number of PAC-approved days for the NH_3 target to 120 (run group Ca with CLAS12). [REF] In the meantime, the total runtime for the ND_3 target (run group Cb) has been largely unchanged (at present 65 days including all overhead for auxiliary measurements, target operations etc.). This discrepancy is even more striking when taking into account that ND_3 targets tend to have polarizations of roughly a factor 1/2 lower than NH_3 targets, resulting in an overall figure of merit (FoM) eight times worse than for the proton. This means that any analysis that requires information from both targets (e.g., global fits to extract polarized parton distributions) would have uncertainties that are totally dominated by the statistical error from the deuteron.

While some of the goals of the original experiment 12-06-109 can be reached with reasonable precision even with 50 PAC days on the deuteron, there are some physics observables whose precision would be “statistics-starved” under this scenario. In particular, the asymptotic behavior of the PDF Δd at large x would be much less constrained than what is possible with a doubling of the integrated luminosity. Deuteron data are also crucial to determine the total contribution from quark helicities to the nucleon spin ($\Delta\Sigma$), as well as polarized gluon and strange quark PDFs at moderate to large x (see details in the following sections). Because of their smaller count rates, SIDIS channels will benefit significantly from additional statistics. As we lay out in detail in the following sections, a doubling of the actual run time on polarized ND_3 from 50 to 100 days (plus the necessary overhead) will optimize the overall physics output from Experiment 12-06-109 and maximize the return on the large investment in the spin physics program with Jefferson Lab at 12 GeV. No other facility presently running or under construction will be able to probe, with comparable precision, the kinematic region of moderate to large x and moderate Q^2 accessible here.

1.1.1 The Deuteron and CLAS12

A complete mapping of spin structure functions and the extraction, through global PDF fits, of polarized parton distributions require a complete set of measurements on both types of nucleons, protons and neutrons, over the widest possible range in x and Q^2 . In addition, since neutrons can only be accessed bound in nuclei, it is very important that both commonly used nuclear targets, ${}^3\text{He}$ and deuterium, be studied with high precision, since nuclear effects and their uncertainties are very different for these two cases. Furthermore, the deuteron is the best substitute for a purely isoscalar nucleon target, which is ideal for extracting information on gluon and sea quark helicity distributions through NLO analyses. For these reasons, a high-statistics measurement on polarized deuterium (ND_3) is obligatory.

Presently, the only readily available and suitable targets for polarized protons and deuterons employ solid state compounds like ammonia, butanol or lithium deuteride at low (≈ 1 K) temperatures. These compounds are susceptible to radiation damage and beam heating, limiting severely the practically achievable luminosities. The upgraded CLAS12 detector will be a perfect match for these targets, since it

- is optimized for luminosities of $1\text{--}2 \cdot 10^{35} \text{ cm}^{-2} \text{ s}^{-1}$, within a factor of 2-4 of the practical limit of cryogenic ammonia targets, and compensates for this relatively low luminosity with its very large acceptance
- already contains a solenoidal magnet which will provide the (typically 5 Tesla) field needed for dynamic nuclear polarization, thus minimizing the extra costs of a polarized target
- covers a large angular range, including backwards angles, which allows us to simultaneously measure inclusive, semi-inclusive and tagged structure functions (with backward-going target remnants) over the full kinematic range of interest (while also collecting data for deeply virtual exclusive processes and single spin asymmetries).

Our group is leading the development of an optimized longitudinally polarized proton and deuteron target for CLAS12, and coordinates the run group C using these targets. Significant investments in this program have already been made, partially through an NSF MRI grant. No other experiment with this particular type of targets has been planned with similar kinematics, at Jefferson Lab or elsewhere. We believe that adding 60–65 more days of running to the already established run group C (an overall increase by only 25%) will yield an optimal return on this investment.

1.2 Scientific Case and Recent Developments

Inclusive and flavor-tagged spin structure functions of the nucleon have been measured for over three decades [1], beginning with the experiments at SLAC [2] and the discovery of

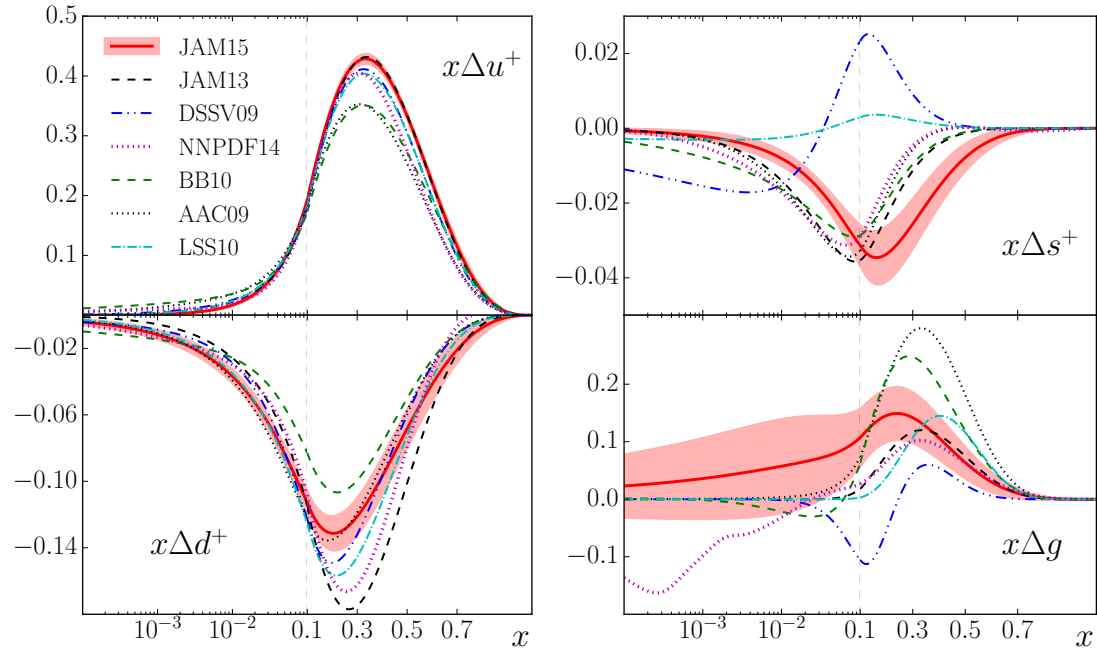


Figure 1.1: Compilation of recent polarized PDF fits from various groups. This Figure is from the JAM15 paper [5] (Fig. 17) where all references for these fits can be found.

the famous “spin puzzle” by the EMC [3]. The goal of these experiments is to determine, via next-to-leading-order DGLAP analyses, the helicity-dependent distribution functions (PDFs) of valence and sea quarks as well as gluons, see Fig. 1.1. Collinear spin structure functions can also be used to evaluate moments that are related to nucleon axial current matrix elements (e.g., the overall contribution of quark helicities to the nucleon spin), and to test fundamental sum rules like the Björken sum rule [4]. Finally, measuring their dependence on the photon virtuality Q^2 allows us to determine higher twist contributions, matrix elements in the framework of the operator product expansion (OPE), and the transition from partonic (high Q^2) to hadronic (low Q^2) degrees of freedom, including duality and tests of the Gerasimov-Drell-Hearn sum rule and its extensions in, e.g., Chiral perturbation theory (χ PT). [REFS] In the new era of three-dimensional mapping of the nucleon parton distributions, collinear spin structure functions serve both as a crucial constraint on GPDs and TMDs, and provide two of the four ingredients to the celebrated nucleon spin sum rule.

Within recent years, data from high-energy polarized proton collisions at RHIC [6, 7, 8, 9, 10] have constrained the contribution of gluon and sea quark helicities at low to moderate $x \leq 0.2$ to the nucleon spin. Further information has come from measurements of open charm production [11]. The most recent inclusive data from COMPASS [12] extend our knowledge of spin structure functions to the lowest x and highest Q^2 yet. Meanwhile, the spin structure function program with Jefferson Lab’s 6 GeV has been concluded and most results have been published. In particular, very precise data on proton, deuteron and

${}^3\text{He}$ targets [13, 14, 15, 16, 17, 18] have recently appeared that cover a large kinematic range, from low Q^2 to the DIS region. This program is being continued in the 12 GeV era, with several experiments in three halls approved with scientific rating of “A”. The unique importance of these expected Jefferson Lab data is threefold:

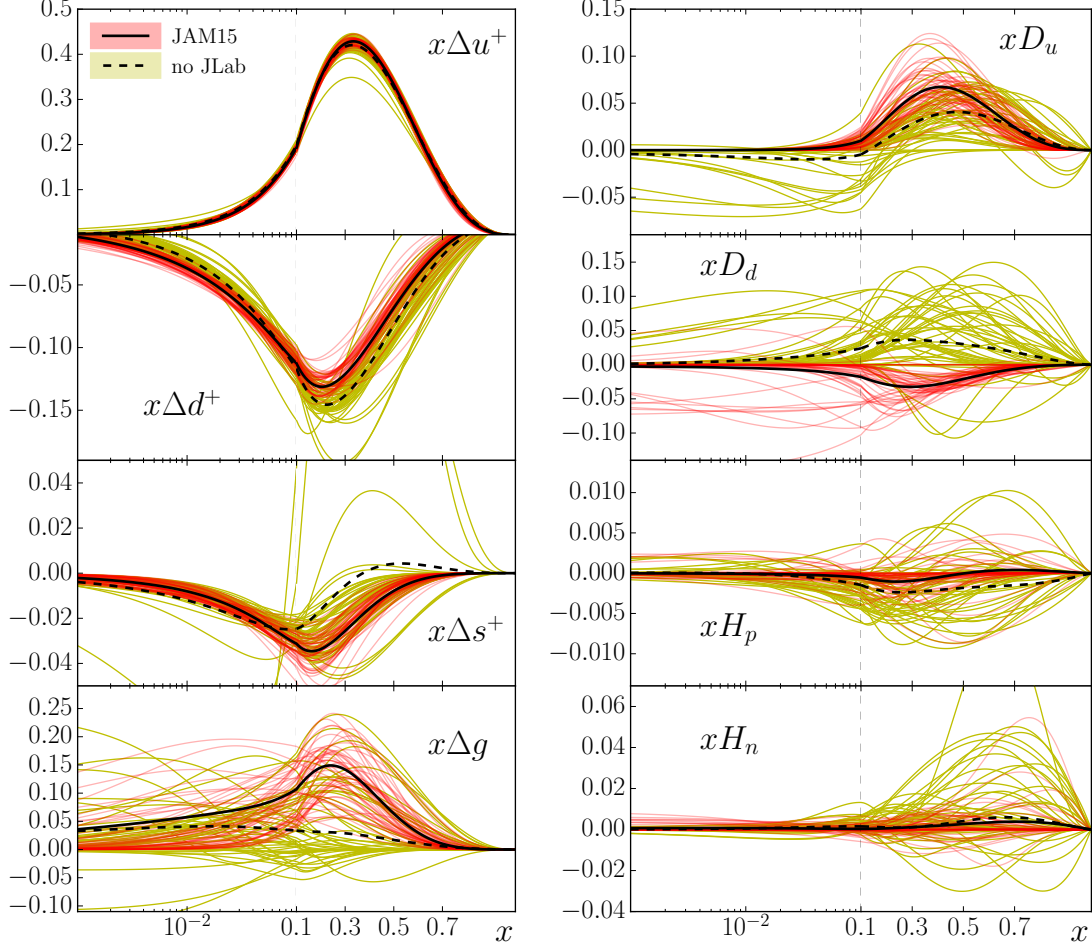


Figure 1.2: Impact of recent Jefferson Lab data on the global NLO PDF fit by the Jefferson Lab Angular Momentum (JAM) collaboration. This Figure is from the recent JAM15 paper [5] (Fig. 15) where all relevant references can be found. The l.h.s. fits are for the leading twist distributions for three quark flavors and gluons, while the r.h.s. shows the results for various higher-twist terms. The yellow lines are from repeated Monte Carlo fits including all world data except those from Jefferson Lab; the red lines include the Jefferson Lab data and clearly have a much more narrow uncertainty band.

1. For a DGLAP determination of all individual parton distribution functions, but in particular those of the gluon, from DIS data, a large leverarm in Q^2 is required to exploit scaling violations. The recent precise data from COMPASS [12] cover the

high- Q^2 limit³, while precise data at the lowest Q^2 consistent with DIS come from Jefferson Lab. The latter cover a large range in Q^2 , which in itself allows us to reliably extract and control for higher-twist effects. Figure 1.2 demonstrates the significant improvement in our knowledge of *all* polarized PDFs enabled already by the existing Jefferson Lab data.

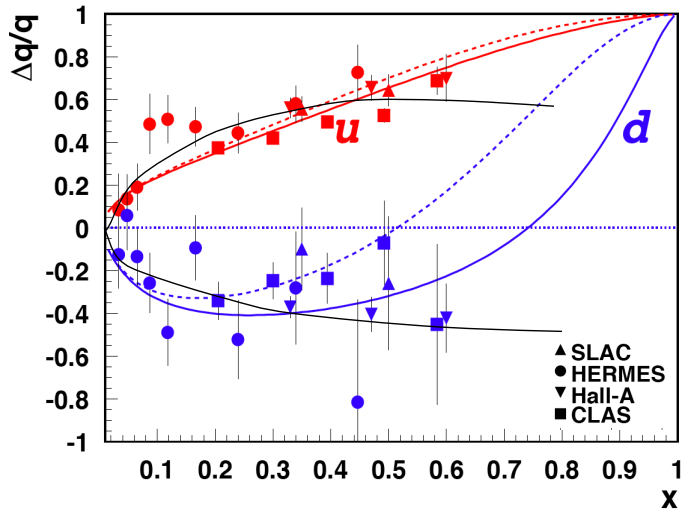


Figure 1.3: $\Delta u/u$ (upper half) and $\Delta d/d$ (lower half) results from Jefferson Lab Hall A and CLAS data (in leading order approximation), compared with other world data and three different predictions: a fit by Leader, Stamenov and Siderov [19] (black line), and two pQCD predictions without [20] (dashed) and with [21] (solid red and blue lines) inclusion of orbital angular momentum effects.

2. While the contribution from PDFs in the valence region $x > 0.3$ and, especially, in the limit $x \rightarrow 1$, to the overall nucleon spin is not very large, knowledge of PDFs in this regime is crucial to understand the valence structure of the nucleon and to test predictions from pQCD and various models. Only Jefferson Lab at 12 GeV can provide the necessary precision data in these kinematics for the foreseeable future. In particular, the asymptotic polarization of d quarks in the proton, $\Delta d/d$ at large x , is presently poorly known (see Fig. 1.3), and a reliable measurement requires high statistics data from both deuterons and ${}^3\text{He}$.
3. Beyond the leading-order PDFs, higher twist structure functions are of high current interest in themselves, since they contain information about correlations and interactions between gluons and quarks in the nucleon. Again, only at Jefferson Lab,

³These will be greatly improved upon, both in kinematic reach and in precision, by data to be acquired with the future EIC; however, the low- Q^2 data from Jefferson Lab will likely not be matched in the foreseeable future.

with its unique combination of high luminosity and moderate Q^2 , can these structure functions be studied in detail (see the r.h.s. of Fig. 1.2 for examples).

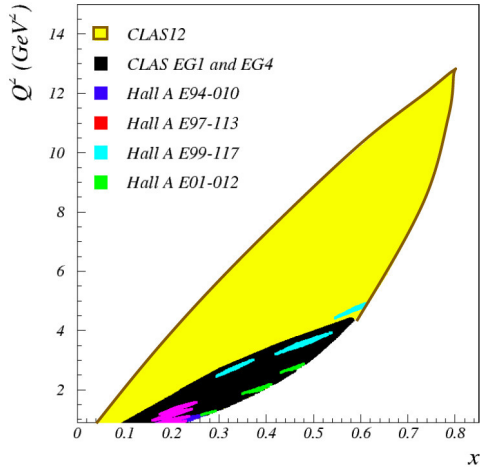


Figure 1.4: Kinematic coverage in the DIS region of existing 6 GeV JLab experiments and expected coverage for the proposed 12 GeV experiment.

Experiment 12-06-109 at 11 GeV will extend the useful x -range in the DIS region both to lower and higher x and to much higher Q^2 , compared to the existing Jefferson Lab data; see Fig. 1.4. Especially at the upper end, the expected data will still be limited in statistics; a doubling of the integrated luminosity will yield significant improvements in the information we can extract from these data, as we will show below.

1.3 Expected Results

1.3.1 PDFs

The main goal of E12-06-109 is to determine the x -dependence of each individual parton (quark *or* gluon) distribution in the region of moderate to very high x , $0.06 \leq x \leq 0.8$. This is the region most relevant to the low-energy properties of the nucleon, where valence quarks and sea quarks confined in the “meson cloud” dominate. It is also the region where measurements at RHIC and charm production at COMPASS can contribute only little but which is important to our understanding of the dynamics that impart a net polarization to the “valence-like” sea quarks and gluons at high x .

Figure 1.5 shows the expected improvement for the uncertainties on up, down, and strange quark polarizations as well as the gluon polarization from E12-06-109. The blue lines show the improvement due to just the proton data from the presently allocated beam time (120 days on NH_3), while the green lines show the further reduction in those uncertainties due to the expected deuteron data as approved (45 days on ND_3). Finally, the red

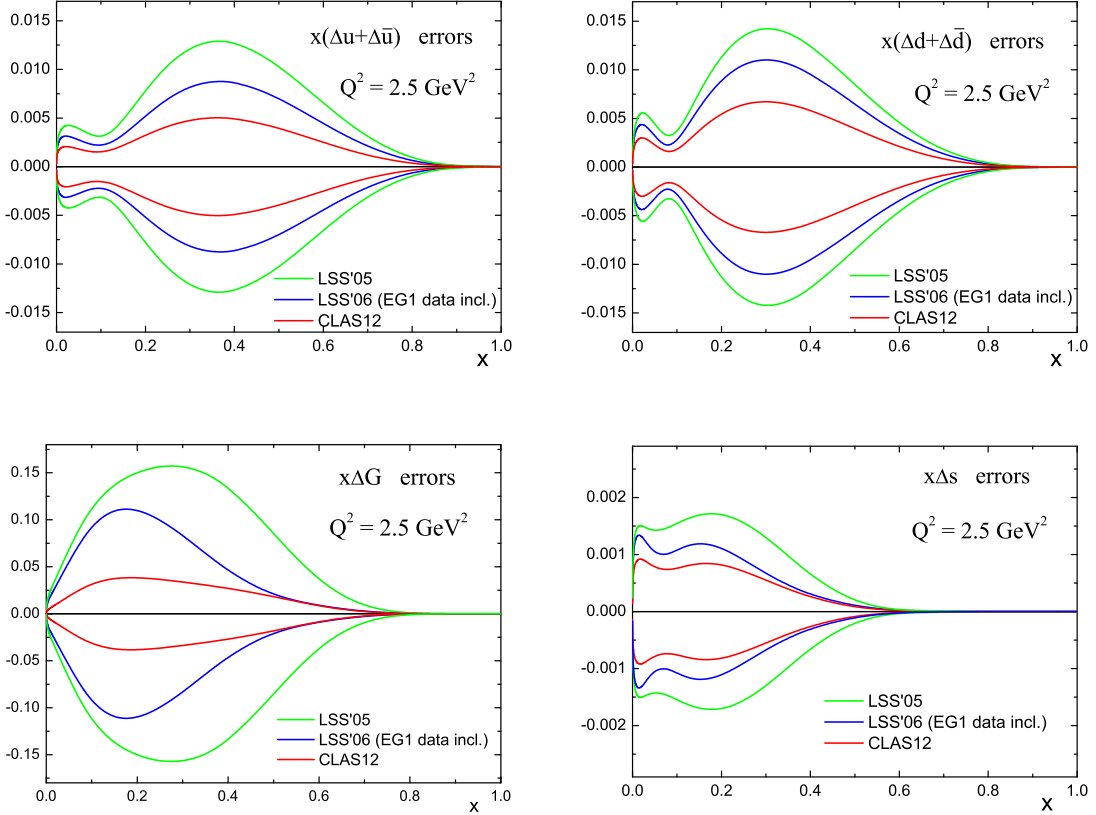


Figure 1.5: Expected effect on the uncertainty for various polarized parton distribution functions after inclusion of E12-06-109 data, according to an up-to-date analysis by the JAM collaboration (courtesy of N. Sato). The blue lines indicate the reduction factor for the present uncertainties (see Fig. 1.2) from the already approved 120 days of NH₃ only, while the green and red lines show the additional reduction from combining these data with either the already approved 45 days for ND₃ (green), or with double that run time (red).

lines show how the impact of collected twice the statistics on the deuteron, as proposed here. It is clear that the biggest improvement from the deuteron data will be in our knowledge of the down quark polarization (see bottom left panel of Fig. 1.5). This is also the case where doubling the beam time has the largest impact, reducing the uncertainty on δd by roughly a factor 3/4 in the moderate to high x region. However, as Fig. 1.5 shows, nearly all polarized PDFs will benefit from the additional beam time requested here.

It is important to clarify that the total uncertainty on the deuterium data points is largely driven by accumulated statistics. The most important systematic uncertainty will be the normalization of the data due to the product of beam and target polarization and due to the dilution factor. Both of these quantities will be determined experimentally (directly - for the polarization - or indirectly through auxiliary measurements). In particular, the polarization product $P_b P_t$ will be extracted from a measurement of the exclusive $D(e, e' p)n$ reaction, for which the expected double-spin asymmetry is very well known and sophisticated models for final state interactions exist (which our group has tested experimentally [23]). Due to the somewhat small magnitude of this asymmetry (driven by the requirement of low Q^2 to get reasonable count rates), this measurement requires high statistics. Data will be taken simultaneously with DIS and other channels, meaning that the the uncertainty in $P_b P_t$ will decrease proportional to that in the measured structure functions. Similarly, the dilution factor will be determined using sophisticated models of electron scattering from the various nuclear components of the target; however, some normalization factors (e.g., overall target density of the various species) have to be taken from precise measurements on auxiliary targets. These measurements will gain the same improvement in statistics as the main measurements on ND_3 .

1.3.2 Quark polarization at high x

In Figure 1.6, we focus on the impact our proposed data will have on the determination of the d-quark polarization at the highest x reachable with Jefferson Lab at 12 GeV. The “expected data points” are based on a detailed Monte Carlo simulation of the measured asymmetries on the proton and the deuteron, including both statistical and systematic uncertainties. While we used a simple-minded LO (“naïve parton model”) calculation to extract the valence quark polarizations from these measurements, the expected uncertainty will not change much with a more sophisticated analysis like the JAM PDF fit described above. The obvious point from this figure is that, as presently scheduled, our expected data will have limited statistical power to definitely answer the question (by themselves) whether $\Delta d/d$ remains negative for $x \rightarrow 1$ as expected from some NLO fits [19] and from hyperfine-perturbed quark models [22] or whether it will converge to +1 as expected by pQCD, as indicated in the solid curves in Fig. 1.6. In particular, the two last data points are only 3.7 and 1.2 standard deviations from zero, so with a statistical fluctuation of the actually measured data points by only one standard deviation, the solid curve in Fig. 1.6 would still be (nearly) compatible with those data, with a χ^2 of 4.9 for two degrees of freedom ($p = 8.7\%$).

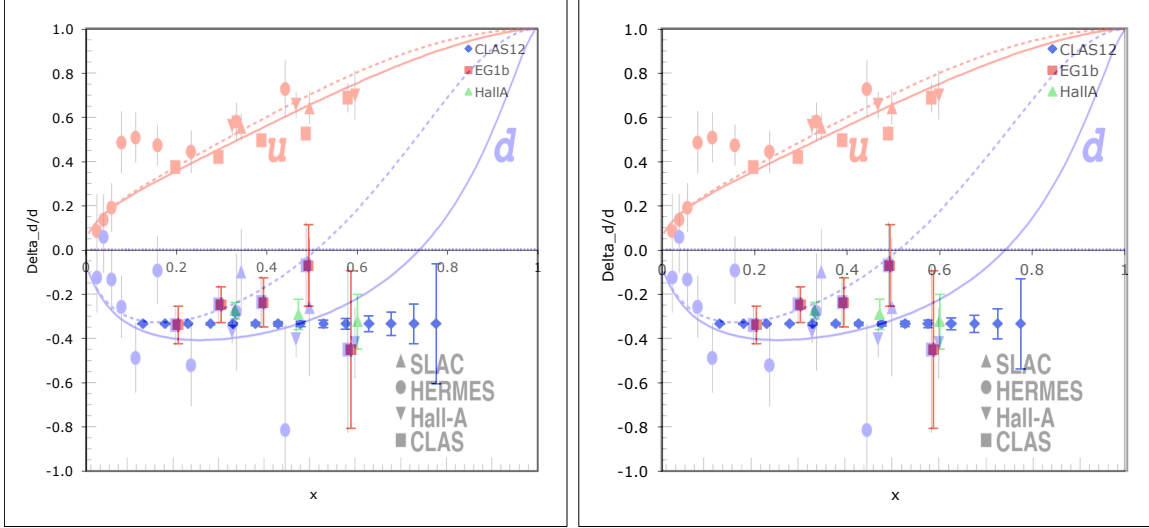


Figure 1.6: Expected statistical precision for the polarization of d quarks, $\Delta d/d$, versus x , extracted from E12-06-109 as approved (l.h.s.) and with an additional 50 days of beam time on the deuteron (r.h.s.). Existing data are shown lightly shaded (squares are from CLAS at 6 GeV) while the expected data are shown as blue diamonds. The two curves are the expectations from pQCD without [20] and with [21] inclusion of orbital angular momentum effects. The expected data are placed according to expectations from hyperfine-perturbed quark models [22] which, at least at present, cannot be ruled out.

With a doubling of the integrated luminosity on the deuteron, the statistical error bars on $\Delta d/d$ will go down nearly exactly by a factor of $1/\sqrt{2}$, since the proton results (that also enter the calculation) are already vastly more precise than the deuteron ones. As stated above, the systematic uncertainties will also go down, by nearly the same amount (and the uncertainties are statistics-dominated at high x). Repeating the same calculation, we find that the agreement with the “wrong” curve is now much worse, with a χ^2 of 11.3 for two degrees of freedom ($p = 0.35\%$). While it is true that more information on $\Delta d/d$ is expected from the approved experiments on ${}^3\text{He}$, it is precisely at high x that smearing effects and uncertainties from nuclear binding become the largest, making an independent measurement on the most lightly bound nucleus, deuterium, mandatory. Our proposal for an additional 50 days on that target will strengthen this independent result significantly.

1.3.3 Further results from SIDIS

In addition to the determination of polarized PDFs from inclusive DIS measurements, run group C also supports a large number of approved measurements with semi-inclusive detection of pions and Kaons. For example, we show in Fig. 1.7 the expected results from a combination of SIDIS production of pions (π^+ and π^-) from both proton and deuteron targets that directly measures (in LO) the valence d-quark polarization. This figure is from

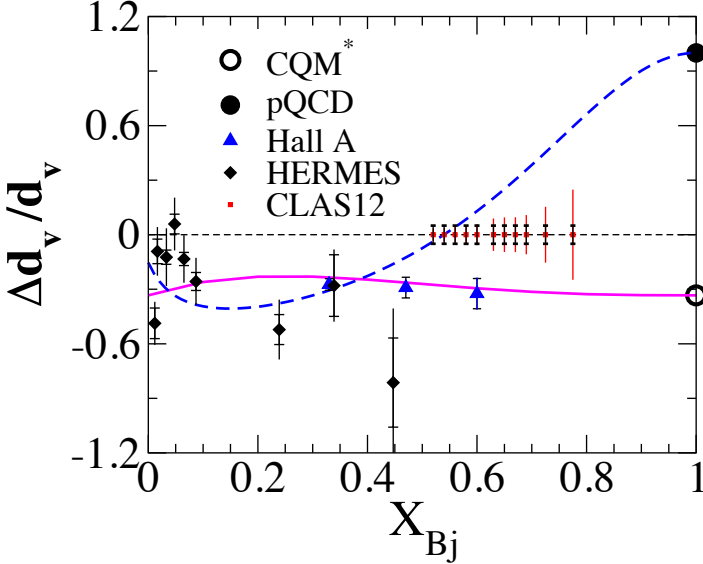


Figure 1.7: Expected results for the valence d quark polarization from semi-inclusive data with the proposed experiment, as well as existing data. The horizontal risers indicate the systematic uncertainties (!), while the length of the error bars indicates the statistical uncertainties. The dashed line represents a pQCD prediction [20] while the solid line represents the prediction from the hyperfine perturbed constituent quark model [22].

the original proposal for E12-06-109 and hasn't been updated yet, but it is clear that similar arguments as for the previous subsection apply: A reduction of the statistical error bars (indicated by the *full* length of the vertical lines) by a factor $1/\sqrt{2}$ would turn this marginally significant measurement into a strong, independent confirmation for the trend observed in DIS.

More generally, a combined analysis of all inclusive and semi-inclusive measurements within the framework of NLO DGLAP analysis will further constrain the individual quark and gluon PDFs and allow a clear separation of quark and antiquark contributions of each flavor to the sea. The JAM collaboration is now gearing up to include this information in their fits, carefully assessing the impact of our (lack of) knowledge of the required fragmentation functions. While simulations are not yet available, it is clear again that higher precision will translate in additional knowledge. As an example we consider (in Fig. 1.8) the impact of various measurements on our knowledge of the strange quark sea in the nucleon, which is still a contentious topic without a clear consensus whether the contribution of this strange sea to the nucleon spin is positive, negative or negligible.

The top row of Fig. 1.8 shows that the K^+ asymmetry (on either target) and the K^- asymmetry on the proton are rather insensitive to the strange quark polarization, since in both cases u-quarks dominate because of their prevalence and larger charge. However, the K^- asymmetry on the deuteron is much more sensitive to strange quarks, since in the deuteron, u and d quark contributions to K^- production fortuitously cancel to a large

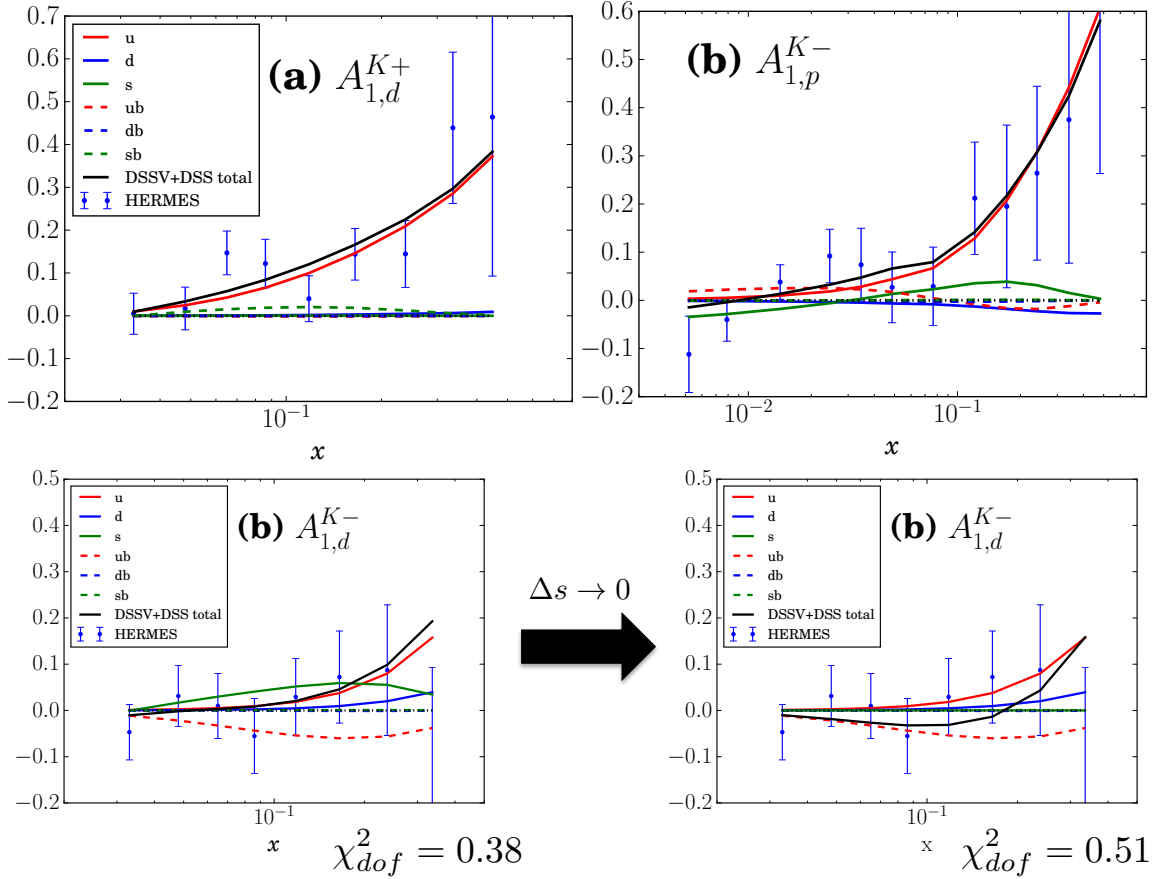


Figure 1.8: Contributions to the measured asymmetry in SIDIS Kaon production from various quark (solid lines) and anti-quark (dashed lines) flavors, according to a preliminary JAM analysis. The data points are from HERMES. The top row shows the K^+ asymmetry on the deuteron (l.h.s.) and the K^- asymmetry on the proton (r.h.s.). The bottom row shows two fits to the K^- asymmetry on the deuteron, either with the s-quark contribution allowed to vary freely for a minimized χ^2 (left) or with this contribution set to zero (right). Figure courtesy of J.J. Ethier.

extent. Hence, a precise measurement of this channel down to the lowest available $x \approx 0.06$ at Jefferson Lab has great promise to answer the question whether strange quarks in the nucleon carry positive helicity, negative helicity or whether there is a node in the distribution where their polarization transitions from plus to minus. Unfortunately, the only data existing so far (from HERMES) have large error bars, so that an alternative fit without any s-quark contribution only increases the χ^2 per degree of freedom from 0.38 to 0.51 (see bottom row of Fig. 1.8). With the vastly better statistics available from CLAS12, this situation should be much improved (note that CLAS12 will cover the same kinematic region as HERMES except for the two lowest data points). The importance of finally “nailing down” this least-known quark contribution to the nucleon spin is another strong justification to collect the highest statistics data set on the deuteron possible.

1.4 Beam Request

We request 50 additional days for a total of 100 days of 11 GeV longitudinally polarized ($> 85\%$) electrons on a longitudinally polarized ND₃ target in CLAS12 (total luminosity 2×10^{35} nucleons×electrons/cm²/s), plus 15 additional days for a total of 30 days at various beam energies for calibration, in-situ irradiation of the target material, target changes, anneals and polarization reversals, as well as beam polarization (Møller) measurements.

(To be harmonized with the other RG proposals).

Bibliography

- [1] S. E. Kuhn, J. P. Chen and E. Leader, Prog. Part. Nucl. Phys. **63**, 1 (2009), hep-ph/0812.3535.
- [2] M. J. Alguard *et al.*, Phys. Rev. Lett. **37**, 1261 (1976). G. Baum *et al.*, Phys. Rev. Lett. **51**, 1135 (1983).
- [3] J. Ashman *et al.* [EMC Collaboration], Nucl. Phys. **B328**, 1 (1989).
- [4] J. D. Bjorken, Phys. Rev. **179**, 1547 (1969). J. R. Ellis and R. L. Jaffe, Phys. Rev. **D 9**, 1444 (1974), Erratum Phys. Rev. **D 10**, 1669 (1974).
- [5] N. Sato, W. Melnitchouk, S.E. Kuhn, J.J. Ethier, and A. Accardi, Phys. Rev. **D 93**, 074005 (2016).
- [6] L. Adamczyk *et al.*, Phys. Rev. Lett. **115**, 092002 (2015).
- [7] A. Adare *et al.*, Phys. Rev. D **90**, 012007 (2014).
- [8] A. Adare *et al.*, arXiv:1510.02317 [hep-ex].
- [9] L. Adamczyk *et al.*, Phys. Rev. Lett. **113**, 072301 (2014).
- [10] A. Adare *et al.*, arXiv:1504.07451 [hep-ex].
- [11] C. Adolph *et al.*, Phys. Rev. D **87**, 052018 (2013).
- [12] C. Adolph *et al.*, Phys. Lett. B **753**, 18 (2016).
- [13] N. Guler *et al.*, Phys. Rev. C **92**, 055201 (2015).
- [14] R. G. Fersch, N. Guler, P. Bosted, A. Deur, K. Griffioen, S. E. Kuhn, R. Minehart, Y. Prok *et al.* [CLAS Collaboration]: “Precise determination of proton spin structure functions at low to moderate Q^2 with CLAS”, to be published in Phys. Rev. C (2016).
- [15] Y. Prok *et al.*, Phys. Rev. C **90**, 025212 (2014).
- [16] D. S. Parno *et al.*, Phys. Lett. B **744**, 309 (2015).

- [17] M. Posik *et al.*, Phys. Rev. Lett. **113**, 022002 (2014).
- [18] P. Solvignon *et al.*, Phys. Rev. C **92**, 015208 (2015).
- [19] E. Leader, A. V. Sidorov and D. B. Stamenov, Phys. Rev. D **75**, 074027 (2007), preprint hep-ph/0612360; Eur. Phys. J. ST **162** (2008) 19.
- [20] S. J. Brodsky, M. Burkardt and I. Schmidt, Nucl. Phys. **B441**, 197 (1995), preprint hep-ph/9401328.
- [21] H. Avakian, S. J. Brodsky, A. Deur and F. Yuan, Phys. Rev. Lett. **99**, 082001 (2007), preprint hep-ph/0705.1553.
- [22] N. Isgur, Phys. Rev. D **59**, 034013 (1999), preprint hep-ph/9809255.
- [23] M. Mayer *et al.* (CLAS collaboration), “Beam-target double spin asymmetry in quasi-elastic electron scattering off the deuteron with CLAS”, paper presently under CLAS AHC review.

Chapter 2

Semi-Inclusive Deep Inelastic Scattering on a longitudinally polarized deuterium target

S. Pisano^{1,2}

INFN, Laboratori Nazionali di Frascati, 00044 Frascati, Italy

S. Niccolai¹

Institut de Physique Nucléaire d'Orsay, 91406 Orsay, France

A. Biselli¹

Fairfield University, Fairfield Connecticut 06824

C. Keith¹

Thomas Jefferson National Laboratory, Newport News, VA 23606

D. Sokhan¹

University of Glasgow

¹co-spokesperson

²contact person, email: pisanos@jlab.org

Abstract

A comprehensive program to study Transverse Momentum Dependent distribution functions is foreseen for CLAS12. In particular, the E12-07-107 and E12-09-009 experiments aim to access the valence-quark transverse and longitudinal spin distributions through measurements of spin-azimuthal asymmetries in semi-inclusive electroproduction of pions and kaons. They will make use of the upgraded JLab 11 GeV polarized electron beam and the CLAS12 detector with longitudinally polarized proton and deuteron targets. The use of different targets, in conjunction with the detection of various hadrons in the final state, provides access to information about the flavor of the struck quark. As of today, 120 days of beam time are approved for longitudinally polarized proton target (NH_3), but only 50 for the deuteron one (ND_3). This proposal requests the addition of 50 more days to the CLAS12 Run group Cb (ND_3 target). This will be particularly beneficial for the high- p_T region, especially for the k^- channel, where the existing models are less constrained and their predictions for the SIDIS target-spin asymmetries differ the most. Furthermore, an increased statistics on ND_3 will permit to measure, for the first time, the semi-inclusive production of hadron pairs on longitudinally polarized deuterium. This can provide a unique access to the poorly known chiral-odd PDFs, which can then be separated according to their flavor via the combination with the results obtained on proton and deuteron targets.

2.1 Toward a multi-dimensional mapping of nucleon structure

The Transverse Momentum Dependent distribution functions (TMDs) provide a description of nucleon structure which is complementary to the one that can be obtained measuring Generalized Parton Distributions: the latter describe the correlation between the longitudinal momentum and the transverse position of the parton, while the former encode both the longitudinal and the transverse momenta of the parton. Thus, the TMDs share with the GPDs the dependence on the parton longitudinal momentum fraction, providing the additional information on its transverse momentum k_T . The TMDs can be accessed through the semi-inclusive electroproduction of hadrons (**SIDIS**), *i.e.* the process where an electron scatters off a nucleon producing a hadron in the final state. In an intuitive picture, the final hadron carries information on the original dynamics of the struck quark, so that mapping the hadron kinematics provides information on the parton motion inside the nucleon. In the SIDIS cross section different structure functions (SF) are introduced, each being accessible through specific combinations of the polarizations of beam and target. Any SF contains two non-perturbative objects: the TMDs, encoding the parton dynamics in the nucleon, and the so-called Fragmentation Functions (**FF**), that describe the transition from the partonic degrees of freedom to the hadronic ones, *i.e.* the hadronization process. FFs and TMDs are coupled in a convolution integral over the quark transverse momentum, making the final TMD extraction model dependent through the assumptions on the (not measurable) k_T dependence.

At leading twist, the parton dynamics is described by eight **TMDs**, each one related to a specific combination of parton/hadron polarization, as shown in Table 2.1. The diagonal elements of the table are the momentum, the longitudinal and transverse spin distributions of partons, and represent well-known parton distribution functions related to the square of the leading-twist, light-cone wave functions. Off-diagonal elements require non-zero orbital angular momentum and are related to the overlap of light-cone wave functions with $\Delta L \neq 0$ [2]. The parton distributions f_{1T}^\perp and h_1^\perp represent the imaginary parts of the corresponding interference terms, while the functions g_{1T} and h_{1L}^\perp represent their real parts. The TMDs f_{1T}^\perp (chiral-even) and h_1^\perp (chiral-odd) are known as the Sivers and Boer-Mulders functions, respectively [4, 5, 6, 7, 1, 3]. They describe unpolarized quarks in the transversely polarized nucleon and transversely polarized quarks in the unpolarized nucleon respectively. They vanish at tree-level in a T -reversal invariant model (T -odd) and can only be non-zero when initial or final state interactions cause an interference between different helicity states. These functions parametrize the correlation between the transverse momentum of quarks and the spin of a transversely polarized target or the transverse spin of the quark, respectively. They both require orbital angular momentum, as well as non-trivial phases from the final state interaction, that survive in the Bjorken limit.

As for the GPDs, also for the TMDs CLAS12 foresees a comprehensive program, including measurements of different observables with different targets and polarization degrees

N/q	U	L	T
U	f_1		h_1^\perp
L		g_1	h_{1L}^\perp
T	f_{1T}^\perp	g_{1T}	$h_1 h_{1T}^\perp$

Table 2.1: Leading-twist Transverse Momentum Distributions. Different rows and columns correspond, respectively, to different quark and nucleon polarization states.

of freedom. Furthermore, the detection of different hadron channels allows to tag the flavor of the struck quark, opening the avenue to a deeper understanding of the nucleon content and on the hadronization mechanism.

2.1.1 Scientific case

In the experiment proposed here, which requires to extend by 50 days the already approved experiment E12-09-009, the simultaneous presence of a longitudinally polarized beam and a longitudinally polarized target allows the measurement of longitudinal target and double-spin asymmetries (A_{UL} and A_{LL} respectively). In these asymmetries, a number of relevant TMDs appear:

$$\sigma_{UU} \propto F_{UU} \propto f_1(x, k_\perp) D_1(z_h, p_\perp) \quad (2.1)$$

$$\sigma_{UL} \propto F_{UL} \propto h_{1L}(x, k_\perp) H_1^\perp(z_h, p_\perp) \quad (2.2)$$

$$\sigma_{LL} \propto F_{LL} \propto g_{1L}(x, k_\perp) D_1(z_h, p_\perp) \quad (2.3)$$

where $z = P_1 \dot{P}_h / P_1 \dot{q}$ is the fraction of the virtual photon energy carried by the final hadron, k_\perp and p_\perp are the quark transverse momenta before and after the interaction with the virtual photon, P_1 and P_h are the four momenta of the initial nucleon and the observed final-state hadron, respectively. The unpolarized (D_1) and polarized (H_1^\perp) fragmentation functions depend in general on the transverse momentum of the fragmenting quark. For the longitudinal target spin asymmetry, the leading-twist modulation is a $\sin 2\phi$ moment, that provides access to the Kotzinian function h_{1L}^\perp , *i.e.* the T-even counterpart of the Boer-Mulders function. The same distribution function is also accessible in double-polarized Drell-Yan production. It describes the correlations of the transverse spin and momentum of quarks in a longitudinally polarized nucleon and, being an off-diagonal element, requires a non-zero orbital angular momentum to be non vanishing. Moving beyond the leading-twist approximation, a second, twist-3 modulation is expected in A_{UL} . It can be accessed as a $\sin \phi$ moment, and provides access to a combination of different TMDs and FFs. The simultaneous extraction of leading and higher-twist modulations in the observables at the CLAS12 kinematics will play an essential role in sizing effects beyond the leading twist. The CLAS12 kinematic coverage, indeed, is characterized by a Q^2 value laying in a region where possible higher-twist phenomena are still active.

Double-spin asymmetry A_{LL} is proportional to the diagonal TMD $g_1(x, k_\perp)$, that reduces

to the 1D helicity distributions once the k_\perp dependence is integrated out. Measurements of the P_T dependence of A_{LL} for different hadron channels will provide access to widths in transverse momentum for different flavors. Also interesting is the exploration of the Collins mechanism, encoded in the FF that appears coupled to h_{1L}^\perp in A_{UL} . In the so-called u -quark dominance scenario, where the fragmentation is led by the dominant flavor in the nucleon, similar results would be expected from pion and kaon fragmentation. However, the available results from HERMES (and COMPASS) on kaons do not confirm this scenario, with a signal for positive kaons being larger than for pions, while for negative kaons they are compatible. The kaon signals are a challenge for the present understanding of the underlying physics processes. Detailed studies require disentanglement of the different contributions, which is possible only with high-precision mapping of the kinematical dependences. The surprising and controversial pattern of azimuthal asymmetries for kaons is an indication of a non trivial role of the sea quarks in the nucleon, or of a peculiar behaviour of the fragmentation mechanism in the presence of strange quark.

In order to shed light on the hadronization mechanism, a high-precision mapping of the kinematic dependences, in conjunction with a excellent hadron identification will be mandatory. Furthermore, measurements for different hadron channels (that allow to tag the flavor of the decaying quark) on different targets will allow to extract different combinations of TMD and favored/unfavored fragmentation functions.

2.1.2 Channel selection and data analysis

The process of interest is the semi-inclusive electroproduction of a single hadron, *i.e.*

$$e(k)d(p) \Rightarrow e(k')h(P)X \quad (2.4)$$

The electron scatters off the deuterium through the exchange of a virtual photon. The latter interacts with one of the nucleon partons (a quark, in the CLAS12 kinematics) that eventually hadronizes through a fragmentation process producing the hadron h in the final state.

Particle identification will mainly exploit the forward detectors of CLAS12. Electrons will be identified through the calorimeter system (PCAL + EC), the time of flight and the high-threshold Cherenkov counter, and the tracking information will come from the Drift Chambers. Charged pions will be identified through the combination of tracking, time-of-flight and Cherenkov counter information. The neutral pions will be reconstructed through their two-photon decays, exploiting information from the calorimeters. In order to get a reliable particle identification in the kinematical region of interest, the use of the RICH detector will be mandatory, being the complementary PID system of CLAS12 not efficient in the kinematics proper of SIDIS hadrons (see, e.g., Fig. 2.2). The final sample will be selected applying deep-inelastic cuts ($Q^2 > 1 \text{ GeV}^2$, $W > 1 \text{ GeV}$) to select a regime where scaling is already at work and to exclude possible contributions from nucleon resonances. Contamination from target-fragmentation hadrons will be removed by applying a cut on

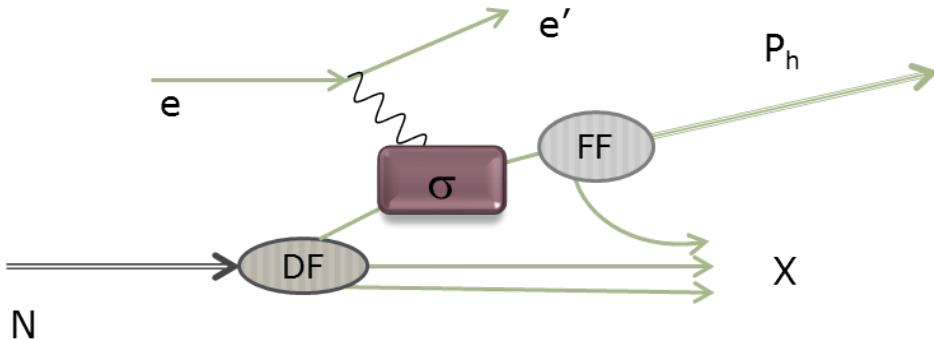


Figure 2.1: Semi-inclusive electro-production of a hadron h . The box labeled σ represents the hard part of the cross-section, described by quantum electrodynamics. The soft, non-perturbative blob represents the distribution functions (DF) that describe the dynamics of the partons in the nucleon (DF=TMD in the SIDIS case), while FF represent the hadronization of the struck quark to the final hadron.

the fraction of the virtual photon energy carried by the hadron, z , that will also remove contributions from the exclusive channels. At 6 GeV the typical z cuts were $0.4 < z < 0.7$, the lower one removing contamination from delta-mediated decays and the higher one from residual exclusive events. As an example, in Fig. 2.3 the distribution of $m_{e^- \kappa^+ X}$ is shown as a function of the z of the positive kaon. The contribution from exclusive events, peaking at the nucleon mass, appears clearly visible in the high- z region and will be removed through the above-mentioned upper cut on z .

The relevant variables for mapping single and double spin asymmetries are the ones describing the electron kinematics, (x_B, Q^2) , the hadron transverse momentum P_T and the fraction of the virtual-photon energy carried by the hadron z . The latter appear in the fragmentation functions, and are proper to the hadronization process. Distributions on p_T for positive and negative pions are shown in Fig. 2.5: left plot refers to the positive kaons, while right plot to negative. In order to extract the relevant azimuthal modulations, the asymmetries will be measured as a function of the angle ϕ , formed by the leptonic and hadronic planes, shown in Fig. 2.4 and defined according to the Trento Conventions. The acceptance in ϕ for charged kaons is shown in the two upper plots of Fig. 2.5. The left plot shows the ϕ distribution for positive kaons, while the right one refers to negative kaons.

2.1.3 Projections

The projections in this section are based on a full simulation of inclusive and semi-inclusive inelastic scattering with the CLAS12 acceptance folded in. Events were generated with the clas12DIS generator [9], an implementation of the LUND Monte Carlo package PEPSI (Polarized Electron-Proton Scattering Interactions) [8]. It is based on polarized and unpolarized parton distribution functions and the LUND string model for hadronization. It has

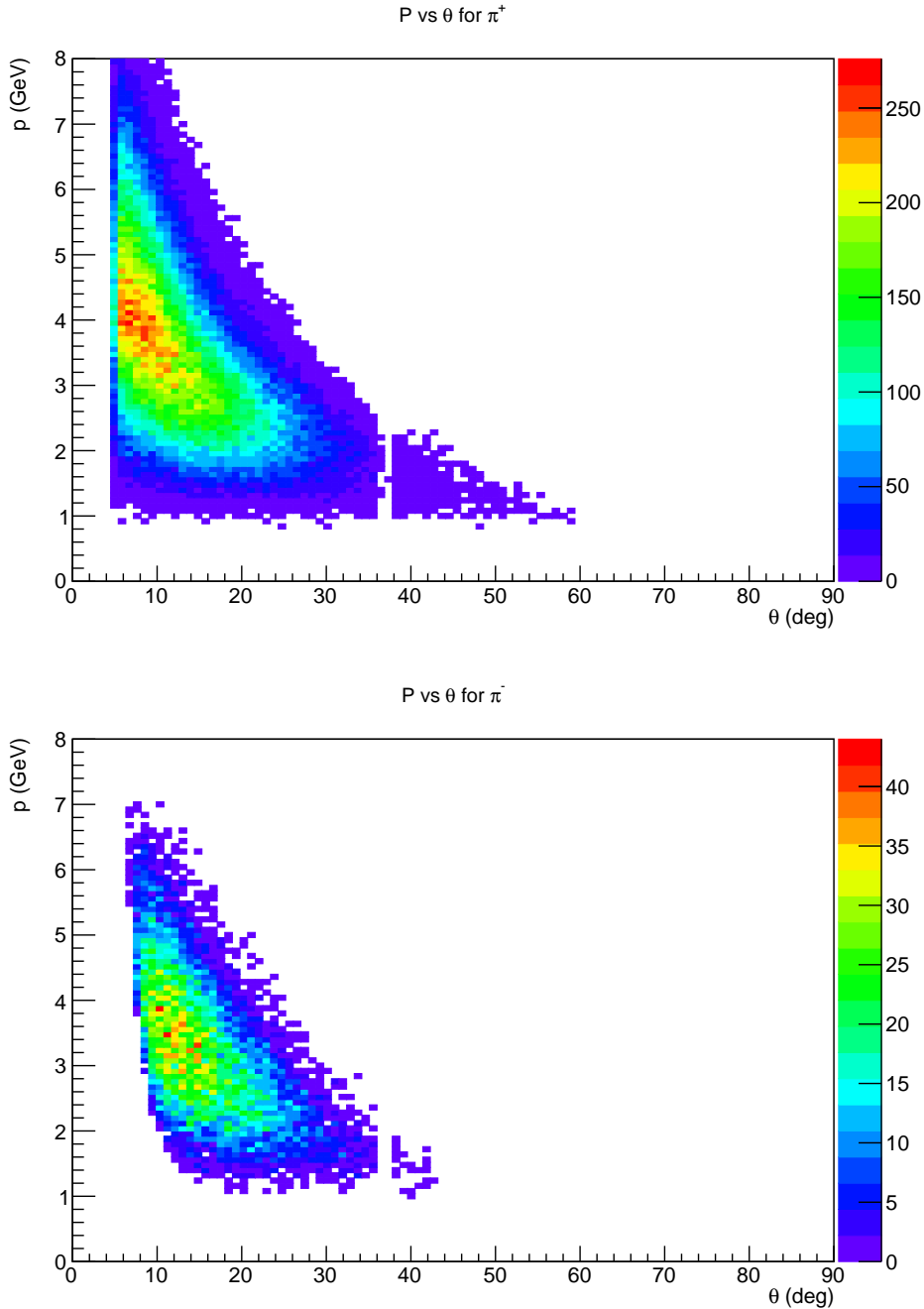


Figure 2.2: P v.s. θ for positive (top plot) and negative (bottom plot) kaons. The distributions are produced by selecting SIDIS kaons as described in Sec. 2.1.2.

$e^- \kappa^+ X$ missing mass

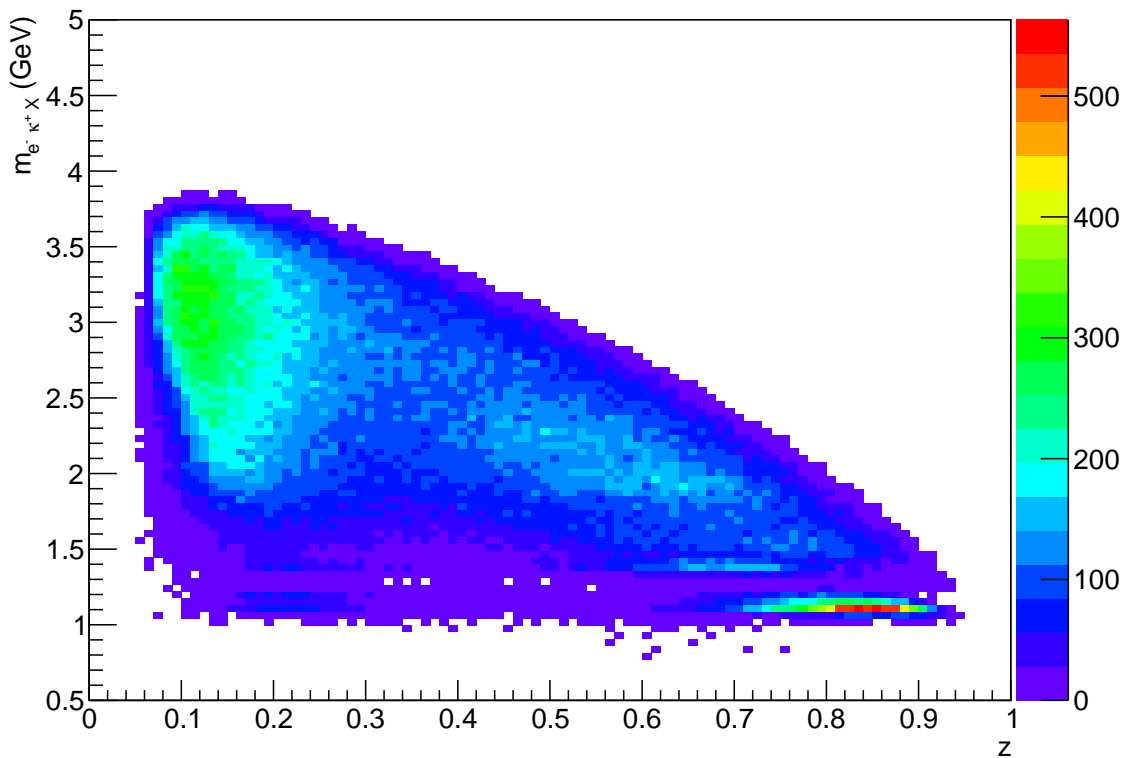


Figure 2.3: Distribution of the $e^- \kappa^+ X$ missing mass as a function of z of the positive kaon. The contribution from the exclusive peak appears clearly in the high- z region.

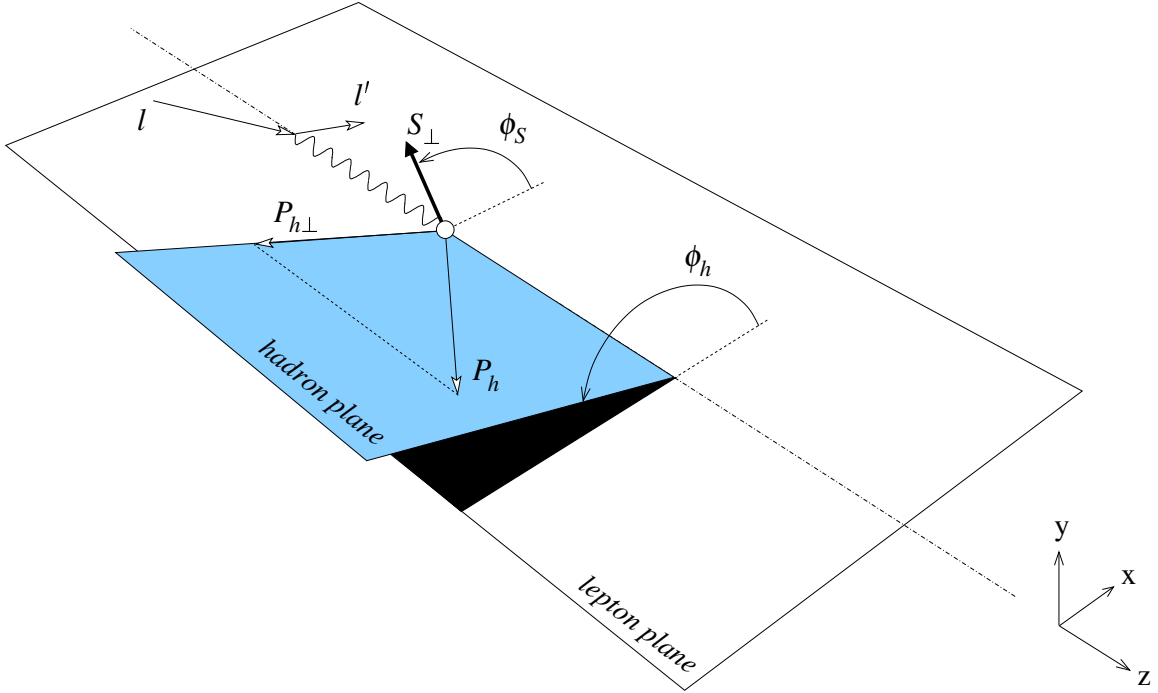


Figure 2.4: Definition of the angle ϕ , formed by the leptonic and the hadronic planes.

been tested successfully against several low- Q^2 experiments with 5.7-GeV beam at Jefferson Lab.

A fast Monte Carlo simulation program has been used to define the acceptance and resolution of the CLAS12 detector with all of the standard (base) equipment in place. The kaons were assumed identified 100% in sectors covered by the CLAS12 RICH, and also at energies above 5 GeV, where the pions start to fire the High Threshold Cherenkov Counter (HTCC). The events generated by `clas12DIS` are used as input and all particles are followed through all detector elements. The results of this simulation have been cross-checked with direct cross-section calculations and a simple geometric acceptance model. The resolution of the detector is simulated by a simple smearing function which modifies a particle's track by a random amount in momentum and angles according to a Gaussian distribution of the appropriate width.

2.1.4 Expected results

Kaon production being suppressed by an order of magnitude with respect to pion production, observables related to kaon production in DIS will benefit the most from the additional 50 days on a longitudinally polarized deuteron target requested in this proposal. Simultaneous measurements of the Kotzinian-Mulders asymmetry for pions and kaons on proton and deuteron targets will provide an independent measurement of ratios of their Collins

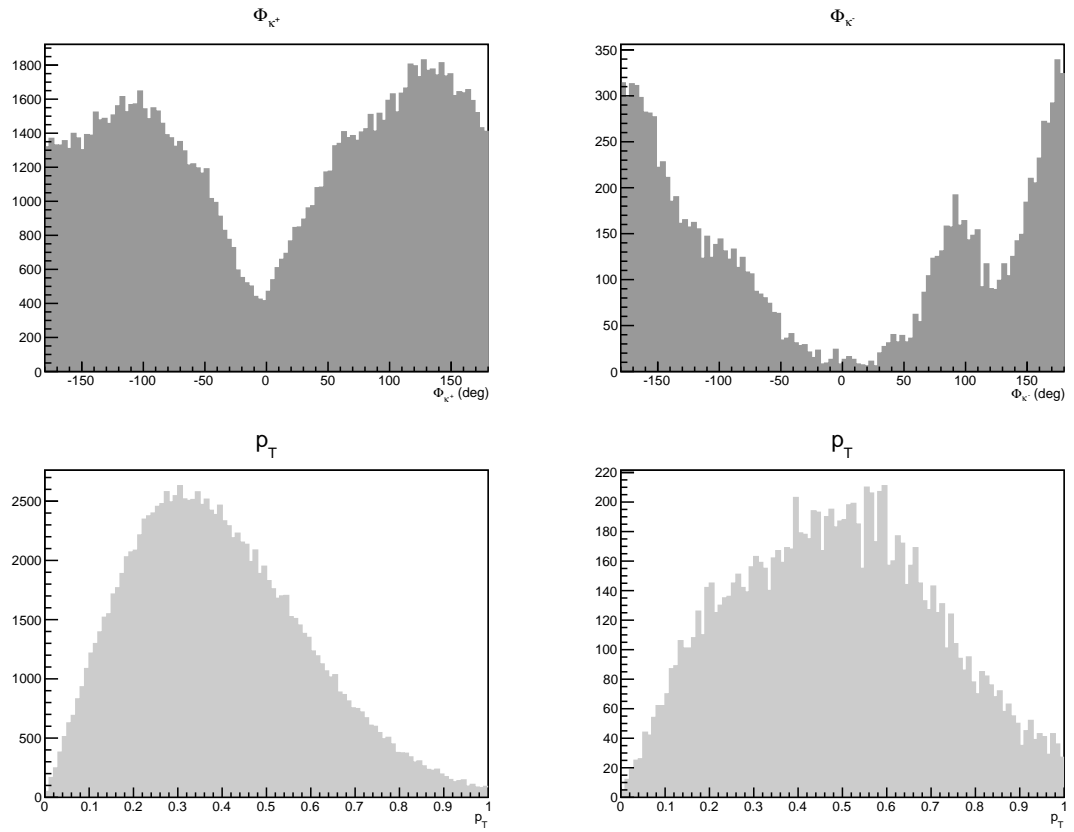


Figure 2.5: Definition of the angle ϕ , formed by the leptonic and the hadronic planes.

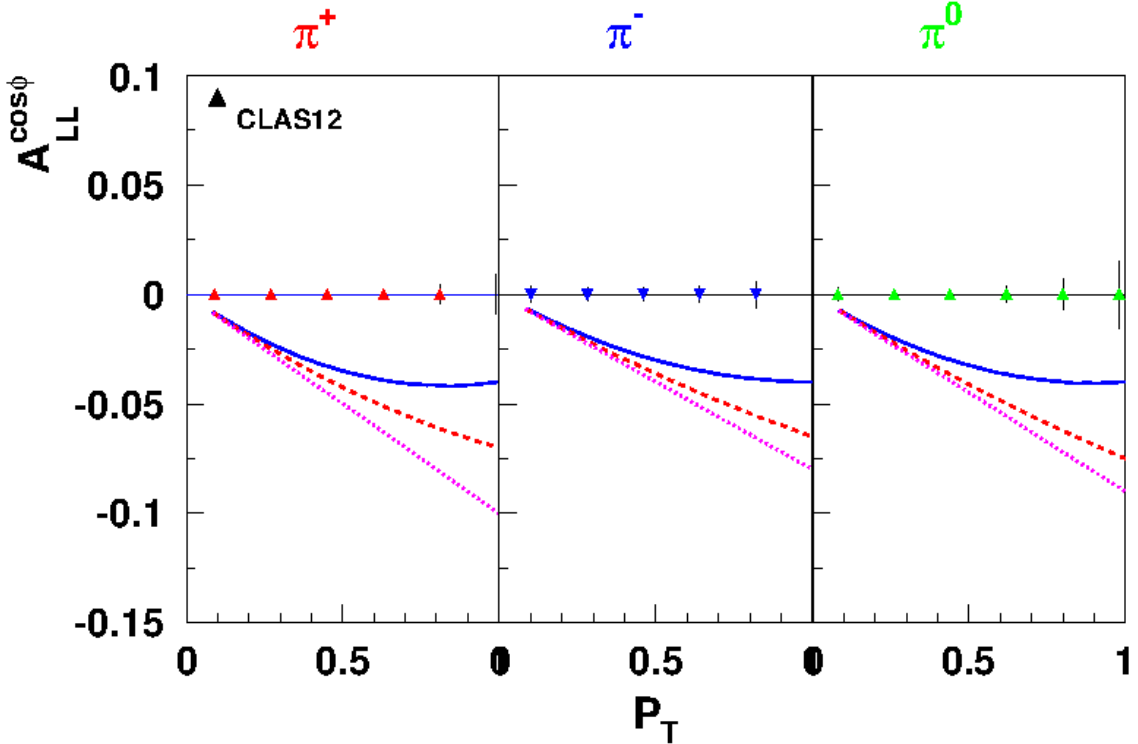


Figure 2.6: $\cos \phi$ moment of the longitudinal double spin asymmetry for SIDIS kaon electroproduction, as a function of p_T . Left plot: positive pions; central plot: negative pions right plot: neutral pions.

functions, providing complementary measurements to the e^+e^- ones. The extracted dependencies on (x_B, Q^2, P_T, z) on both pions and kaons will provide access to widths in the transverse momentum of different underlying partonic distributions, like g_1 and h_{1L} , and to their flavor dependence. Proposed measurements can be used to test the evolution properties of the Collins function. They will also provide a check of chiral limit prediction, where the ratio of pion and kaon fragmentation functions is expected to be at unity. Figures 2.6 and 2.7 show the distributions of the double-spin asymmetry constant term on deuteron as a function of the hadron p_T , for pions and kaons respectively, for a total beam time of 100 days (the 50 already approved for Run Group C plus the 50 more requested in this Run-Group-extension proposal). **add description of models** While pion projections show already a reasonable discriminating power among the available models, kaon ones turned out to be barely sufficient to test the phenomenological accuracy of the models, especially in the high- p_T region where the hadron acceptance drops (see Fig. 2.5). This affects in particular k^- , the rate of which is suppressed with respect to k^+ . The high- p_T region is also the one less constrained from other measurements, and it would benefit the most from an increased statistics for the CLAS12 measurement. The $\sin 2\phi$ moment of the longitudinal target-spin asymmetry is shown in Fig. 2.8 as a function of x_B , for both positive

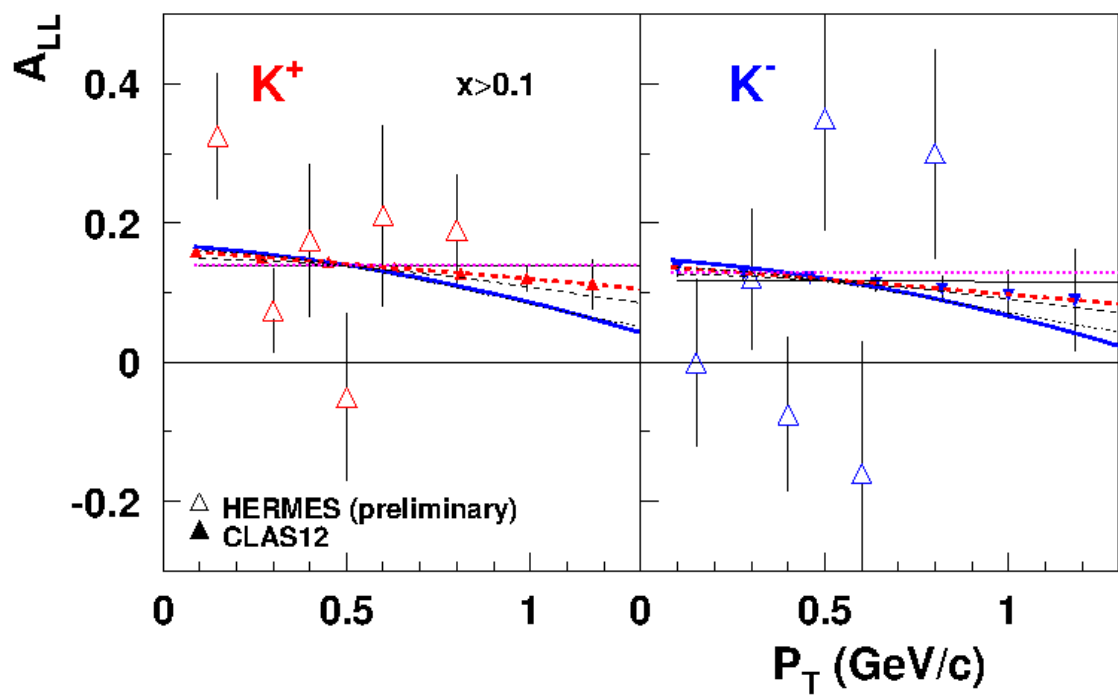


Figure 2.7: $\cos \phi$ moment of the longitudinal double-spin asymmetry for SIDIS kaon electroproduction, as a function of p_T . Left plot: positive kaons; right plot: negative kaons.

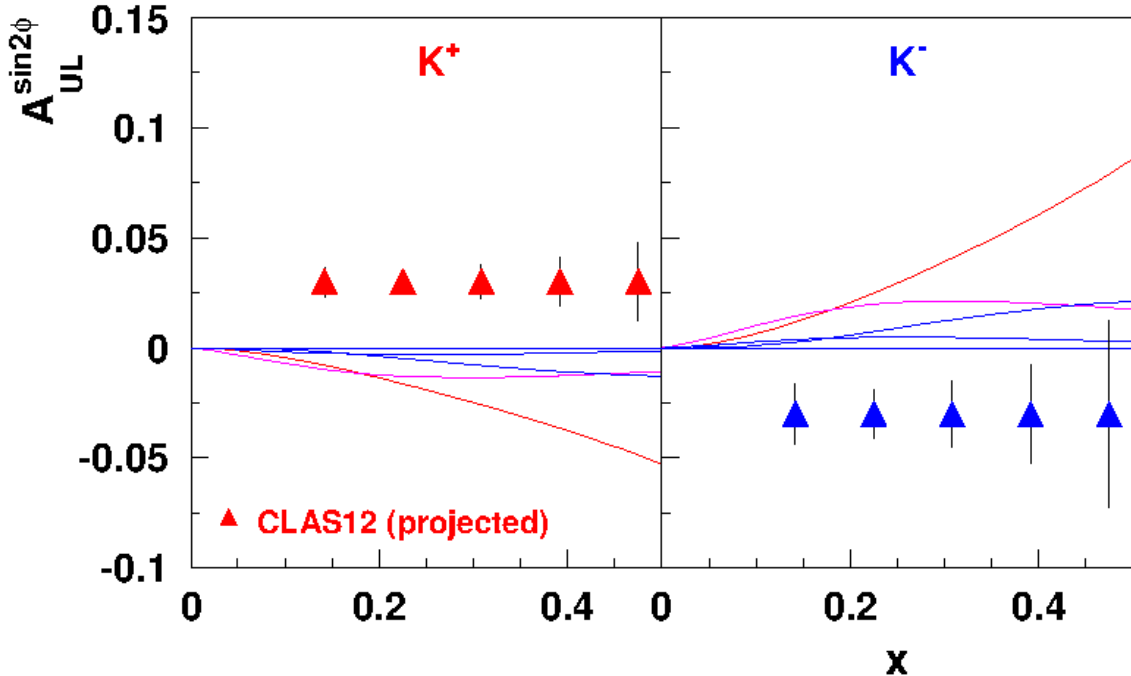


Figure 2.8: $\sin \phi$ moment of the longitudinal target-spin asymmetry for SIDIS kaon electroproduction, as a function of p_T . Left plot: positive kaons; right plot: negative kaons.

(left) and negative (right) kaons. Projections in the high- x_B region show the importance of an increased statistics, since it is where the present models are less constrained and differ the most in their prediction. The valence region is the main domain of CLAS12 physics, and it is mandatory to assure a reasonable statistical coverage for the relevant channels - as the semi-inclusive production of kaons - in this regime, not being accessible by the other experiments.

2.1.5 Semi-inclusive production of hadron pairs

In addition to the semi-inclusive production of single hadrons, other semi-inclusive channels would benefit from an increased statistics on a longitudinally polarized deuteron target. In the last years, for example, an increasing role is being played by the SIDIS production of hadron pairs, which gives the cleanest access to the chiral-odd one-dimensional picture of the nucleon. Differently from the quark (unpolarized) and helicity 1D distribution functions, the transversity distribution, as well as the two higher-twist PDF $e(x)$ and $h_L(x)$, cannot be accessed through inclusive DIS. This is due to their *chiral-odd* nature, that prevents the access through inclusive observables. In order to be accessed, indeed, they have to appear in the observables coupled to a second *chiral-odd* function, the so-called Di-Hadron fragmentation functions. The latter are the analogous of the single hadron FF described earlier in the text, and encode the fragmentation of the struck quark to the final

hadron pair. The main advantage of the di-hadron production is the fact that, while in the single-hadron case the distribution functions and the fragmentation functions appear coupled in the structure functions through a convolution integral, in the di-hadron case they are coupled through a simple product, making the final extraction easier and less sensitive to model assumptions. Among the chiral-odd PDFs, the higher-twist $h_L(x)$ is by far the least known. It can only be accessed through the di-hadron longitudinal target-spin asymmetry, where it appears coupled to the interference fragmentation functions H_1^\triangleleft , that represents the analogous of the Collins function of the single-hadron case. Together with $e(x)$, it opens the avenue to a deeper understanding of the quark-gluon-quark correlations inside the nucleon. No measurements of such an observable are presently available on a deuteron target. Preliminary analysis on a NH_3 target by CLAS shows a first non zero A_{UL} on the proton. This preliminary observation would be greatly improved by a high-precision extraction in the extended kinematics accessible by CLAS12, both on a proton and on a deuteron target. A combined measurement of the di-hadron A_{UL} on both proton and deuteron will be highly beneficial, since it will allow to perform the flavor separation of the PDFs and of the di-hadron FF. As for the single-hadron case, in order to properly disentangle the dependences of the PDF and the FF, a multidimensional mapping will be essential. Due to the reduced phase-space for the di-hadron case with respect to single hadron, an increased statistics will be essential to reach a proper accuracy in all the bins.

Bibliography

- [1] X.D. Ji and F. Yuan, Phys. Lett. B543, 66 (2002).
- [2] X.D. Ji, J.P. Ma, and F. Yuan, Nucl. Phys. B652, 383 (2003).
- [3] A.V. Belitsky, X. Ji, and F. Yuan, Nucl. Phys. B656, 165 (2003).
- [4] D.W. Sivers, Phys. Rev. D. 43, 261 (1991).
- [5] M. Anselmino and F. Murgia, Phys. Lett. B442, 470 (1998).
- [6] S.J. Brodsky, D.S. Hwang, and I. Schmidt, Nucl. Phys. B 642, 344 (2002).
- [7] J.C. Collins, Phys. Lett. B536, 43 (2002).
- [8] L. Mankiewicz, A. Schafer, and M. Veltri, Comput. Phys. Commun. 71, 305 (1992).
- [9] H. Avakian and P. Bosted, "MC-generator for DIS studies with CLAS12" (2006)

Chapter 3

Deeply Virtual Compton Scattering on the neutron with a longitudinally polarized deuteron target

S. Niccolai^{1,2}

Institut de Physique Nucléaire d'Orsay, 91406 Orsay, France

A. Biselli¹

Fairfield University, Fairfield Connecticut 06824

C. Keith¹

Thomas Jefferson National Laboratory, Newport News, VA 23606

S. Pisano¹

INFN, Laboratori Nazionali di Frascati, 00044 Frascati, Italy

D. Sokhan¹

University of Glasgow

¹co-spokesperson

²contact person, email: silvia@jlab.org

Abstract

Measurements of Deeply Virtual Compton Scattering on the neutron (nDVCS) are necessary for a complete description of nucleon structure in terms of Generalized Parton Distributions (GPDs). Combining DVCS results from both proton and neutron targets will permit the flavor decomposition of the GPDs. An experimental program of nDVCS has commenced at JLab with the already-approved experiment E12-11-003 to measure beam-spin asymmetries over a wide kinematic range using the CLAS12 detector. Here we propose to extend this program by measuring, for the first time, both target-spin and double-spin asymmetries for nDVCS using a longitudinally polarized deuteron target inside CLAS12. The measurements will be made detecting the electron and the photon in the forward part of CLAS12, and the recoil neutron in the recently completed Central Neutron Detector, thus assuring the exclusivity of the nDVCS reaction ($ed \rightarrow e'n\gamma(p)$). By fitting these results together with the beam-spin asymmetries measured by E12-11-003 at the same kinematic points, an extraction of several neutron Compton Form Factors (CFFs) can be made. $\Im m(\mathcal{E}_n)$ and $\Im m(\mathcal{H}_n)$ will be especially well determined thanks to their dominance in the beam- and target-spin asymmetries, respectively. Quark-flavor separation of the GPDs then becomes possible through a combination of the extracted neutron CFFs with those obtained from proton DVCS. In order to provide an accurate mapping of the nDVCS single and double target-spin asymmetries over the available 4-dimensional ($Q^2, x_B, -t, \phi$) phase space, and thus achieve an accurate extraction of the neutron CFFs accessible from these observables, we request 50 more days of running on a ND_3 polarized target to add to the 50 existing ones of Run Group C of CLAS12, plus a total of 25 days of calibration and ancillary runs, with the maximum available beam energy of 11 GeV. This proposal was conditionally approved (C2) by PAC43, with the request to represent it at PAC44 split it into a run-group proposal for the existing 50 days of Run-group Cb and an extension-request proposal for the other 50 days.

3.1 Introduction: Generalized Parton Distributions and DVCS

Generalized Parton Distributions (GPDs) are nowadays the object of an intense effort of research, in the perspective of understanding nucleon structure. The GPDs describe the correlations between the longitudinal momentum and transverse spatial position of the partons inside the nucleon, they give access to the contribution of the orbital momentum of the quarks to the nucleon, and they are sensitive to the correlated $q - \bar{q}$ components. The original articles and general reviews on GPDs and details of the formalism can be found in Refs. [1]-[7].

The nucleon GPDs are accessed in the measurement of the exclusive lepto-production of a photon (DVCS, which stands for deeply virtual Compton scattering) or of a meson on the nucleon, at sufficiently large Q^2 , where Q^2 is the virtuality of the photon emitted by the initial lepton, for the reaction to happen at the quark level. Figure 3.1 illustrates the leading process for DVCS, also called the “handbag diagram”. At leading-order QCD and at leading twist, considering only quark-helicity conserving quantities and the quark sector, the process is described by four GPDs, $H^q, \tilde{H}^q, E^q, \tilde{E}^q$, one for each quark flavor q , that account for the possible combinations of relative orientations of nucleon spin and quark helicity between the initial and final state. H and E do not depend on the quark helicity and are therefore called unpolarized GPDs while \tilde{H} and \tilde{E} depend on the quark helicity and are called polarized GPDs. H and \tilde{H} conserve the spin of the nucleon, whereas E and \tilde{E} correspond to a nucleon-spin flip.

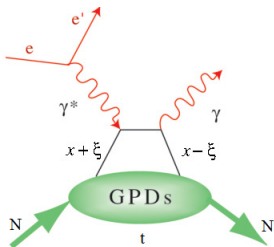


Figure 3.1: The handbag diagram for the DVCS process on the nucleon $eN \rightarrow e'N'\gamma'$. Here $x + \xi$ and $x - \xi$ are the longitudinal momentum fractions of the struck quark before and after scattering, respectively, and $t = (N - N')^2$ is the squared four-momentum transfer between the initial and final nucleons (or equivalently between the two photons). In the Bjorken limit, i.e. for $Q^2 = -q^2 = -(k - k')^2 \rightarrow \infty$ and $\nu = E_e - E_{e'} \rightarrow \infty$ so that $x_B = \frac{Q^2}{2M\nu}$ is finite, ξ is proportional to the Bjorken scaling variable x_B ($\xi \simeq \frac{x_B}{2-x_B}$, where $x_B = \frac{Q^2}{2M\nu}$, M is the nucleon mass and ν is the difference between the energies of the initial and final electron in the lab frame).

The GPDs depend upon three variables, x, ξ and t : $x + \xi$ and $x - \xi$ are the longitudinal momentum fractions of the struck quark before and after scattering, respectively, and t is

the squared four-momentum transfer between the initial and final nucleon (see caption of Fig. 3.1 for the definitions of these variables). The transverse component of t is the Fourier-conjugate variable of the transverse position of the struck parton in the nucleon. Among the three variables, x , ξ and t , which appear in the DVCS formalism, only ξ and t are experimentally accessible in these reactions.

The DVCS amplitude is proportional to combinations of integrals over x of the form:

$$\int_{-1}^1 dx F(\mp x, \xi, t) \left[\frac{1}{x - \xi + i\epsilon} \pm \frac{1}{x + \xi - i\epsilon} \right] \quad (3.1)$$

where F represents one of the four GPDs. The top combination of the plus and minus signs applies to the quark-helicity independent, or unpolarized, GPDs (H, E), and the bottom combination of signs applies to the quark-helicity dependent, or polarized, GPDs (\tilde{H}, \tilde{E}). Each of these 4 integrals, which are called Compton Form Factors (CFFs), can be decomposed into their real and imaginary parts, as

$$\Re e \mathcal{F}(\xi, t) = \mathcal{P} \int_{-1}^1 dx \left[\frac{1}{x - \xi} \mp \frac{1}{x + \xi} \right] F(x, \xi, t) \quad (3.2)$$

$$\Im m \mathcal{F}(\xi, t) = -\pi [F(\xi, \xi, t) \mp F(-\xi, \xi, t)], \quad (3.3)$$

where \mathcal{P} is Cauchy's principal value integral and the sign convention is the same as in Eq. 3.1. The information that can be extracted from the experimental data at a given (ξ, t) point depends on the observable involved. $\Re e \mathcal{F}$ is accessed primarily measuring observables which are sensitive to the real part of the DVCS amplitude, such as double-spin asymmetries, beam-charge asymmetries or unpolarized cross sections. $\Im m \mathcal{F}$ can be obtained measuring observables which are mainly sensitive to the imaginary part of the DVCS amplitude, such as single-spin asymmetries or cross-section differences.

However, knowing the CFFs does not define the GPDs uniquely. A model input is necessary to deconvolute their x dependence.

The DVCS process is accompanied by the Bethe-Heitler (BH) process, in which the final-state real photon is radiated by the incoming or scattered electron and not by the nucleon itself. The BH process, which is not sensitive to the GPDs, is experimentally indistinguishable from DVCS and interferes with it at the amplitude level. However, considering that the nucleon form factors are well known at small t , the BH process is precisely calculable.

3.2 Physics motivation: neutron GPDs and flavor separation

Measuring neutron GPDs is complementary to measuring proton GPDs: quark-flavor separation of the GPDs becomes possible only if both the proton and neutron GPDs are measured. Since we can express

$$\mathcal{H}^p(\xi, t) = \frac{4}{9} \mathcal{H}^u(\xi, t) + \frac{1}{9} \mathcal{H}^d(\xi, t) \quad (3.4)$$

and

$$\mathcal{H}^n(\xi, t) = \frac{1}{9}\mathcal{H}^u(\xi, t) + \frac{4}{9}\mathcal{H}^d(\xi, t) \quad (3.5)$$

(and similarly for \mathcal{E} , $\tilde{\mathcal{H}}$ and $\tilde{\mathcal{E}}$), it immediately follows that

$$\mathcal{H}^u(\xi, t) = \frac{9}{15}(4\mathcal{H}^p(\xi, t) - \mathcal{H}^n(\xi, t)) \quad (3.6)$$

and

$$\mathcal{H}^d(\xi, t) = \frac{9}{15}(4\mathcal{H}^n(\xi, t) - \mathcal{H}^p(\xi, t)). \quad (3.7)$$

An extensive experimental program devoted to the measurement of GPDs using the DVCS channel on a proton target has been approved at Jefferson Lab, in particular with CLAS12. Single-spin asymmetries with polarized beam and/or linearly or transversely polarized proton targets, as well as unpolarized and polarized cross sections, will be measured with high precision and a vast kinematic coverage. If a similar program is performed on the neutron, the flavor separation of the various GPDs will be possible. An experiment to measure the beam-spin asymmetry for nDVCS, particularly sensitive to the GPD E_n , has already been approved [8]. The present proposal focuses on the extraction of two more observables, the target single-spin asymmetry and the (beam-target) double-spin asymmetry for nDVCS on a longitudinally polarized deuterium target. The next sections will outline those GPDs to which the nDVCS observables we plan to measure show the most sensitivity.

3.3 DVCS spin observables

A complete analysis of DVCS observables, including the asymmetries of interest in this document, in terms of Fourier harmonics with respect to the azimuthal angle, was carried out by Belitsky *et al.* [9], up to twist-3 approximation. These asymmetries allow the extraction of separate components of the azimuthal angular dependence of the $eN \rightarrow eN'\gamma$ cross section, which are related to the Compton Form Factors (CFFs) defined in Eqs. 3.2–3.3.

The amplitude \mathcal{T} for the exclusive electroproduction of photons is the sum of the DVCS $\mathcal{T}_{\text{DVCS}}$ and Bethe-Heitler (BH) \mathcal{T}_{BH} amplitudes:

$$\mathcal{T}^2 = |\mathcal{T}_{\text{BH}}|^2 + |\mathcal{T}_{\text{DVCS}}|^2 + \mathcal{I}, \quad (3.8)$$

where \mathcal{I} is the interference term

$$\mathcal{I} = \mathcal{T}_{\text{DVCS}}\mathcal{T}_{\text{BH}}^* + \mathcal{T}_{\text{DVCS}}^*\mathcal{T}_{\text{BH}}. \quad (3.9)$$

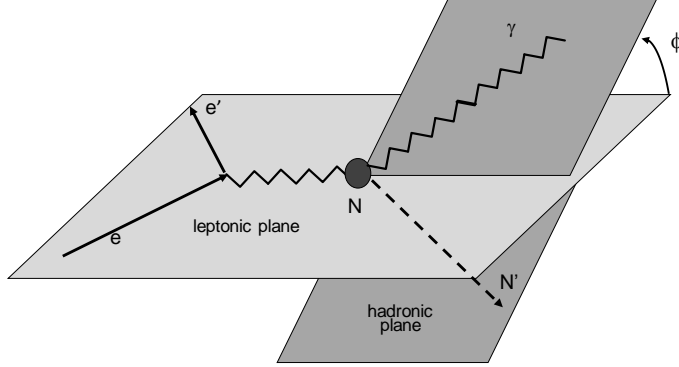


Figure 3.2: Schematic to illustrate the definition of the angle ϕ , formed by the leptonic and hadronic planes, in the $eN \rightarrow eN'\gamma$ reaction.

The azimuthal angular dependence of each of the three terms is given by [9]:

$$|\mathcal{T}_{\text{BH}}|^2 = \frac{e^6}{x_B^2 y^2 (1 + \epsilon^2)^2 t \mathcal{P}_1(\phi) \mathcal{P}_2(\phi)} \{ c_0^{\text{BH}} + \\ + \sum_{n=1}^2 c_n^{\text{BH}} \cos(n\phi) + s_1^{\text{BH}} \sin(\phi) \}, \quad (3.10)$$

$$|\mathcal{T}_{\text{DVCS}}|^2 = \frac{e^6}{y^2 Q^2} \{ c_0^{\text{DVCS}} + \sum_{n=1}^2 [c_n^{\text{DVCS}} \cos(n\phi) + \\ + s_n^{\text{DVCS}} \sin(n\phi)] \}, \quad (3.11)$$

$$\mathcal{I} = \frac{e^6}{x_B y^3 t \mathcal{P}_1(\phi) \mathcal{P}_2(\phi)} \{ c_0^{\mathcal{I}} + \sum_{n=1}^3 [c_n^{\mathcal{I}} \cos(n\phi) + \\ + s_n^{\mathcal{I}} \sin(n\phi)] \}, \quad (3.12)$$

where ϕ is the angle between the leptonic and hadronic planes, as shown in Fig. 3.2, \mathcal{P}_1 and \mathcal{P}_2 are lepton BH propagators, $y = P_1 \cdot q_1 / P_1 \cdot k$, where P_1 is the four-momentum of the initial nucleon). For more details and definitions, see [9]. The Fourier coefficients in $|\mathcal{T}_{\text{BH}}|^2$ are calculable in QED, with knowledge of the nucleon form factors, while the ones appearing in \mathcal{I} and $|\mathcal{T}_{\text{DVCS}}|^2$ depend on the Compton Form Factors.

3.3.1 Target-spin asymmetry

The use of a longitudinally polarized (LP) target allows the extraction of the target-spin asymmetry A_{UL} (here also referred to as TSA) which is given, at twist-2 level, by:

$$A_{UL}(\phi) \sim \frac{s_{1,LP}^{\mathcal{I}} \sin \phi}{c_{0,unp}^{BH} + (c_{1,unp}^{BH} + c_{1,unp}^{\mathcal{I}} + \dots) \cos \phi + \dots} \quad (3.13)$$

where the ellipses in the denominator represent smaller terms. The $\sin \phi$ coefficient $s_{1,LP}$, originating from the DVCS/BH interference term, at leading-twist is proportional to a linear combination of the imaginary parts of the four CFFs,

$$\begin{aligned} s_{1,LP} &\propto \Im[F_1 \tilde{\mathcal{H}} + \xi(F_1 + F_2)(\mathcal{H} + \frac{x_B}{2}\mathcal{E}) + \\ &\quad - \xi(\frac{x_B}{2}F_1 + \frac{t}{4M^2}F_2)\tilde{\mathcal{E}}], \end{aligned} \quad (3.14)$$

where F_1 and F_2 are, respectively, the Dirac and Pauli form factors. In the case of a proton target, the dominant contribution to A_{UL} comes from $\Im\mathcal{H}_p$ and from $\Im\mathcal{H}_p$. **In the neutron case, for which $F_2 \gg F_1$, this observable is mostly sensitive to $\Im\mathcal{H}_n$.**

3.3.2 Double-spin asymmetry

The use of a polarized electron beam along with a polarized target allows also the determination of the double spin asymmetry A_{LL} . Unlike A_{UL} , the Bethe-Heitler process alone can generate a non-zero value for this observable. At twist-2 level, it takes the form:

$$A_{LL}(\phi) \sim \frac{c_{0,LP}^{BH} + c_{0,LP}^{\mathcal{I}} + (c_{1,LP}^{BH} + c_{1,LP}^{\mathcal{I}}) \cos \phi}{c_{0,unp}^{BH} + (c_{1,unp}^{BH} + c_{1,unp}^{\mathcal{I}} + \dots) \cos \phi \dots} \quad (3.15)$$

with

$$\begin{aligned} c_{0,LP}^{\mathcal{I}}, c_{1,LP}^{\mathcal{I}} &\propto \Re[F_1 \tilde{\mathcal{H}} + \xi(F_1 + F_2)(\mathcal{H} + \frac{x_B}{2}\mathcal{E}) + \\ &\quad - \xi(\frac{x_B}{2}F_1 + \frac{t}{4M^2}F_2)\tilde{\mathcal{E}}], \end{aligned} \quad (3.16)$$

In this expression, the interference terms are expected to be smaller than the known BH terms. Moreover, both the constant and the $\cos \phi$ -dependent terms contain contributions from both BH and the DVCS/BH interference. Nonetheless, it is expected that in some parts of the phase space A_{LL} has a measurable sensitivity to $\Re\tilde{\mathcal{H}}_p$ (and, in a lesser way, $\Re\mathcal{H}_p$), for the proton, **and to $\Re\mathcal{H}_n$ for the neutron.**

3.4 Extraction of CFFs from fits to DVCS observables

In recent years, various groups have developed and applied different procedures to extract Compton Form Factors from DVCS observables. The approach adopted in this proposal

[10, 11] has proved to be very effective and practical to extract GPD information from the existing proton DVCS data³. It is based on a local-fitting method at each given experimental $(Q^2, x_B, -t)$ kinematic point. In this framework, instead of four complex CFFs defined as in Eqs. 3.2 and 3.3, there are eight real CFFs defined as

$$F_{Re}(\xi, t) = \Re e \mathcal{F}(\xi, t) \quad (3.17)$$

$$F_{Im}(\xi, t) = -\frac{1}{\pi} \Im m \mathcal{F}(\xi, t) = [F(\xi, \xi, t) \mp F(-\xi, \xi, t)], \quad (3.18)$$

where the sign convention is the same as for Eq. 3.1. These CFFs are the almost-free⁴ parameters, which are extracted from DVCS observables using the well-established DVCS+BH theoretical amplitude. The BH amplitude is calculated exactly while the DVCS one is taken at the QCD leading twist. The expression of these amplitudes can be found, for instance, in [12].

As there are eight CFF-related unknowns (four “real” CFFs, four “imaginary” ones) left as free parameters, including more observables, measured at the same kinematic points, will result in more tightly constrained fits and will increase the number and accuracy of CFFs extracted from them.

This was shown, for instance, with the analysis of the CLAS eg1-DVCS dataset [14], which was taken at 6 GeV with a longitudinally-polarized proton target. The simultaneous fit of three proton-DVCS asymmetries (BSA, TSA and DSA) lead to the extraction of $\Im m \mathcal{H}$ and $\Im m \tilde{\mathcal{H}}$, as is shown in Fig. 3.3. These results for H_{Im} and \tilde{H}_{Im} confirmed what had been previously observed in a qualitative way by direct comparison of the t -dependence of the eg1-dvcs TSAs and the e1-dvcs BSAs in [15]: the t -slope of $\Im m \mathcal{H}$ is much steeper than that of $\Im m \tilde{\mathcal{H}}$, hinting at the fact that the axial charge (linked to $\Im m \mathcal{H}$) might be more “concentrated” in the center of the nucleon than the electric charge (linked to $\Im m \tilde{\mathcal{H}}$). This is an interesting example of the nucleon tomography that becomes possible with the determination of CFFs, without the need for model input.

The main goal of the experiment proposed here is to provide, in a wide phase space, two kinds of asymmetries (single-target, and double beam-target), to be simultaneously fitted together with the beam-spin asymmetry that will be measured, at the same kinematic points, in the approved unpolarized-target experiment [8], and thus allow the extraction of the neutron CFFs. The results we expect to obtain are presented in Section 3.14.

3.5 Experimental situation

The determination of all the GPDs is clearly a non-trivial task, and requires measurement of several observables on both proton and neutron targets. Such a dedicated experimental

³Eventually, our results will also be compared to the various existing model parametrizations for the GPDs, the free parameters of which will be constrained by our data.

⁴The values of the CFFs are allowed to vary within ± 5 times the values predicted by the VGG model [12, 13].

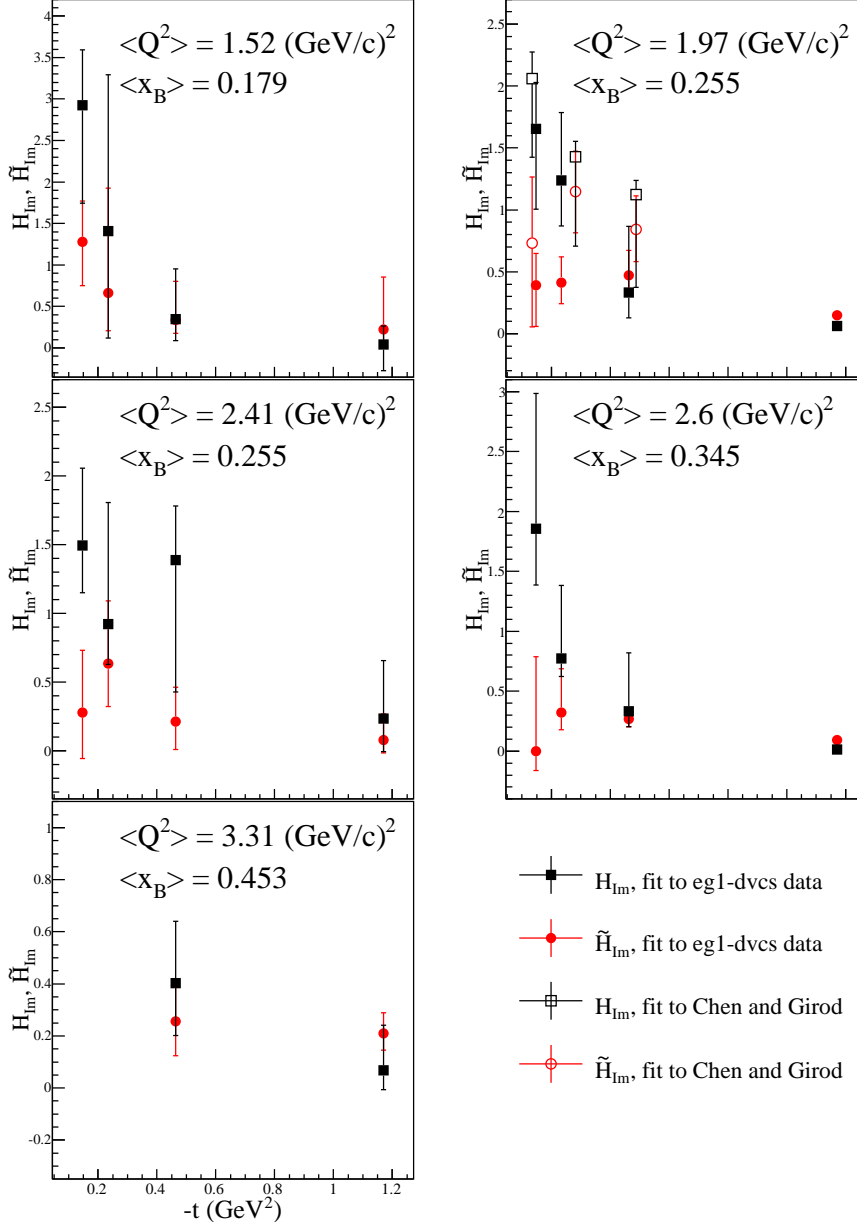


Figure 3.3: t dependence for each Q^2 - x_B bin of H_{Im} (black squares) and \tilde{H}_{Im} (red circles). The full points are obtained by fitting the eg1-DVCS data (TSA, BSA and DSA) [14]. The empty points were obtained by fitting the BSA results from [16] integrated over all values of Q^2 at $x_B \sim 0.25$, and the TSAs from [17].

Observable (target)	Sensitivity to CFFs	Completed experiments	12-GeV experiments
$\Delta\sigma_{beam}(p)$	$\Im m \mathcal{H}_p$	Hall A [19],[26] ⁵ , CLAS [22]	Hall A [23], CLAS12 [24] Hall C [27]
BSA(p)	$\Im m \mathcal{H}_p$	HERMES [21], CLAS [20, 16, 14]	CLAS12 [24]
TSA(p)	$\Im m \tilde{\mathcal{H}}_p, \Im m \mathcal{H}_p,$	HERMES [21], CLAS [17, 15, 14]	CLAS12 [24]
DSA(p)	$\Re e \mathcal{H}_p, \Re e \tilde{\mathcal{H}}_p$	HERMES [21], CLAS [14]	CLAS12 [24]
tTSA(p)	$\Im m \mathcal{H}_p, \Im m \mathcal{E}_p$	HERMES [21]	CLAS12 [25]
$\Delta\sigma_{beam}(n)$	$\Im m \mathcal{E}_n$	Hall A [18],[28] ⁵	
BSA(n)	$\Im m \mathcal{E}_n$		CLAS12 [8]

Table 3.1: Summary of all existing data on proton and neutron DVCS spin observables, along with their sensitivity to the various GPDs. The “t” prefix indicates transversely polarized target.

program, concentrating on a proton target, has started worldwide in the past few years. Table 3.1 summarizes the current situation. It is evident that while data exist for all proton observables, neutron DVCS data is woefully lacking. The only existing nDVCS experiment was performed in Hall A [18], where the beam-polarized cross section difference was extracted, albeit with small kinematical coverage, low statistical precision, and high systematic uncertainties. There also exists a number of approved 12 GeV pDVCS experiments at JLab, both in Hall A and Hall B, but only one approved neutron experiment, to measure the beam-spin asymmetries using CLAS12 [8]. While the new pDVCS experiments will greatly increase both the coverage and statistics of the existing proton data, we propose to further advance the nDVCS program by performing the first ever measurements of target-spin and double-spin asymmetries on a longitudinally polarized neutron target.

The currently approved CLAS12 program includes about 120 days of beam time allocated for data taking on unpolarized proton target, 120 days on longitudinally polarized proton target (NH_3), 90 days on unpolarized deuterium target, and 50 days (plus 15 of overhead) on longitudinally polarized deuterium target (ND_3). Considering that the polarization of the deuteron (and of the neutron) in ND_3 is about half that of the proton in NH_3 , that the cross section for neutron-DVCS is more than a factor of two smaller than the one for proton-DVCS, and that the detection efficiency for neutrons is at least a third of that for protons, as of today there is a big difference in statistical power between the polarized proton and neutron datasets for CLAS12. Doubling the current statistics on (ND_3), as this proposal aims to do, would contribute to reduce this gap.

⁵Analysis underway.

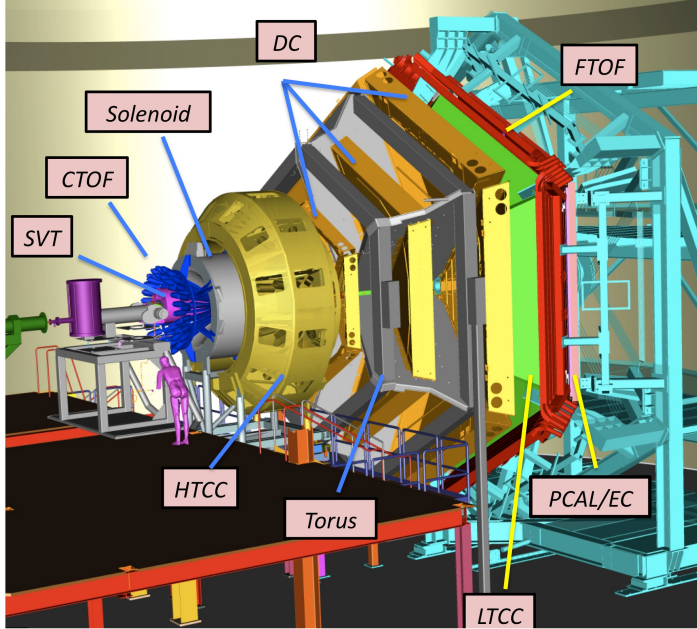


Figure 3.4: The CLAS12 detector and its components. In the forward part, the six coils of the superconducting toroidal magnet segment the detector into six sectors, each equipped with three regions of drift chambers (DC), High- and Low-Threshold Cherenkov Counters (HTCC and LTCC), Pre-Shower and Electromagnetic Calorimeters (PCAL and EC) and Forward Time-of-Flight (FTOF) scintillators. The central detector surrounds the target and is contained inside a solenoid magnet; its base equipment is composed of the Silicon Vertex Tracker (SVT) and the Central Time-of-Flight (CTOF).

3.6 Proposed experimental setup

A dynamically polarized $^{14}\text{ND}_3$ target, described in the next Section, will provide the polarized neutrons on which the 11-GeV polarized electron beam from the upgraded CEBAF will be rastered. In order to map the complex kinematic dependence of the GPDs, a wide acceptance detector is necessary. For this experiment, we plan to use the CLAS12 detector (Fig. 3.4), which will be devoted to the detection of the electron, the neutron (in the Central Neutron Detector, described in Section 3.6.2) and the DVCS-BH photons. The CLAS12 acceptance for photons reaches down to polar angles of about 5° with the EC. The possibility of extending the acceptance for photons down to 2.5° using the electromagnetic calorimeter of the Forward Tagger [29] is an option, but, due to the as-yet unclarified compatibility issues that are discussed in Section 3.12, it is not included in the baseline setup of the proposed experiment.

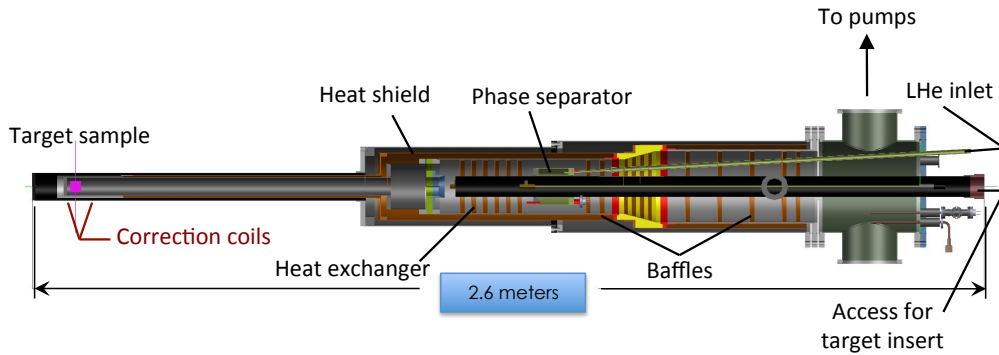


Figure 3.5: Side view of the CLAS12 dynamically polarized target.

3.6.1 Polarized target

The proposed experiment will utilize a new, dynamically polarized target under construction for the CLAS12 spectrometer by a collaboration of the Jefferson Lab Target Group, the University of Virginia, Old Dominion University and Christopher Newport University. The target cryostat, shown schematically in Figure 3.5, is specifically designed according to the geometrical constraints imposed by the CLAS12 detector package, primarily the Silicon Vertex Tracker. Frozen, deuterated ammonia has been chosen as the target material for its high deuteron content (30% by weight), high deuteron polarization (up to 50%), and high resistance to radiation damage [30]. Construction of the target is currently underway, with initial tests anticipated in 2017.

To realize Dynamic Nuclear Polarization (DNP), a dielectric solid is doped with a small concentration (10^{19} cm^{-3}) of paramagnetic radicals. The unpaired electrons in the radicals are highly polarized by cooling the sample to a low temperature and applying a strong magnetic field. For example, at the proposed operating conditions of 1 K and 5 T, the electron polarization is greater than 99.99%. Off-center microwave saturation of the electron spin resonance drives mutual electron/nuclear spin flips which effectively transfer the electron polarization to the nuclei. Either positive or negative nuclear polarization can be realized, depending on whether the microwave frequency is slightly below or above the electron resonance frequency of 140 GHz.

The target sample will be cooled to 1 K by a bespoke ^4He evaporation refrigerator with an anticipated cooling power of about 0.5 W at 1.0 K. The CLAS12 solenoid shall provide the necessary 5 T magnetic field. For optimum polarization, the uniformity of the field should be about 100 ppm or better over the volume of the sample. If the solenoid is unable to provide this level of uniformity, it may be necessary to include small superconducting correction coils inside the target cryostat, or to reduce the sample dimensions.

Luminosity

The nominal length of the target container will be $L = 4.0$ cm, with a 2.5 cm diameter. It will be filled with mm-sized granules of frozen $^{14}\text{ND}_3$ with a density $\rho = 1.007 \text{ g/cm}^3$ and a packing fraction $f \approx 0.6$. The total luminosity with electron beam intensity I will be

$$\begin{aligned}\mathcal{L} &= f\rho L N_A I \\ &= 0.6(1.007 \text{ g/cm}^3)(4.0 \text{ cm})(6.02 \times 10^{23} \text{ g}^{-1})(6.24 \times 10^9 \text{ s}^{-1} \text{nA}^{-1}) \\ &= 9.1 \times 10^{33} \text{ cm}^{-2} \text{s}^{-1} \text{nA}^{-1}\end{aligned}\tag{3.19}$$

Note that this number is per nA of incident beam current. The luminosity for scattering from polarized neutrons within the deuterons will be 3/20 of the above number, or $1.4 \times 10^{33} \text{ cm}^{-2} \text{s}^{-1} \text{nA}^{-1}$. We anticipate running the experiment at 10 nA, giving a neutron luminosity of $1.4 \times 10^{34} \text{ cm}^{-2} \text{s}^{-1}$. In order to reduce effects due to localized beam heating and radiation damage, the beam will be continuously rastered over 2.4 cm of the 2.5 cm target diameter.

Polarization measurement

The deuteron polarization will be monitored online by continuous wave NMR, using the industry standard Liverpool Q-meter [31]. There are two means whereby the polarization can be extracted from the NMR signal: the area method and the peak-height method. We intend to use both, and either should provide a relative uncertainty $\Delta P/P \approx 4\%$. We also intend to extract the polarization offline using the quasi-elastic scattering asymmetry.

First, the total area of the NMR absorption signal is proportional to the vector polarization of the sample, and the constant of proportionality can be calibrated against the polarization of the sample measured under thermal equilibrium (TE) conditions. This is the standard method used for polarized proton targets, but can be more problematic for deuteron targets. Typical conditions for the TE measurements are 5 T and 1.4 K, where the deuteron polarization is only 0.075%, compared to 0.36% for protons. This smaller polarization, along with quadrupolar broadening, makes the deuteron TE signal more difficult to measure with high accuracy. We therefore intend to implement a straightforward modification to the NMR circuit that has been shown to improve the stability and signal-to-noise ratio of the NMR signal [32]. This modification was successfully utilized during the eg1-DVCS experiment in Hall B.

Second, the deuteron polarization can also be extracted from the *shape* of the NMR signal. The deuteron is a spin-1 nucleus with three magnetic substates, $m = -1, 0, +1$, and the NMR absorption signal is a superposition of the $-1 - 0$ and $+1 - 0$ transitions. In the case of $^{14}\text{ND}_3$, the deuteron's electric quadrupole moment interacts with electric field gradients within the molecule and splits the degeneracy of the two transitions. The degree of splitting depends on the angle between the magnetic field and direction of the electric field gradient. The resultant line shape, integrated over a sample of many polycrystalline beads, has the form of a Pake doublet (see Fig.3.6). It has been experimentally demonstrated that,

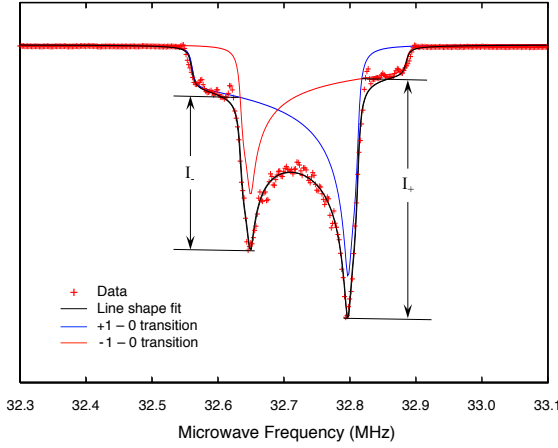


Figure 3.6: Typical NMR signal of polarized $^{14}\text{ND}_3$. The black line results from a sophisticated line shape analysis of the data points and is a superposition of the two NMR transitions shown in red and blue. This figure is adapted from [34].

at or near steady-state conditions, the magnetic substates of deuterons in dynamically polarized $^{14}\text{ND}_3$ are populated according to the Boltzmann distribution with a characteristic *spin* temperature T_s that can be either positive or negative, depending on the sign of the polarization. In this case, the vector polarization can be determined by the ratio of the two transition intensities, $r = I_+/I_-$ [33]:

$$P_z = \frac{(r^2 - 1)}{(r^2 + r + 1)}. \quad (3.20)$$

An online estimate of the polarization can be made by comparing the heights of the two peaks. For a more accurate determination, an offline analysis of the entire line shape is necessary [33].

Finally, the polarization will also be studied offline using the experimental data. We will extract the product of the beam and target polarization, $P_b P_t$, by measuring the quasi-elastic asymmetry ($\vec{d}(e, e' p)$) and by comparing it with the known theoretical value:

$$P_b P_t = \frac{1}{D_f} \frac{A_{\text{meas}}}{A_{\text{theo}}} \quad (3.21)$$

where D_f is the dilution factor to account for the contribution of the unpolarized background (Section 3.10). The target polarization value, needed for the TSA, will be then computed by taking the ratio of $P_b P_t$ and the value of the beam polarization P_t , measured in dedicated Møller polarimetry runs.

Overhead for target operation

There are four routine target operations that must be considered as overhead. First, we intend to provide an initial dose of approximately $20 \text{ Pe}^-/\text{cm}^2$ at 200 nA to each target sample prior to its use in the nDVCS experiment.⁶ This is necessary to achieve the highest possible deuteron polarization, as is explained below. Second, the target must be periodically warmed to approximately 100 K in order to repair the deleterious effects of radiation damage, a process known as annealing. Third, the target sample must be replaced when the anneals become ineffective at repairing the radiation damage. Fourth, the NMR system will be periodically calibrated by performing measurements of the thermal equilibrium polarization of deuterons at 5 T and temperatures around 1.4 K . We examine each of this in the following sections, and a summary is made at the end.

Cold dose: In solid ammonia, paramagnetic radicals are created within the target sample by ionizing radiation, usually in the form of a $10\text{--}20 \text{ MeV}$ electron beam, at a dose of about $100 \text{ Pe}^-/\text{cm}^2$. This is usually applied with the material cooled to 90 K with liquid argon, after which it may be stored indefinitely in liquid nitrogen. In the case of *deuterated* ammonia, experience has shown that polarizations greater than 20% are only achieved after an additional “cold” dose of approximately $10 \text{ Pe}^-/\text{cm}^2$ has been applied to the sample at 1 K . During the EG4 program in Hall B, the deuteron polarization increased from an initial value under 20% to more than 45% after a cold dose of $20 \text{ Pe}^-/\text{cm}^2$ [35]. In this case, the CLAS detectors were turned off and a 100 nA beam was applied to the sample for an hour or so, followed by a 100 K anneal. These cold irradiations were interspersed with normal data-taking at 2 nA , and the deuteron polarization was observed to increase after each anneal, eventually exceeding 45% . Rather than following this prescription, we intend to prepare each target sample with a $20 \text{ Pe}^-/\text{cm}^2$ cold dose before using it in the experiment. The CLAS12 detectors will be turned off for this procedure, which will require about a day for each sample at 200 nA .

Annealing: As a solid polarized target material, deuterated ammonia has a remarkably high resistance to radiation damage, exceeded only by lithium hydride and lithium deuteride. When exposed to ionizing radiation, the decay of the polarization is roughly exponential in manner,

$$P = P_o e^{-D/\delta}. \quad (3.22)$$

Here D is the dose, measured in Pe^-/cm^2 . The critical dose δ of ND_3 is different for the positive and negative spin states, with $\delta_+ = 13 \text{ Pe}^-/\text{cm}^2$ and $\delta_- = 26 \text{ Pe}^-/\text{cm}^2$ [30]. The polarization decay is due to the creation of additional paramagnetic species that do not contribute directly to the DNP process, but do contribute to the spin-lattice relaxation of the nuclear spins. Fortunately, the concentration of these new radicals can be reduced by annealing the target sample at temperatures up to about 100 K for some tens of minutes.

For the purposes of this proposal, we assume an initial polarization of 45% , which has been achieved in both the Hall C polarized target and the original Hall B polarized target.

⁶ $1 \text{ Pe}^- = 10^{15} \text{ electrons.}$

To maintain an average polarization of 40%, the radiation damage must be repaired by annealing the target sample when the polarization falls to 35%, or in other words, when the dose reaches $-\ln(\frac{0.35}{0.45})\delta \approx 5 \text{ Pe}^-/\text{cm}^2$. Here we have used the average value of δ_+ and δ_- . Assuming a 10 nA beam current distributed evenly over a 2.4 cm diameter, this dose will be accumulated, on average, after 4 days. We estimate a total of four hours will be required to anneal the target, cool it back to 1 K, and repolarize it to 40–45%.

Target lifetime: During 100 days of beam time at 10 nA, the polarized target will accumulate a total dose of $120 \text{ Pe}^-/\text{cm}^2$. However, the maximum that a ND₃ sample can tolerate before it must be replaced is not fully known. McKee [36] reports that for the Gen01 experiment in Hall C, a total of dose of $315 \text{ Pe}^-/\text{cm}^2$ was deposited on six different samples, and at least one continued to give high polarizations even after a dose of $100 \text{ Pe}^-/\text{cm}^2$. The total dose had little or no effect on the frequency of anneals, although the maximum attainable polarization did decline slightly after about $50 \text{ Pe}^-/\text{cm}^2$. For this proposal we make the conservative estimate that the samples will be replaced after a total dose of $50 \text{ Pe}^-/\text{cm}^2$, of which $20 \text{ Pe}^-/\text{cm}^2$ will occur before data-taking begins. The remainder will be incurred after about 25 days of data-taking at 10 nA, and so we anticipate that four samples of ND₃ will be sufficient for the entire experiment. Dedicated carbon runs will occur between the ND₃ sample changes. The time required to replace an old ND₃ sample with the carbon target, then replace the carbon with fresh ND₃, perform a TE calibration on the new sample and polarize it to 40–45% should be about 12 hours. Note that this does not include the actual time spent acquiring data on the carbon target.

TE measurements: Thermal equilibrium (TE) measurements are necessary to calibrate the NMR system, and must be performed whenever a new target sample is introduced into the experiment. Additional measurements are made throughout the experiment in order to monitor and reduce sources of systematic uncertainty such as gain drift and settling of the sample beads. To perform a TE, the target sample must first have its existing dynamic polarization destroyed, either by temporarily warming the sample or temporarily lowering the magnetic field to zero. The sample must then be allowed to achieve its thermal equilibrium polarization, which it approaches in an exponential manner with a spin-lattice time constant T_1 that depends on the field strength, the sample’s temperature, and its density of paramagnetic radicals. Since annealing the sample reduces its radical density and increases T_1 , it is best to do TEs prior to the anneals. Most measurements are made around 1.4 K, where the signal size is not too small, and T_1 is not too long. Because the deuteron TE signal is small, a significant amount of signal averaging must be utilized to achieve a precise determination of its area, and so the time required for each measurement will depend strongly on the signal-to-noise ratio of NMR system. Based on past experience, we assume six hours will be sufficient. This includes the time required to polarize the sample to 40–45% at the end of the calibration.

Target overhead summary: Based on the above information we provide the following estimate for the total overhead necessary to operate the polarized target. The total is 282 hours, or about 12 days. Whenever possible, anneals, TE measurements, and target changes

can be coordinated with scheduled or unscheduled beam outages to lessen their impact on data acquisition and further reduce the overhead.

1. Cold dose of $20 \text{ Pe}^-/\text{cm}^2$ at 200 nA . Required: 3 @ 24 hours each. Total: 72 hours.
2. Anneal every $5 \text{ Pe}^-/\text{cm}^2$. Required: 21 @ 4 hours each. Total: 84 hours.
3. Change target sample after $30 \text{ Pe}^-/\text{cm}^2$. Required: 3 @ 12 hours each. Total: 36 hours.
4. TE calibration of NMR system at the beginning of each target sample, and after $10 \text{ Pe}^-/\text{cm}^2$. Required: 15 @ 6 hours each. Total: 90 hours.

3.6.2 Central Neutron Detector

The Central Neutron Detector was conceived to extend the CLAS12 acceptance for the recoil neutrons of nDVCS, which are expected to be mostly emitted between 50° and 70° [8]. The requirements of the detector are:

- good capabilities for neutron identification, via the measurement of β (with $\beta = \frac{v}{c}$), for the kinematic range of interest ($0.2 < p_n < 1.2 \text{ GeV}/c$, $40^\circ < \theta_n < 80^\circ$) and
- neutron momentum resolution σ_P/P within 10%,

Early simulation studies [8] showed that these performances can be achieved by a scintillator-based detector providing a timing resolution of about 150 ps.

The core of the CND (Fig. 3.7), which will be placed in the Central Detector, in the 10 cm of radial space left between the CTOF and the solenoid magnet, is a barrel, coaxial with the beam direction, made of three radial layers of trapezoidal plastic-scintillator bars. Each radial layer contains 48 bars, connected in pairs by a "u-turn" light guide at the downstream end. Photomultipliers are coupled to the upstream end of each scintillator via 1.5m-long light guides. For each hit, half of the light emitted in a scintillator paddle is collected by the upstream PMT (the "direct" signal), while the other half propagates through the u-turn and the neighboring paddle to the PMT connected at its end (the "indirect" signal).

Three such scintillator pairs (inner, middle, and outer) are grouped together to form a single, radial "block". The CND comprises 24 of these blocks, covering the entire azimuthal range (Fig. 3.8).

The assembly of the CND, which was entirely carried out at the IPN Orsay, started in December 2013, and was completed in February 2015. The detector was shipped and stored at JLab in June 2015, awaiting its installation in CLAS12. Upon assembly, each block of the CND was tested with cosmic rays, triggering on the triple-coincidence of the signal in all three layers. Data were taken for about one week for each block, and the block performances were studied, with special attention to the timing resolution. Figure 3.9 shows the raw distribution of TDCs as a function of ADCs for the six PMTs in one of the

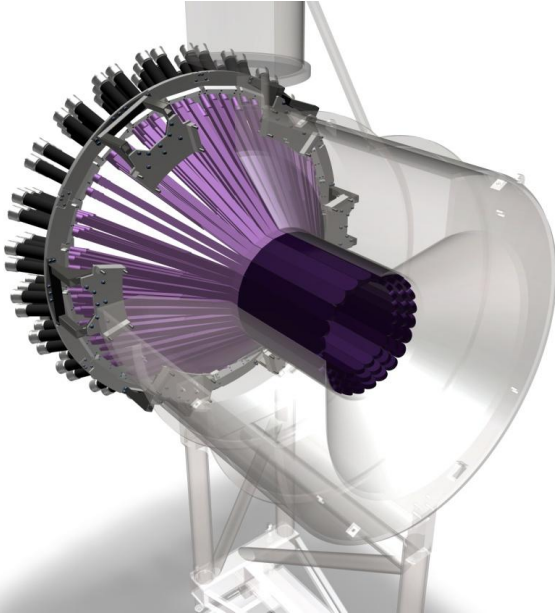


Figure 3.7: Design of the Central Neutron Detector, inserted in the CLAS12 solenoid.

24 blocks. Notice the clear separation between direct (low-TDC/high-ADC) and indirect (high-TDC/low-ADC) signals.

To define an average time resolution for our setup in the triple-coincidence trigger configuration, we use the method inspired by the work done in [37] and later adopted for the CLAS TOF system [38].

The timing resolutions for all the CND blocks, computed according to the method of [38], are represented by the black triangles in Fig. 3.10. The average is 148.0 ps. As a cross check, the resolution was also computed using the method adopted by V. Baturin for the CLAS12 CTOF [39] (red triangles in Fig. 3.10, with average 149.3 ps). The results of the two methods are consistent. The resolutions of the 24 blocks are very close to the required 150 ps. The systematic uncertainty of our results is estimated to be about 7%, determined by repeating the measurements multiple times, and by comparing multiple subsets of each measurement.

Thus, for resolutions of 150 ps, we have a systematic uncertainty of about 10 ps.

It is also worth mentioning that the TDCs that will be used for the actual experiment will have a better resolution (25ps/channel) than the ones used for these tests (50ps/channel).

3.6.3 Simulation and reconstruction

In order to study the performances of this detector, and thus evaluate the projected results of the nDVCS experiment, its geometry (Fig. 3.11) has been added to the CLAS12 GEANT4-based simulation package, GEMC [40]. The energy loss of the particle in the scintillator

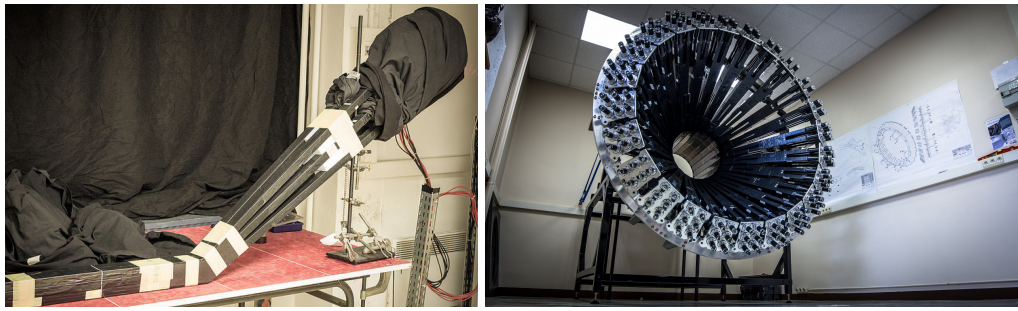


Figure 3.8: Construction and testing of the CND at Orsay. Left: one 2x3 block undergoing cosmic ray tests. Right: all 24 blocks installed into a mock-up of the CLAS12 solenoid.

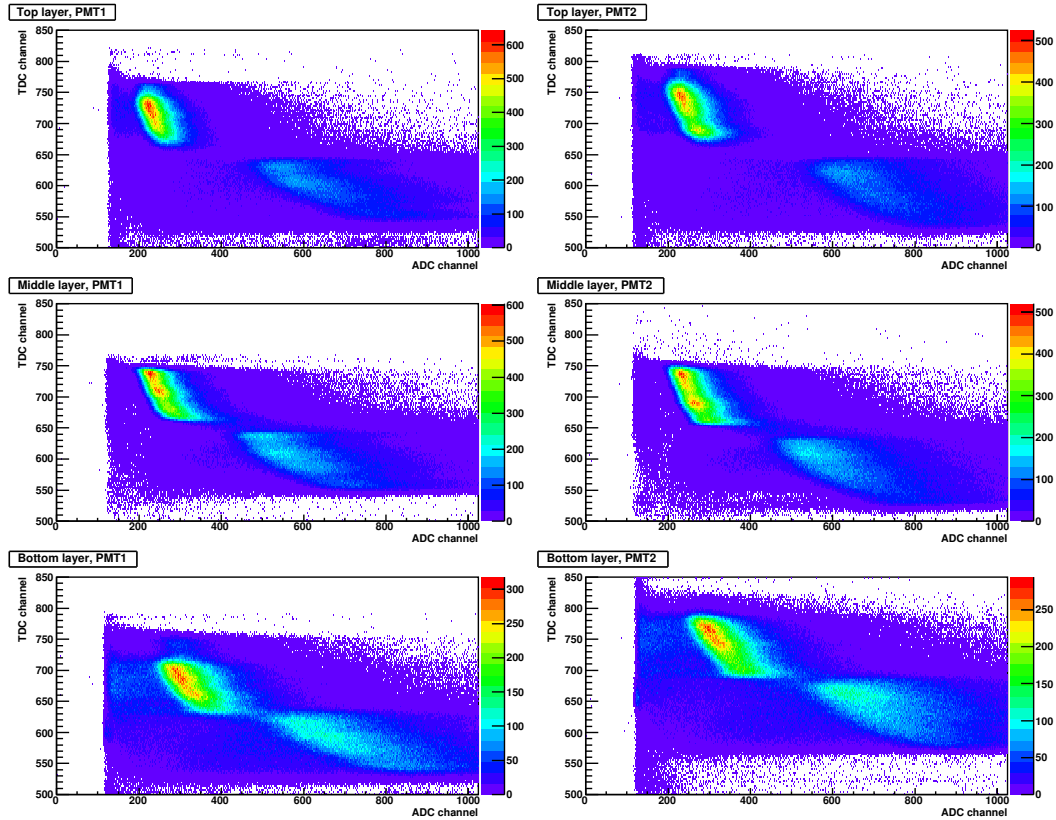


Figure 3.9: Cosmic rays data. Raw TDC vs ADC for each of the six PMTs of block 2 of the CND. No pedestal subtraction or data-cleaning cuts are applied.

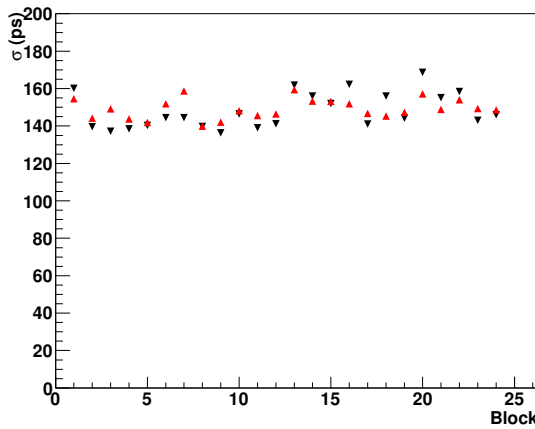


Figure 3.10: Average time resolution for each block of the CND from cosmic rays measurements in triple-coincidence. The black and red triangles are the results obtained with the formulae from, respectively, Refs. [38] and [39].

material is converted to numbers of optical photons in accordance with Birk's formula [41], the resulting signal is propagated through the scintillator paddle, light guide and PMT, and the final charge and time are digitized to mimic the output from the ADC/TDC [42].

The timing resolution and the energy loss due to the u-turn geometry have been included in the simulation using the values measured in the cosmic-rays tests described in the previous section.

Simulations, which included all the other components of the Central Detector, have been run to evaluate the efficiency of the CND for neutrons, its ability to discriminate between neutrons and photons, and its angular and momentum resolutions. Neutrons and photons of momenta varying between 0.1 and 1 GeV/c and having polar angles θ varying between 50° and 70° have been generated at fixed azimuthal angle ($\phi = 0^\circ$), pointing to the center of one of the scintillator bars. The results obtained with these simulations are described here below..

Efficiency

The detection efficiency is defined here as the ratio between the number of events for which a good hit (i.e., a hit having deposited energy above a given threshold) was successfully reconstructed as a neutron in the correct azimuthal bin of the CND and the total number of neutrons generated. Several values of energy thresholds, between 1 and 5 MeV, have been tested. The efficiency decreases with increasing threshold, and ranges between 12% at the lowest thresholds and 7% at the highest ones. Figure 3.12 shows the efficiency as a function of the momentum of the neutrons, at a fixed energy threshold of 2 MeV, and for different values of θ_n .

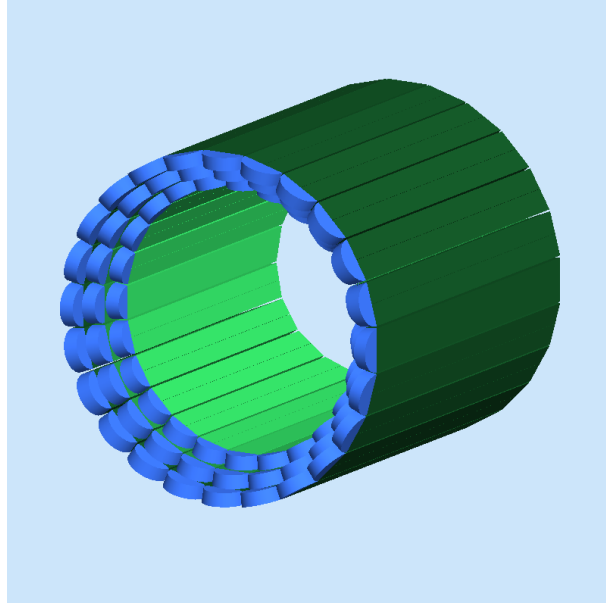


Figure 3.11: Geometry of the Central Neutron Detector in the GEMC simulation, showing three layers of scintillator paddles (green) coupled in pairs via u-turn light guides (blue) downstream.

Angular and momentum resolutions

The resolutions on the polar angle θ of the neutron that can be obtained with the CND are strongly linked to its TOF resolution. The angle θ is in fact given by

$$\theta = (180/\pi) \cdot \arccos\left(\frac{z_{ave}}{l}\right) \quad (3.23)$$

where the reconstructions of the radial distance of the hit from the target, l , and of its position along the scintillator bar, z_{ave} , both depend on the time measurement. Using a value deduced from the measurements on the CND prototype to apply a gaussian smearing on the timing [8], the θ resolution resulting from GEMC was studied as a function of neutron momentum and θ itself. The results are shown in Fig. 3.13, where the angular resolution σ_θ , obtained via gaussian fits of the simulated θ distributions, is plotted as a function of θ , for a particular value of neutron momentum (0.4 GeV/c). σ_θ is seen to increase slightly with the angle, from 1.5° to 3.5° . It has also been found to be relatively insensitive to the neutron momentum.

The resolution on the azimuthal angle is directly connected to the total number of scintillator bars along ϕ . In fact, the bin size $\Delta\phi$ is given by

$$\Delta\phi = \frac{360^\circ}{N} = 7.5^\circ \quad (3.24)$$

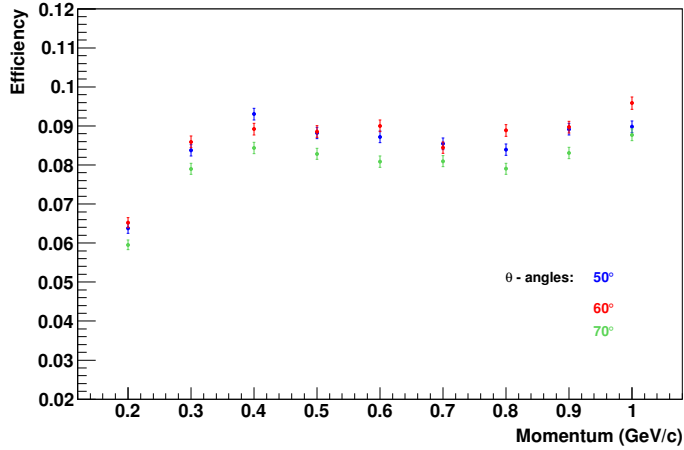


Figure 3.12: Efficiency for the detection of neutrons, as a function of neutron momentum, for a 2-MeV threshold on the deposited energy. The efficiency is shown for three different values of θ_n , between 50° and 70° .

where N is the total number of paddles in ϕ (48 for the final design of the CND). σ_ϕ can be taken as half of $\Delta\phi$, therefore 3.75° .

The resolution on the neutron momentum, calculated after particle identification on the basis of β , according to the formula

$$p = \frac{\beta \cdot m_n}{\sqrt{1 - \beta^2}}, \quad (3.25)$$

is also strictly connected to the TOF resolution. Figure 3.14 shows the momentum resolution σ_p/p as a function of momentum for neutrons emitted with $\theta = 60^\circ$: it increases with increasing momentum, and ranges between 4% and 11%. No appreciable variations of momentum resolution are observed by varying the neutron polar angle.

Particle Identification

Since the charged particles passing through the CND will be vetoed by the Central Tracker, the only particles that could be mistaken for neutrons in the CND are the photons. The efficiency of the CND for detecting photons (Fig. 3.15) has been estimated in simulations to be similar to that for neutrons, about 10% for photon energies down to 0.2 GeV. The efficiency drops to zero for lower energy photons, depending on the threshold cut applied.

Neutrons can be discriminated from photons by means of their β , and so GEMC simulations have been performed to estimate the β distributions that may be obtained from the CND. Results for one of the three radial layers, integrated over the azimuthal angle, is shown in Figure 3.16. Here β distributions for neutrons with momenta between 0.2 and 1

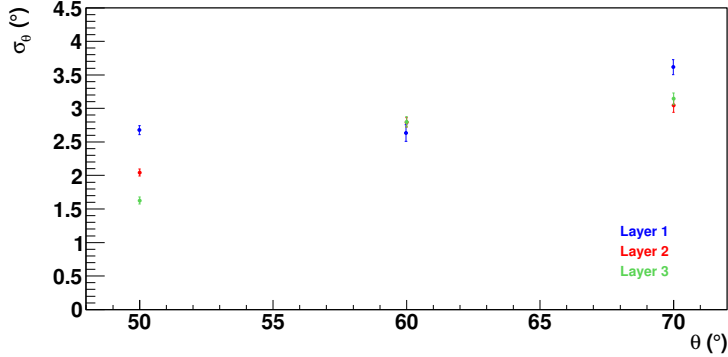


Figure 3.13: Angular resolution σ_θ as a function of θ for neutrons of momentum 0.4 GeV/c, for a 2-MeV threshold on the deposited energy. The three colors of the points correspond to the three radial layers of the CND.

GeV/c are compared with 1 GeV photons. Very clear separation is evident for neutrons less than about 0.9 GeV/c, which comprise over 90% of the expected nDVCS events.

This is evident also from Fig. 3.17, where the error bars correspond to 3σ , where σ is the gaussian width of each β distribution. Equal neutrons and photon yields have been assumed for this study. This assumption has been justified with detailed studies on the different types of photonic backgrounds that can affect the CND [8].

3.7 nDVCS at CLAS12: kinematics and acceptances

In order to study the kinematics of the reaction and determine the expected count rates for both the nDVCS signal and its main background ($ed \rightarrow en\pi^0(p)$), an event generator for DVCS/BH and exclusive π^0 electroproduction on the neutron inside a deuterium target has been developed [44]. The DVCS amplitude is calculated according to the BKM formalism [9], where the GPDs have been taken from the standard CLAS DVCS generator [45]. The Fermi-motion distribution is calculated with the Paris potential [46]. The exclusive π^0 electroproduction channel is generated assuming longitudinal dominance within the naive quark model approximation [44]. Note that no smearing effects due to the nuclear ND_3 target are included in the event generator.

The output of the event generator was fed through CLAS12 FASTMC, to simulate the acceptance and resolutions of electrons and photons in the Forward Detector.

The expected resolutions and acceptance of the CND for neutrons, outlined in the previous sections, were also included in the FastMC code.

Kinematic cuts to ensure the applicability of the GPD formalism ($Q^2 > 1 \text{ GeV}^2/\text{c}^2$, $t > -1.2 \text{ GeV}^2/\text{c}^2$, $W > 2 \text{ GeV}/\text{c}^2$) have been applied. Figure 3.18 shows the coverage in Q^2 , x_B and t that is obtained from the event generator for the nDVCS/BH reaction, with an electron-beam energy of 11 GeV.

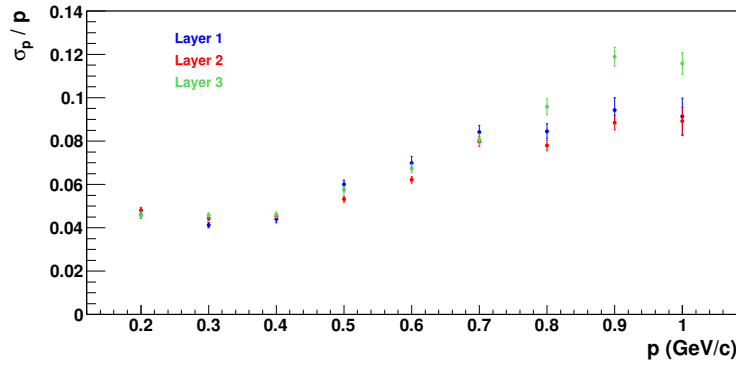


Figure 3.14: Momentum resolution σ_p/p as a function of p for neutrons having $\theta = 60^\circ$, for a 2-MeV threshold on the deposited energy. The three colors of the points correspond to the three radial layers of the CND.

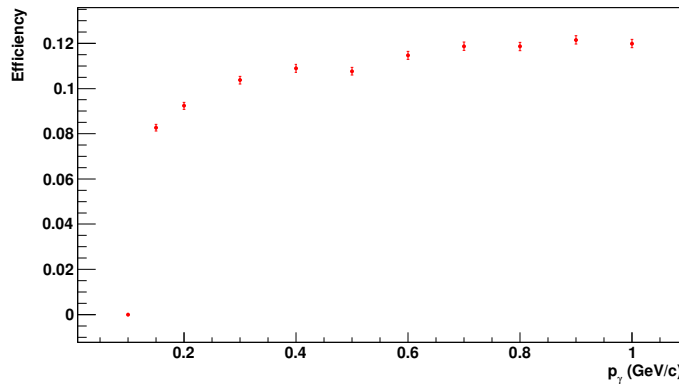


Figure 3.15: Efficiency for the detection of photons, as a function of photon momentum, for a 2-MeV threshold on the deposited energy. The efficiency is shown for $\theta_\gamma = 60^\circ$. Below $E_\gamma = 0.15$ GeV, the photon efficiency drops to zero.

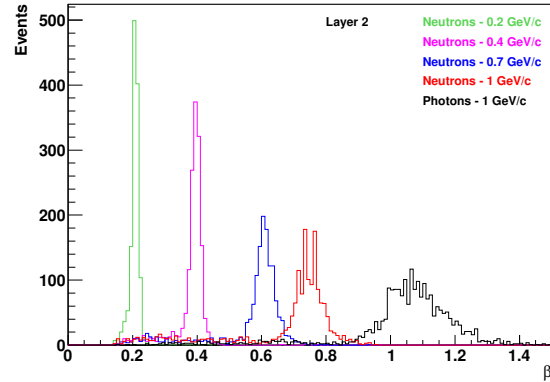


Figure 3.16: β distributions for neutrons with $p_n = 0.2 \text{ GeV}/c$ (green), $p_n = 0.4 \text{ GeV}/c$ (magenta), $p_n = 0.7 \text{ GeV}/c$ (blue), $p_n = 1 \text{ GeV}/c$ (red), and photons with $E = 1 \text{ GeV}$, for the middle layer of the CND. The threshold on the deposited energy is 2 MeV. The plots show all hits, integrated over ϕ . Equal neutron and photon yields have been assumed here.

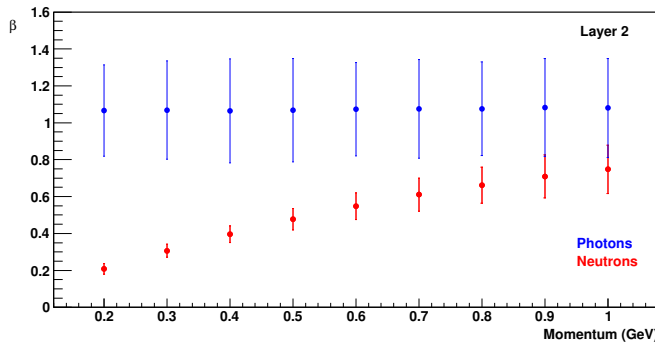


Figure 3.17: β versus momentum for neutrons (red) and photons (blue) with momenta between 0.2 and 1 GeV, for the middle layer of the CND. The error bars are defined as 3σ , where σ is the fitted width of each β peak. The threshold on the deposited energy is 2 MeV.

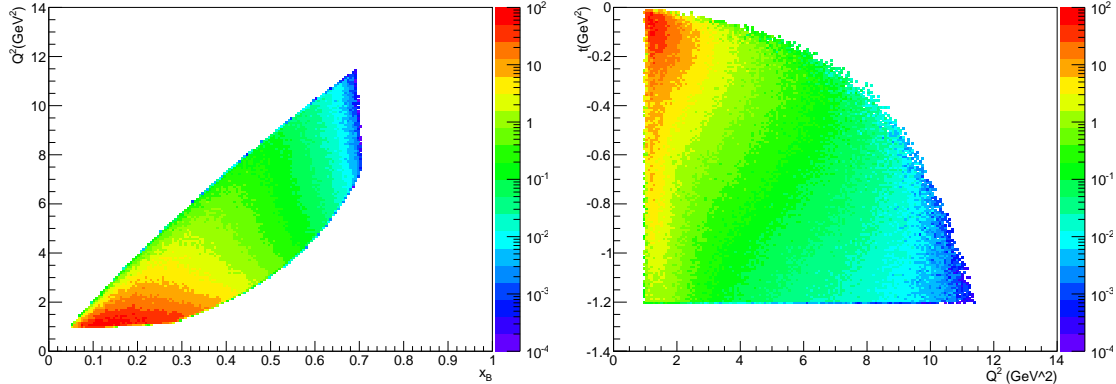


Figure 3.18: Distributions of kinematic variables for nDVCS events. CLAS12 acceptance cuts and physics cuts are included. Left: Q^2 as a function of x_B . Right: t as a function of Q^2 .

Figures 3.19, 3.20, and 3.21 show the momentum p as a function of θ in the lab frame for, respectively, the electron, the photon and the neutron. As expected, the electron and the photon are mostly emitted at forward angles, while the neutron recoils at backwards angles.

3.8 Measurement of the asymmetries

We plan to extract two kinds of asymmetries, the experimental definitions of which are given here. In all of the formulae below, the first sign in the superscript on the number of normalized DVCS/BH events N is the beam helicity (b) and the second sign is the target polarization (t). N is obtained from $e\gamma$ events ($N_{e\gamma}$), normalized by the corresponding Faraday-cup charge (FC^{bt}) after subtraction of the π^0 background as follows:

$$N^{bt} = (1 - B_{\pi^0}) \cdot \frac{N_{e\gamma}^{bt}}{FC^{bt}}, \quad (3.26)$$

where B_{π^0} is the relative π^0 contamination, outlined in Section 3.9.

The target-spin asymmetry will be computed as:

$$A_{UL} = \frac{N^{++} + N^{-+} - N^{+-} - N^{--}}{D_f(P_t^-(N^{++} + N^{-+}) + P_t^+(N^{+-} + N^{--}))}. \quad (3.27)$$

D_f is the dilution factor to account for the contribution of the unpolarized background (Section 3.10), and P_t is the polarization of the target.

The double (beam-target) spin asymmetry will be obtained as:

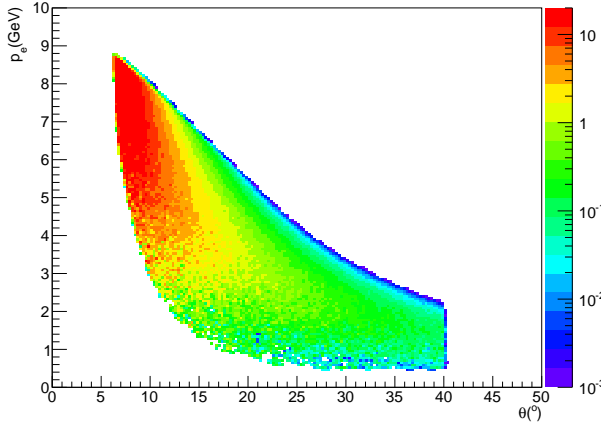


Figure 3.19: Electron momentum as a function of electron polar angle, for nDVCS events. CLAS12 acceptance cuts and physics cuts are included.

$$A_{LL} = \frac{N^{++} + N^{--} - N^{+-} - N^{-+}}{P_b \cdot D_f (P_t^-(N^{++} + N^{-+}) + P_t^+(N^{+-} + N^{--}))} \quad (3.28)$$

where P_b is the polarization of the beam.

In the following, the steps leading to the extraction from the data of all the terms composing these asymmetries will be presented.

3.8.1 Event selection and exclusivity cuts

After selecting events with exactly one electron (in the forward part of CLAS12) and one neutron (in the CND and in the EC), and at least one photon (in the EC), and applying the appropriate PID and fiducial cuts, further cuts need to be applied to ensure the exclusivity of the DVCS/Bethe-Heitler final state. Two kinds of backgrounds need, in fact, to be removed, or reduced as much as possible: the nuclear background coming from scattering on the nitrogen of the ND₃ target, and the background coming from other channels containing electron, neutron and at least one photon in the final state. Having measured the four-vectors of the three active final-state particles, one can construct several observables (hereafter referred to as “exclusivity variables”) on which cuts can be applied to select the DVCS/BH channel. Here, the following quantities were studied, with the aid of our nDVCS and $en\pi^0(p)$ simulations:

- the squared missing mass of X , in the $ed \rightarrow en\gamma X$ reaction;
- the momentum of the spectator proton, obtained as $p(X)$ from $ed \rightarrow en\gamma X$;

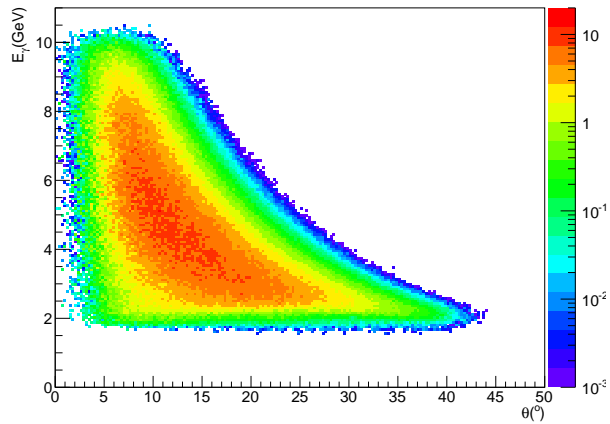


Figure 3.20: Photon momentum as a function of photon polar angle, for nDVCS events. CLAS12 acceptance cuts and physics cuts are included.

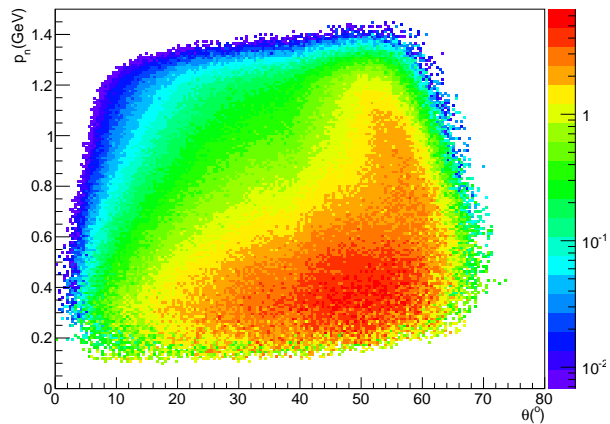


Figure 3.21: Neutron momentum as a function of neutron polar angle, for nDVCS events. CLAS12 acceptance cuts and physics cuts are included.

- the squared missing mass of X , in the $en \rightarrow en\gamma X$ reaction, assuming the initial neutron to be at rest;
- the missing energy of X , in the $ed \rightarrow en\gamma X$ reaction;
- p_{perp} , the transverse component of the missing momentum of the reaction $en \rightarrow en\gamma X$, given by $p_{perp} = \sqrt{p_x(X)^2 + p_y(X)^2}$.

Figures 3.22 and 3.23 show the exclusivity variables listed above for, respectively, nDVCS simulated events and $en\pi^0(p)$ simulated events for which only one electron, one neutron and one photon of energy above 2 GeV fell within the CLAS12 acceptance. The red lines represent the exclusivity cuts, the values of which were chosen to maximize the number of nDVCS events retained while reducing the $en\pi^0(p)$ background as much as possible. It must be stressed that the event generator adopted here does not contain Fermi motion effects coming from the nitrogen of the ND_3 target. The experimental distributions of the exclusivity variables will therefore be broader, and the peaks will be masked by the nuclear background. However, it was shown in the eg1-DVCS analysis [14] that peaks due to the pDVCS channel became evident when appropriately rescaled spectra from a ^{12}C background target were subtracted from the exclusivity variable distributions. We plan to adopt a similar approach here.

The expected $en\pi^0(p)$ contamination that remains after these cuts is shown in Fig. 3.24, where the ratio of surviving $en\pi^0(p)$ events to the number of nDVCS events is plotted as a function of ϕ , integrated over the other kinematic variables. It ranges from 0, at the extreme ϕ values, to about 40%, in the central ϕ range. This background can be evaluated and subtracted from the final asymmetries, as will be described in Section 3.9.

An exploratory nDVCS analysis on the ND_3 subset (“part C”) of the CLAS eg1-dvcs data-set is underway [47]. In spite of the very poor statistics and the far from optimal neutron reconstruction in the CLAS EC calorimeters, a selection of the nDVCS final state has been possible. Figure 3.25 shows the same exclusivity variables as are plotted in Fig. 3.22, obtained after applying nDVCS selection cuts to the $en\gamma$ event sample, which were optimised for the eg1-dvcs data. The similarities with our simulations are remarkable, especially considering that no nuclear background was subtracted from the distributions of Fig. 3.25, which gives confidence in this data-selection technique for the proposed experiment. Additionally, the effect of nuclear background subtraction can be seen in Fig. 3.26, which shows the missing mass squared from $en \rightarrow enX$ before and after subtraction of opportunely scaled distributions obtained with carbon data, and in Fig. 3.27, displaying the carbon-subtracted m_X^2 distribution from $en \rightarrow en\gamma X$. The figure indicates that a good selection of the $en\gamma$ final state has been possible even within the limitations of the eg1-dvcs experiment and illustrate the applicability of the technique to the proposed experiment.

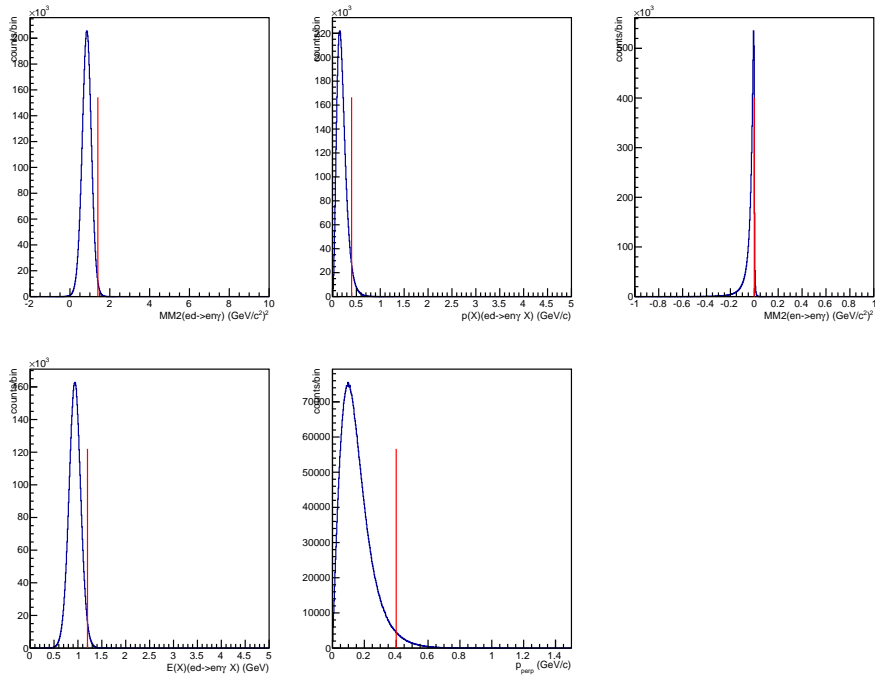


Figure 3.22: nDVCS simulation, after FastMC: DVCS exclusivity variables. Starting from the top left: $\text{MM}_X^2(\text{ed} \rightarrow \text{en}\gamma\text{X})$, $p(\text{X})(\text{ed} \rightarrow \text{en}\gamma\text{X})$, $\text{MM}_X^2(\text{en} \rightarrow \text{en}\gamma\text{X})$, $E(\text{X})(\text{ed} \rightarrow \text{en}\gamma\text{X})$, p_{perp} . The red lines mark the values adopted for the nDVCS exclusivity cuts.

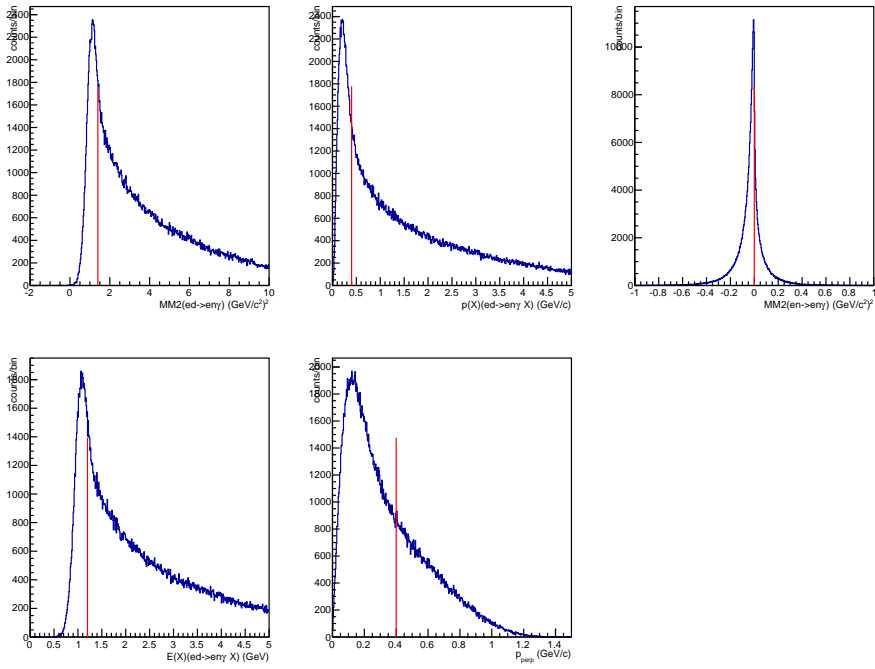


Figure 3.23: π^0 simulation, after FastMC, events for which only one electron, one neutron and one photon of energy above 2 GeV fell within the CLAS12 acceptance: DVCS exclusivity variables, same as Fig. 3.22. The red lines mark the values adopted for the nDVCS exclusivity cuts.

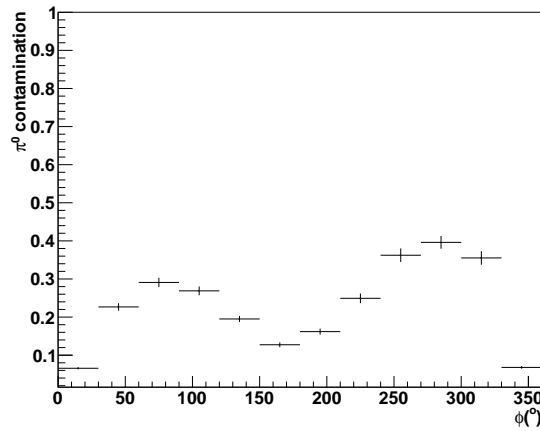


Figure 3.24: Expected π^0 contamination fraction for the proposed experiment, defined as $\frac{N_{\pi^0 1\gamma}}{N_{en\gamma}}$, as a function of ϕ and integrated over the other kinematic variables.

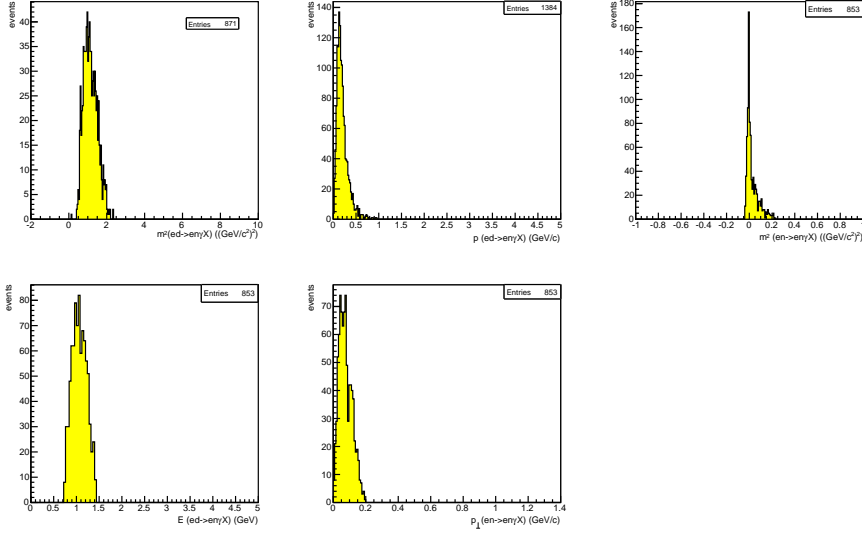


Figure 3.25: nDVCS analysis of the CLAS eg1-dvcs data set, after exclusivity cuts: DVCS exclusivity variables, same as Fig.3.22.

3.9 Neutral pion background

Once the events containing one electron, one neutron and one photon are selected, the nDVCS/BH final state can be isolated by cutting on the $en\gamma$ missing mass and other exclusivity variables. However, due to the finite resolutions of the detectors, the final event sample will still be contaminated by $en\gamma$ events coming from the $en\pi^0(p)$ channel, where one photon from the π^0 decay is detected in the forward part of CLAS12 while the other escapes detection. This contamination will be evaluated and subtracted as was done in previous DVCS CLAS analyses [16, 15, 14, 22], by extracting exclusive $en\pi^0(p)$ events — detecting both decay photons — from the data, and using Monte Carlo simulations to evaluate the ratio of acceptances of π^0 events with 1 and 2 photons detected. The final number of nDVCS/BH events, in each 4-dimensional bin, will be obtained as:

$$N_{DVCS}(Q^2, x_B, -t, \phi) = N_{en\gamma}(Q^2, x_B, -t, \phi) - N_{\pi^0 1\gamma}(Q^2, x_B, -t, \phi) \quad (3.29)$$

where

$$N_{\pi^0 1\gamma}(Q^2, x_B, -t, \phi) = N_{\pi^0}^{data}(Q^2, x_B, -t, \phi) \cdot \frac{N_{\pi^0 1\gamma}^{MC}(Q^2, x_B, -t, \phi)}{N_{\pi^0 2\gamma}^{MC}(Q^2, x_B, -t, \phi)} \quad (3.30)$$

As an example, Fig. 3.28 shows the elements contributing to the π^0 background subtraction, as were evaluated for the extraction of the TSA in the CLAS eg1-dvcs analysis, for two particular kinematic bins in $(Q^2, x_B, -t)$. Note that the impact on the final asymmetry

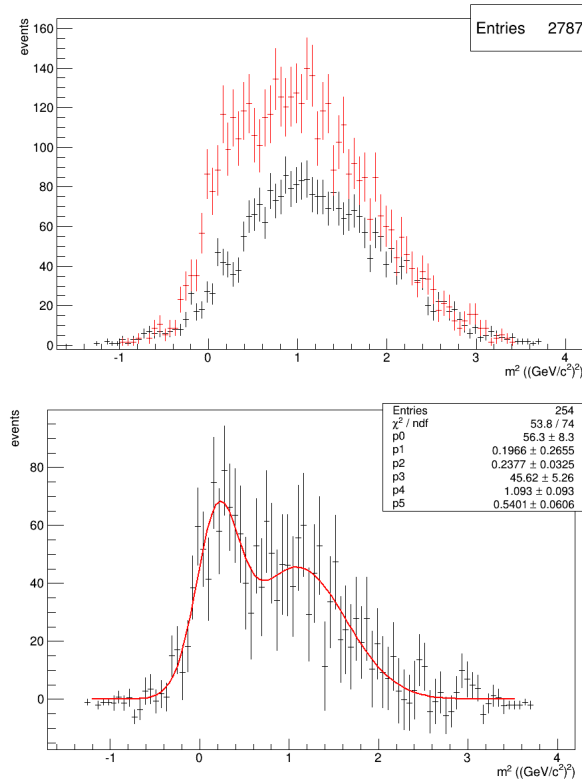


Figure 3.26: nDVCS analysis of the CLAS eg1-dvcs data set. Left: squared missing mass of X in $en \rightarrow enX$, with ND₃ (red) and carbon (black); right: after carbon subtraction, a peak near 0 appears.

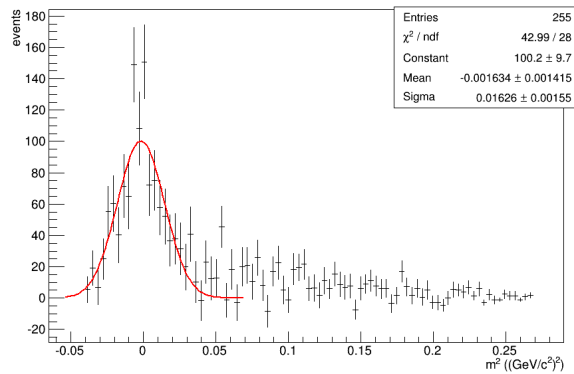


Figure 3.27: nDVCS analysis of the CLAS eg1-dvcs data set: squared missing mass of X in $en \rightarrow en\gamma X$, after exclusivity cuts and carbon subtraction.

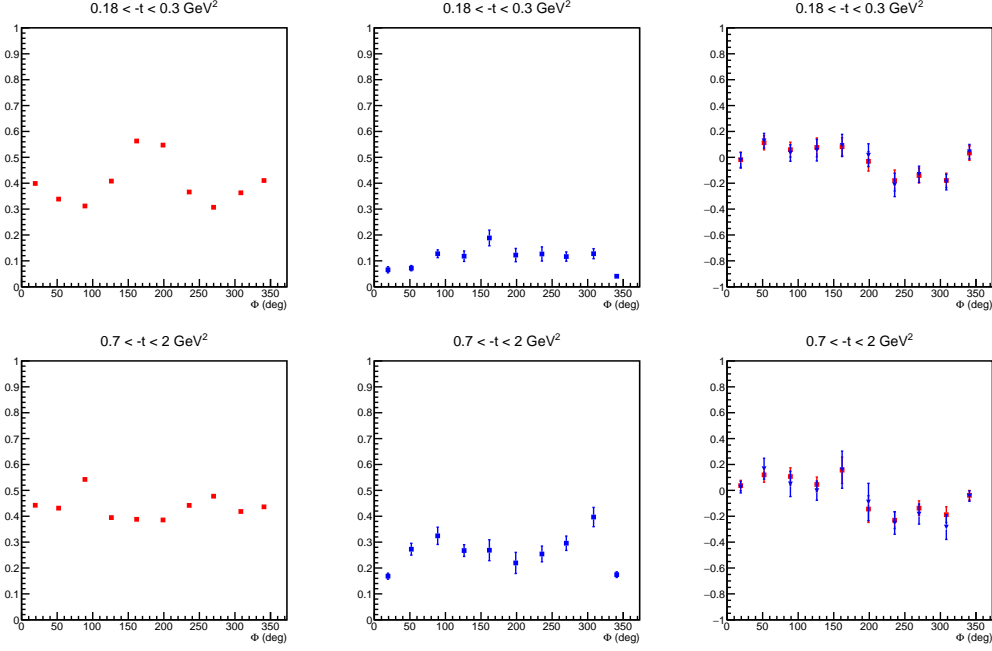


Figure 3.28: Plots from the proton-DVCS analysis of the eg1-DVCS CLAS dataset [14], for two different kinematic bins (top and bottom). Left: Acceptance ratio $\frac{1}{2\gamma}$; middle: π^0 contamination fraction; right: target-spin asymmetry before (red) and after (blue) π^0 background subtraction.

of the background subtraction is quite small: an average effect of roughly 10%, relative to the value of the TSA at 90° , was estimated for this data set. In fact, what will impact the final asymmetries is not the size of the contamination itself, but the point-by-point difference of contamination for positive and negative target (or beam-target) polarization.

The proton-DVCS analysis of the eg1-dvcs NH₃ dataset showed that a combination of optimized cuts on the exclusivity variables, designed to minimise the background, and the simulation- and data- based subtraction of Eq. 3.30 to remove the remaining contamination was a sound technique. In terms of systematics, the asymmetries were minimally affected even when the background estimation was artificially varied by 30%. This is important also because it shows how little this procedure depends on the Monte-Carlo model adopted.

3.10 Dilution factor

For both the nDVCS and $en\pi^0$ final states, dilution factors are necessary to correct the experimental yields for the contribution from the scattering on the unpolarized nitrogen of ND₃. The dilution factor, that will be determined using data taken on ND₃ and on ¹²C

targets, is defined as

$$D_f = 1 - c \cdot \frac{N_{^{12}\text{C}}}{N_{^{14}\text{ND}_3}}. \quad (3.31)$$

Here, $N_{^{12}\text{C}}$ is the number of events, normalized by the corresponding Faraday-cup counts, obtained from a carbon target and surviving all of the nDVCS (or $en\pi^0$) selection cuts, while $N_{^{14}\text{ND}_3}$ is the number of events, likewise normalized and passing the same series of cuts, originating from ND_3 . The factor c accounts for the different luminosities of the two sets of data, which also take into account the different areal densities of the materials present at the target level for the two kinds of runs (ND_3 in the numerator, ^{12}C in the denominator). For the eg1-dvcs experiment, it was found that the dilution factor, which, for pDVCS was determined to be around 0.9, does not display any sizeable dependence on any of the four kinematic variables describing the DVCS process. Adopting the same ratio as in eg1-dvcs, we estimate that acquiring ten times less events on ^{12}C than on ND_3 should provide a sufficient count rate of carbon events to estimate the dilution factor at a satisfactory level of precision. A value of about 0.8 was obtained in recent studies of exclusive channels on ND_3 , still using the eg1-dvcs dataset [48].

3.11 Accidentals in the CND

In order to evaluate the rate of accidentals being reconstructed as a false neutron in the CND in coincidence with an $e\gamma$ event detected in CLAS12, GEMC simulations have been run in the following conditions [49, 8]: the primary electron has been generated going forward (to simulate the real hadronic event), plus 7500 other electrons have been thrown, distributed in a 124 ns window in bunches 4 ns apart, originating 10 cm upstream of the target. 7500 is approximately the number of beam electrons that would pass through our target in a 124 ns time window at the nominal CLAS12 luminosity. 124 ns is the typical time window of the DAQ expected for CLAS12, which corresponds to one event in CLAS12. These electrons then interact with the target itself, producing an electromagnetic and hadronic background hitting the neutron detector. The simulations were produced twice, using two different "physics lists" from GEANT4: electromagnetic plus hadronic processes ("EM-HAD"), and electromagnetic only (EM). The output of the simulations has been analyzed using the CND neutron-reconstruction algorithm. For each event, we selected the hit with the shortest time of flight which had a deposited energy above our chosen threshold (2 MeV) and below the maximum allowed time (9 ns). The reference time was chosen as that corresponding to the central beam bunch. Given the tight timing cuts that are imposed when reconstructing neutrons in the CND, we estimate that only slow neutrons ($p \sim 0.2$ GeV) from the previous bunch or photons from the following bunch could be accidentally registered as originating from the bunch in question. The momentum of the chosen particle is reconstructed assuming that it is a neutron, and cuts are applied on its momentum ($p_{min} = 0.2$ GeV/c) and on β ($\beta < 0.95$). Since previous simulations showed us that real neutrons should only produce at most one hit in one of the three layers

of the CND, particles which had a second hit in another layer along the same trajectory were also removed. Figure 3.29 shows the energy distribution of the background hits in the CND before any cuts are applied for the EM (top) and EM-HAD (bottom) cases. The latter has a more important tail at higher energies.

The resulting probabilities that an event has a hit which passes the CND cuts are 0.0012 for the EM case and 0.01 for the EM-HAD case. Care must be taken in considering the EM-HAD probability, as there can be, on the one hand, double counting due to some of the simulated hadronic events producing actual triggers in CLAS12, and, on the other hand, uncertainties due to the GEANT4 parametrization of the physics list. The GEMC simulation of the whole CLAS12 and the full reconstruction software would be necessary to provide a more accurate estimate, but neither are available yet. The 0.01 of the EM-HAD case must therefore be regarded as a conservative upper limit. These hits can mimic a fake n-DVCS event by accidental coincidence with hadronic events where an electron and an energetic photon ($E_\gamma > 2$ GeV) are detected in the forward part of CLAS12. The $e\gamma$ rate was estimated to be at most 50 Hz: the dominant process at play here is SIDIS with production of a π^0 ; the rate for such a process was estimated in [50] to be of 9 Hz (obtained by taking into account the factor of 20 greater luminosity in the present experiment). Given that various kinematic cuts and the detection of both photons were required to produce that figure, we take a very conservative approach, assuming a rate for such events of the order of 50 Hz. This yields an accidental coincidence rate of the order of 0.06 Hz for the EM physics list, and 0.5 Hz for the EM+HAD physics list. These figures will be further reduced once the exclusivity cuts (Section 3.8.1) will be applied, and will be therefore safely smaller than the expected rate for real $e\gamma$ events, which was estimated, with our event generators and FastMC, to be of 1 Hz for the present experiment.

3.12 Forward Tagger option

This section may change a bit during the CLAS review because simulations are ongoing with new FT and shielding designs in GEMC In order to maximize the acceptance for forward-emitted photons, the possibility of including the Forward Tagger is being considered. It is part of the setup for the approved polarized proton-DVCS CLAS12 experiment [24]. To minimize the radiation damage of the target, the beam must be rastered over its surface. When the Forward Tagger is included in the CLAS12 setup, the Moller shielding around the beamline is reduced, compared to the shielding for the non-FT configuration, in order not to block low-angle photons. This may produce backgrounds in the drift chambers, which can in turn affect the quality of the tracking of charged particles in the Forward Detector. Simulations were performed to study the occupancy levels for the first region of the CLAS12 drift chambers (DC). The GEMC simulation program was used and the ND₃ target cell was added to it. The polarized target was implemented as a cylindrical cell of teflon with radius of 2.5 cm and length of 4 cm, filled with a mixture of 60% ND₃ and 40% liquid helium. The simulation was run with background events produced in a time window

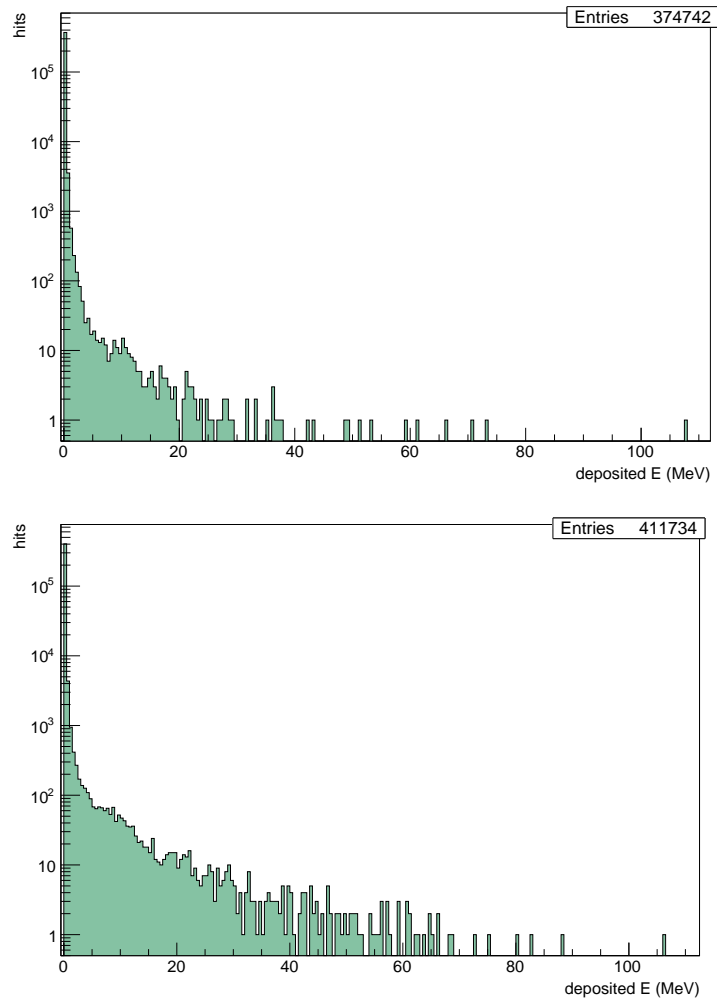


Figure 3.29: Energy deposited by the background hits in the CND, before cuts, as obtained with GEMC plus the EM physics list (top) and the EM-HAD one (bottom).

of 250 ns with a beam current of 10 nA, corresponding to 15625 electrons, spread over a circular surface of 1.2 cm of diameter. Four possible configurations, “with or without Forward Tagger” combined with “with or without raster”, were studied, for comparison purposes. Table 3.2 shows the results for the four configurations and Fig. 3.30 shows an example of the occupancy for DC region 1. Note that typical rates for a liquid hydrogen target (thus without rastered beam) with a luminosity of 10^{35} are 2.5% with the FT and 1% without FT. While the occupancy of the first region is rather high in the proposed configu-

Configuration	Occupancy
FT + no raster	5%
FT + raster	8%
no FT + raster	2.2%
no FT + no raster	2%

Table 3.2: Occupancy for the first region of the CLAS12 drift chambers, for different configurations of the rastered beam and the Forward Tagger.

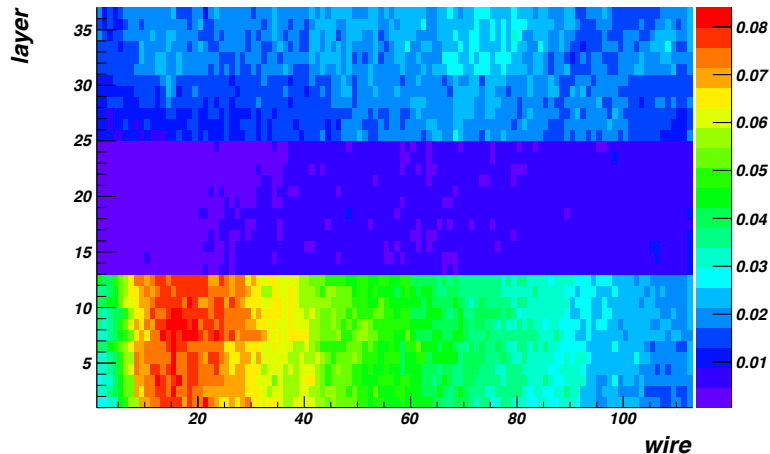


Figure 3.30: Occupancy in the first region of the CLAS12 drift chambers, for the configuration with FT and rastered beam.

ration for this experiment, it is not yet clear at this stage what the limit is for the acceptable DC occupancy in CLAS12 to ensure proper tracking, as the tracking reconstruction software is still under development. Preliminary studies [51] suggested that tracking should be possible with DC occupancies up to 8-10%. A definitive answer on this issue can only come when CLAS12 commissioning data will be taken at different beam currents and analyzed with the appropriate tracking and reconstruction software. This proposal is based on the hypothesis that the Forward Tagger can not be used, for the above described reasons. However, if the tracking will prove to be feasible at such levels of DC1 occupancies, the introduction of the Forward Tagger in the setup of this experiment could be beneficial (see Section 3.13 to see the projected asymmetries with and without inclusion of the FT).

3.13 Projected results

A GPD-based event generator for DVCS-BH on a deuterium target was run, assuming a luminosity of $3/20 \cdot 10^{35} \text{ cm}^2 \text{ s}^{-1}$ (where the factor 3/20 accounts for the ratio of polarized neutrons to the total nucleons in ND₃) and a beam time of 100 days. The output of the generator was fed to the CLAS12 Fast-MC code, which included acceptance and resolution effects for CLAS12 and the CND. An additional factor of 10% was also applied to mimick the efficiency of the CND for neutrons⁷. nDVCS exclusivity cuts were then applied. This way, the expected yields for the $e\gamma(p)$ events produced on the ND₃ target were obtained. The kinematic space (in $Q^2, x_B, -t, \phi$) available with the acceptance of the CLAS12+CND setup was divided into the same 4-dimensional grid that was used for the unpolarized nDVCS proposal:

- 4 bins in Q^2 , the limits of which are: 1, 2, 3.5, 5, 10 (GeV)²;
- 4 bins in x_B , the limits of which are: 0.05, 0.15, 0.3, 0.45, 0.7;
- 4 bins in $-t$, the limits of which are: 0, 0.2, 0.5, 0.8, 1.2 (GeV)²;
- 12 bins in ϕ .

The central kinematics for each bin were computed as weighted averages over the reconstructed events. The target-spin asymmetry and the double-spin asymmetry were then calculated as a function of ϕ using the VGG model (with input parameters $J_u = 0.3$ and $J_d = 0.1$) for each of the $(Q^2, x_B, -t)$ bins that are kinematically allowed. Statistical errors were then obtained for these asymmetries using the approximated formula:

$$\sigma_A = \frac{1}{P} \cdot \frac{\sqrt{1 - P^2 \cdot A^2}}{\sqrt{N}}. \quad (3.32)$$

where P is the polarization (and it is therefore equal to the target polarization for neutrons, P_t , for the TSA case, and to the product of beam and target polarizations, $P_b P_t$, for the DSA case), and N is the expected yield in each 4-dimensional bin.

The resulting asymmetries with the associated expected error bars are shown in Figs. 3.31 and 3.33. The use of the Forward Tagger would improve the ϕ coverage at the edges ($\phi \rightarrow 0^\circ$ and $\phi \rightarrow 360^\circ$) for a few kinematic bins, but for the majority of bins there is no effect.

It is important to point out that the number of days chosen here (100) is the minimal amount of time necessary to be able to bin the TSA and the DSA in enough kinematic bins to describe in a satisfactory manner the dependence in all the 4 kinematic variables, while at the same time having statistical uncertainties not exceeding too much the ones expected

⁷Actually, this factor was adopted globally for ALL neutrons, even those falling within the EC acceptance. Given that the EC should have higher neutron efficiency than the CND, by at least a factor of 2, the projections for the count rates shown here are slightly pessimistic.

for the BSA of E12-11-003 (Fig. 3.35). The comparison of TSA and BSA, for running this experiment with either 50 or 100 days of beam time, is shown in Figs. 3.32 and 3.34, respectively.

3.14 Extraction of Compton Form Factors

The three sets of projected asymmetries (BSA from [8], shown in Fig. 3.35, TSA and DSA from this work, Figs. 3.31 and 3.33, respectively) for all kinematic bins were processed using the fitting procedure described in Section 3.4 to extract the Compton Form Factors of the neutron. In the adopted version of the fitter code, $\tilde{E}_{Im}(n)$ is set to zero, as $\tilde{E}(n)$ is assumed to be purely real - it is parametrized in the VGG model by the pion pole ($1/(t - m_\pi^2)$). Thus, seven out of the eight real and imaginary parts of the CFFs are left as free parameters in the fit. A loose bound on the parameters is also applied, limiting them within the interval given by $\pm 5 \cdot \text{VGG}$, where "VGG" stands for the prediction of the VGG model for the value of the CFF.

The results for the 7 neutron CFFs are shown in Figs. 3.36-3.42, as a function of $-t$, and for each bin in Q^2 and x_B . The blue points are the CFFs resulting from the fits with their asymmetric error bars, which reflect both the statistical precision of the fitted observables and their sensitivity to that particular CFFs. Only results for which both halves of the error bars are non zero, and therefore the fits have properly converged for that CFF, are included here.

The CFFs which will be obtained with more precision and for most of the kinematic points that will be covered by the proposed experiment are $H_{Im}(n)$ and $E_{Im}(n)$. This is to be expected, since the TSA and the BSA are most sensitive to these two CFFs. A quite good sensitivity to $\tilde{E}_{Re}(n)$ seems possible in a wide kinematics range. $\tilde{H}_{Re}(n)$ will also be obtained in most of the kinematic bins, thanks to the peculiar sensitivity of the DSA for this CFF. $\tilde{H}_{Im}(n)$ will be well extracted only in the low Q^2 - x_B kinematics. Finally, it appears that these data will not be able to provide much information on $E_{Re}(n)$. **NOTE for the review committee: Comparative plots showing CFF obtained with 50 and 100 days will come in the next edition of the proposal.**

3.15 Flavor separation of CFFs

In order to convey the impact of this experiment on the JLab GPD program, an example of model-independent flavor separation of CFFs, which our experiment will make possible for the first time, is shown in Figs. 3.43 and Figs. 3.44. Here, the CFFs H_{Im} (Fig. 3.43) and E_{Im} (Fig. 3.44) are shown, for two different bins in Q^2 - x_B (left-right), as a function of $-t$, for the two nucleons (top, where the proton is represented in black and the neutron in red) and for the two quark flavors (bottom, where black represents u and red d). These figures has been produced using the proton CFFs that were extracted combining all the

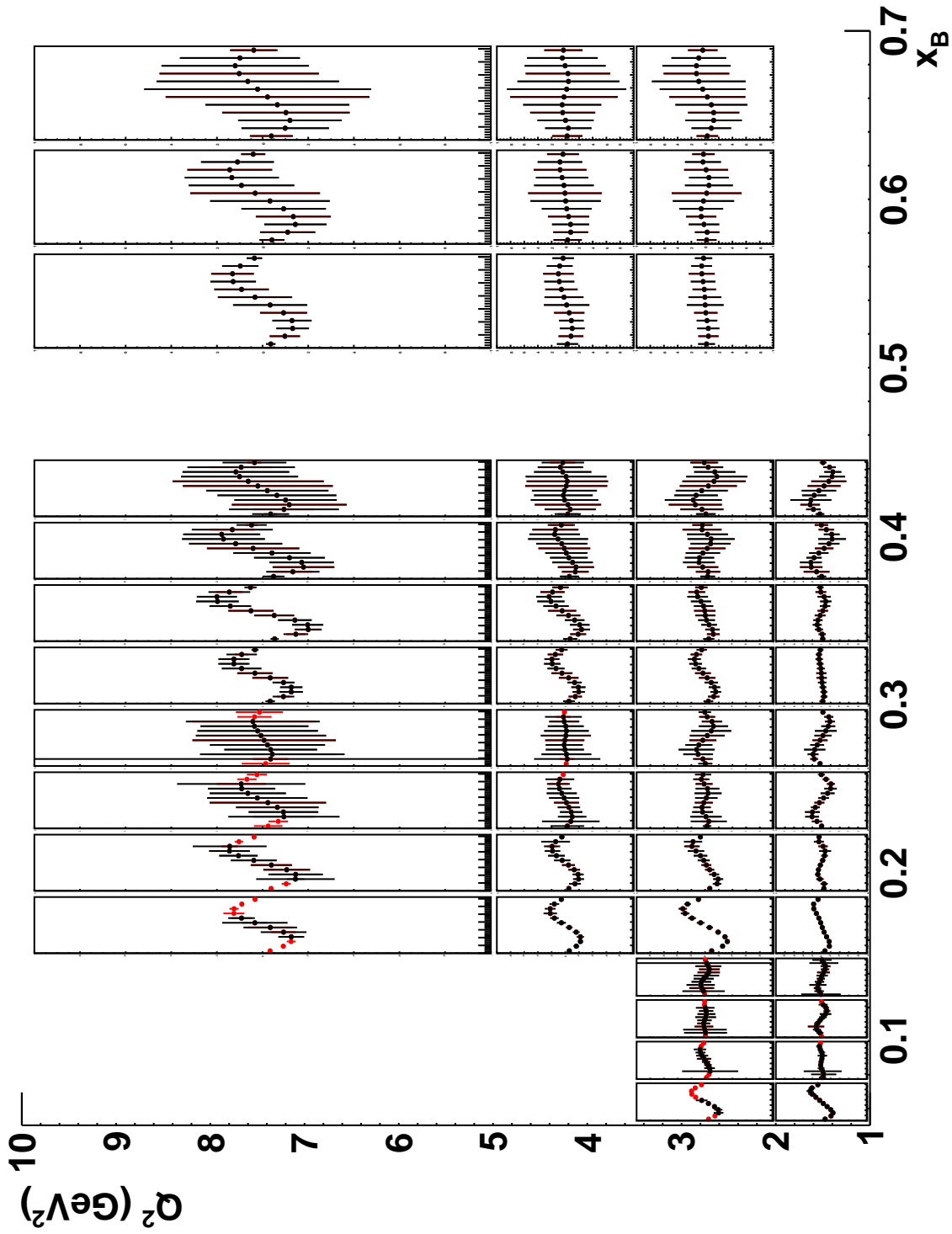


Figure 3.31: Projected target-spin asymmetry. The y-scale range, common to all bins, is (-1:1). The black and red points are obtained, respectively, without and with the Forward Tagger.

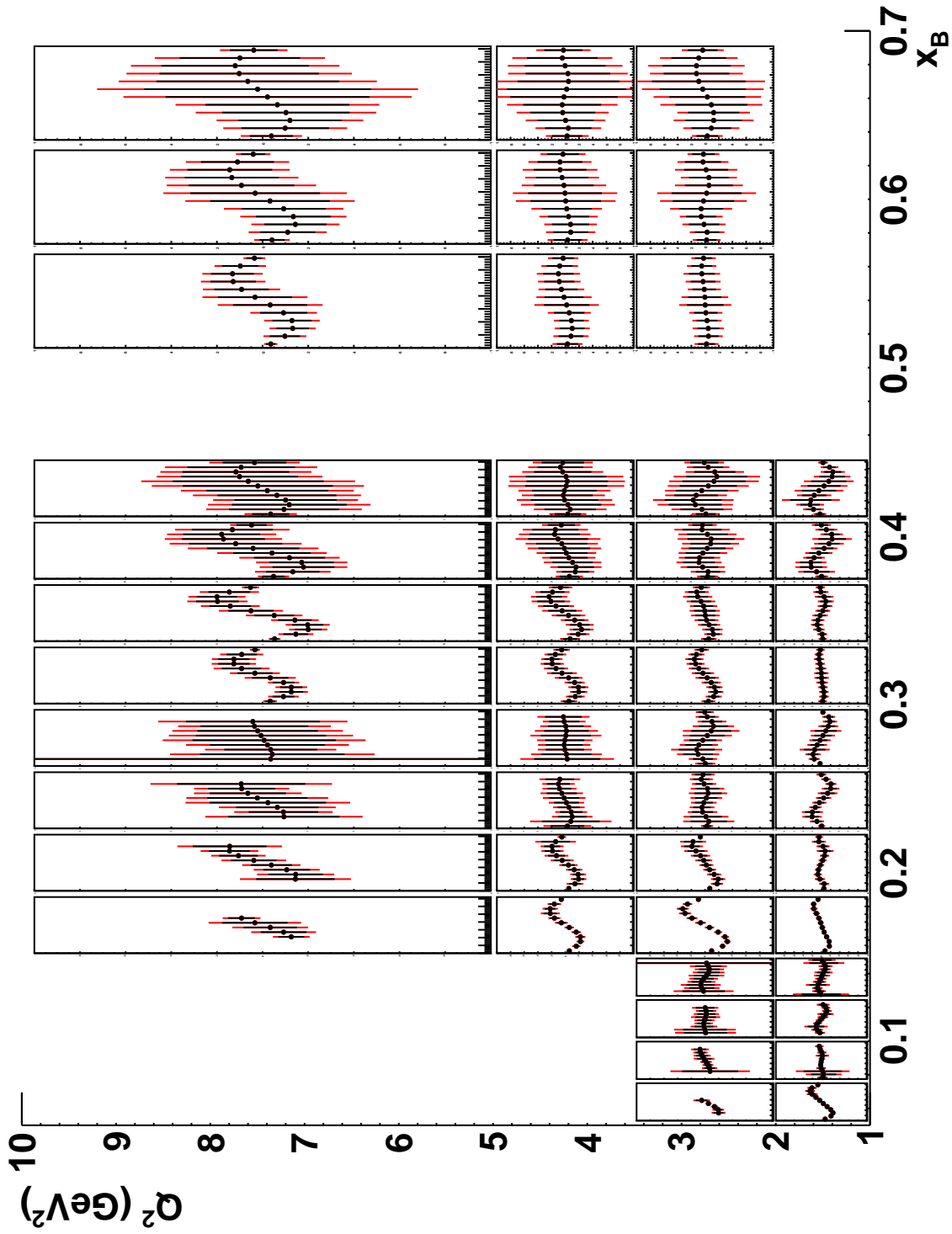


Figure 3.32: Projected target-spin asymmetry. The y-scale range, common to all bins, is (-1:1). The black and red points are obtained, respectively, with 100 and 50 days of beamtime.

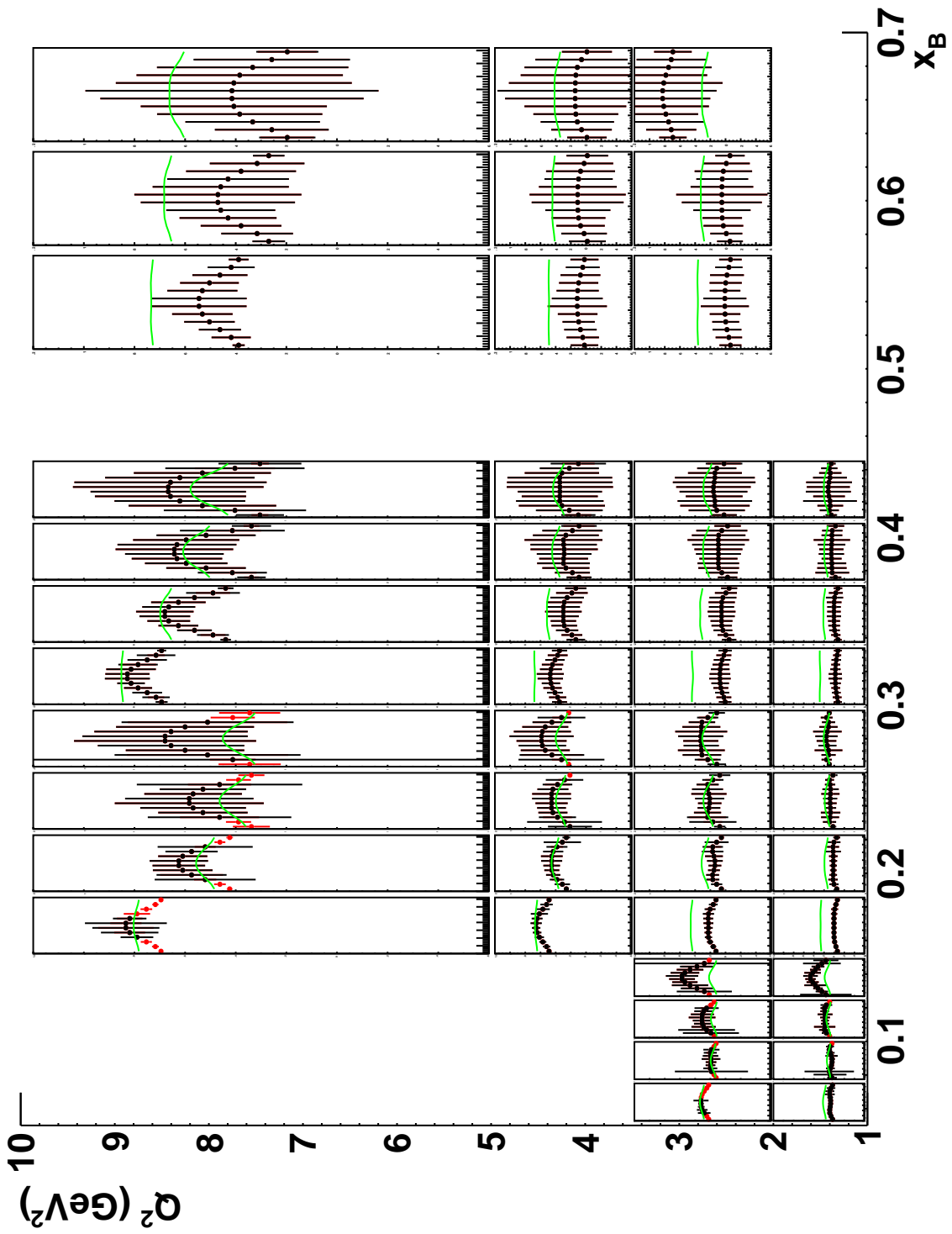


Figure 3.33: Projected double-spin asymmetry, compared with the BH (green lines), calculated at the average kinematics of each bin. The y-scale range, common to all bins, is -0.6-1.2. The black and red points are obtained, respectively, without and with the Forward Tagger.

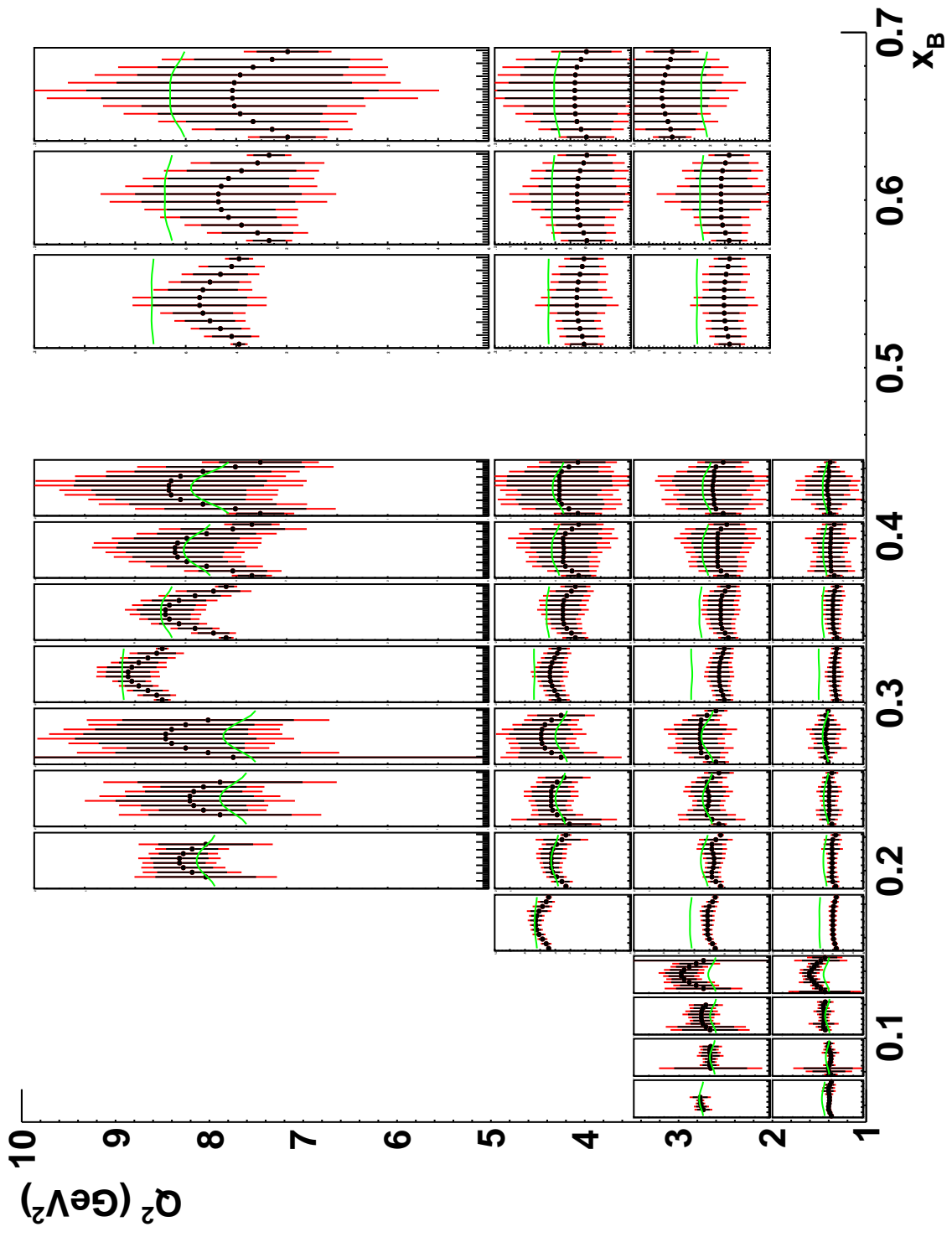


Figure 3.34: Projected double-spin asymmetry, compared with the BH (green lines), calculated at the average kinematics of each bin. The y-scale range, common to all bins, is -0.6-1.2. The black and red points are obtained, respectively, with 100 and 50 days of beamtime.

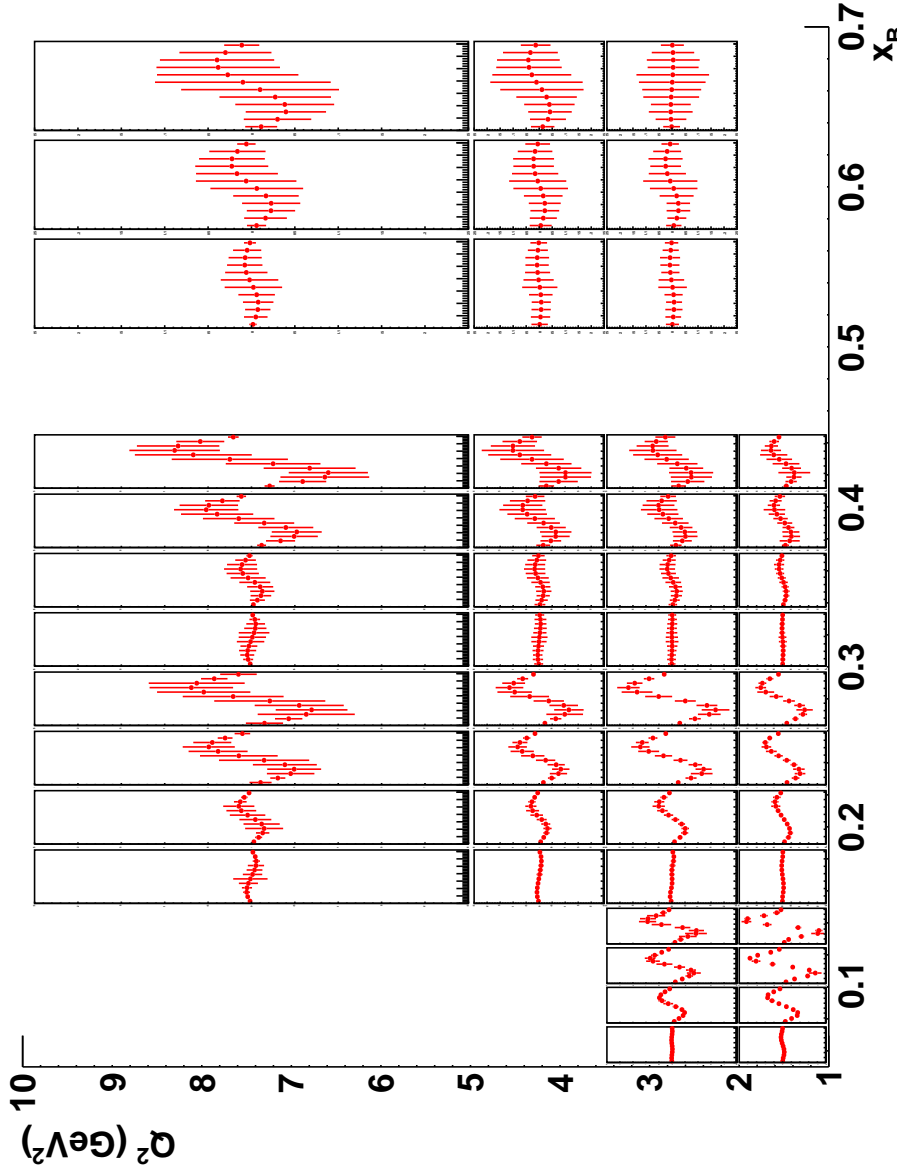


Figure 3.35: Projected beam-spin asymmetry, as will be obtained from experiment E12-11-003 [8]. The y-scale range, common to all bins, is -0.25-0.25.

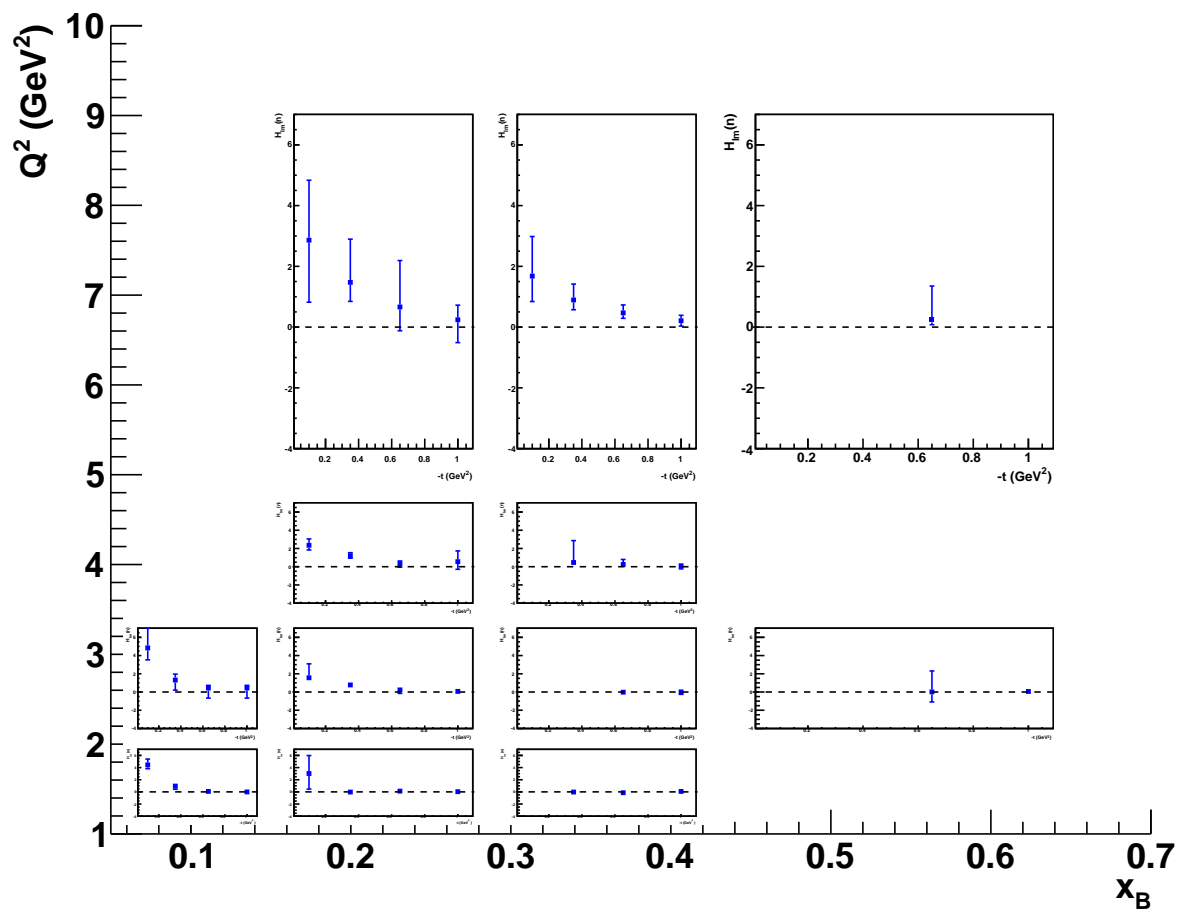


Figure 3.36: $H_{Im}(n)$ as a function of $-t$, for each bin in Q^2 and x_B . The y scale is common to all bins. The dashed line marks $y = 0$.

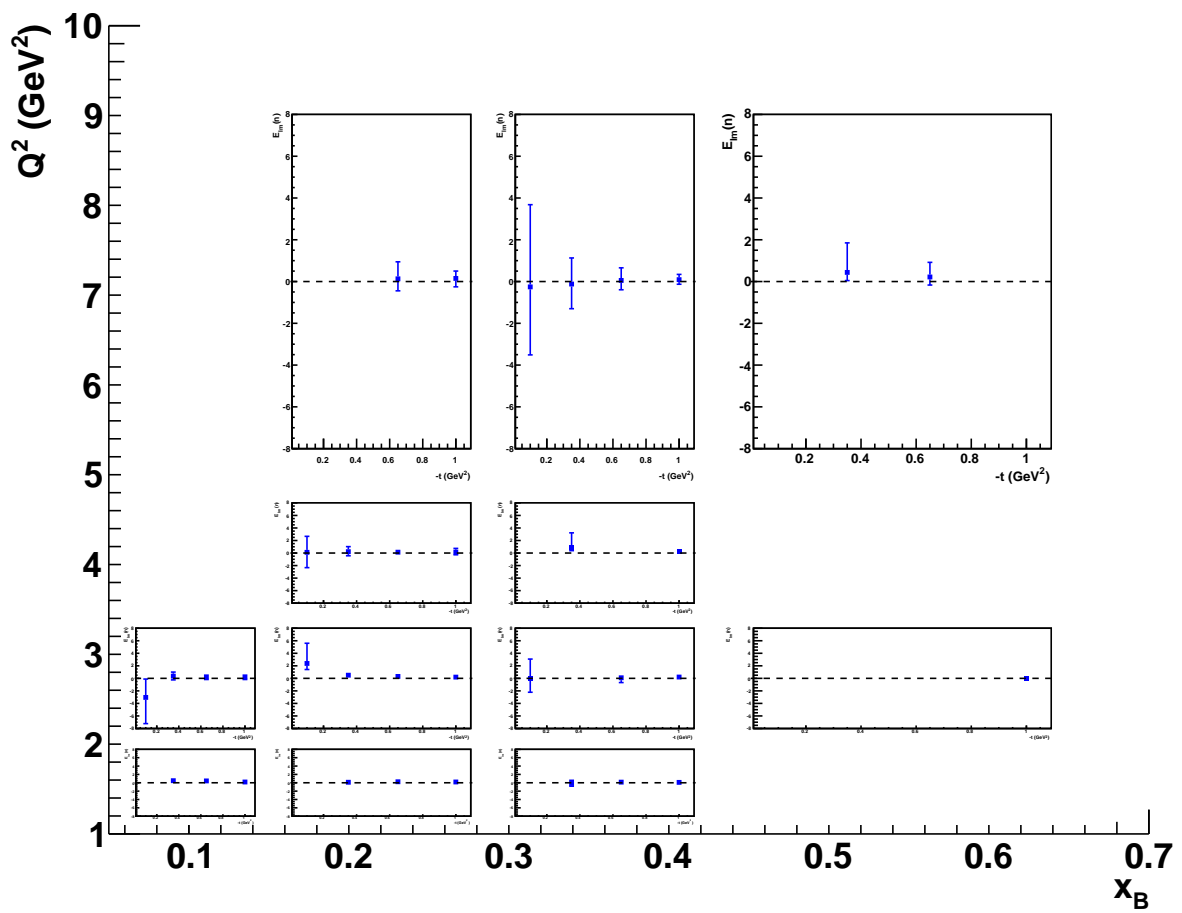


Figure 3.37: $E_{Im}(n)$ as a function of $-t$, for each bin in Q^2 and x_B . The y scale is common to all bins. The dashed line marks $y = 0$.

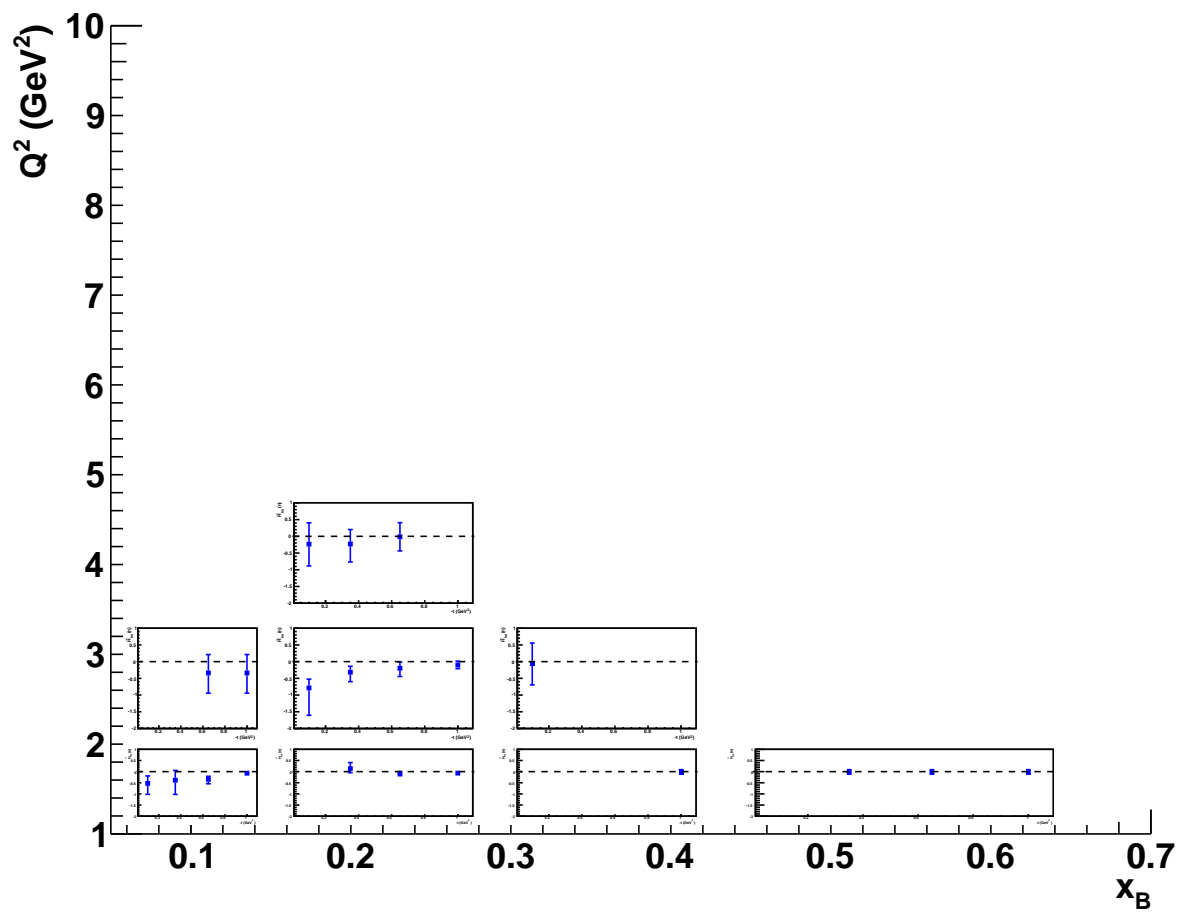


Figure 3.38: $\tilde{H}_{Im}(n)$ as a function of $-t$, for each bin in Q^2 and x_B . The y scale is common to all bins. The dashed line marks $y = 0$.

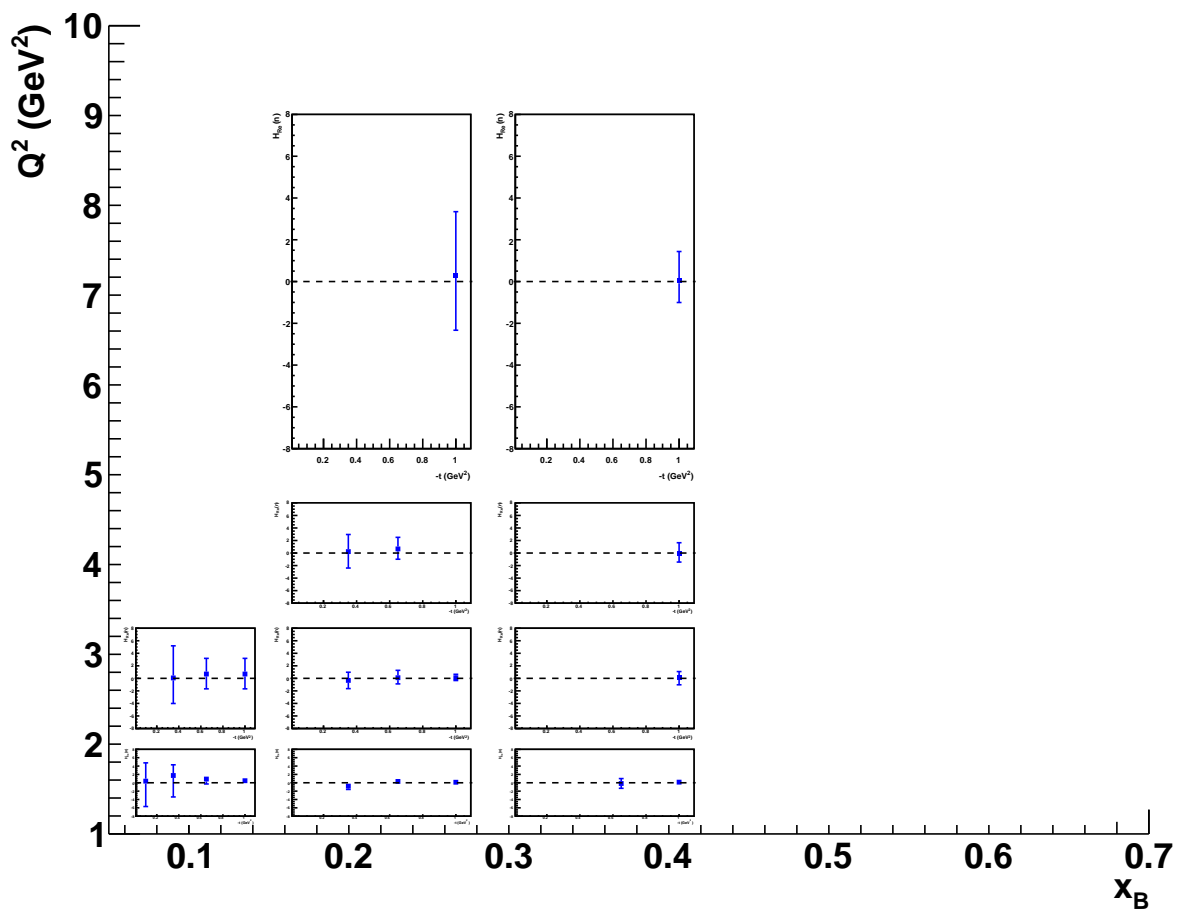


Figure 3.39: $H_{Re}(n)$ as a function of $-t$, for each bin in Q^2 and x_B . The y scale is common to all bins. The dashed line marks $y = 0$.

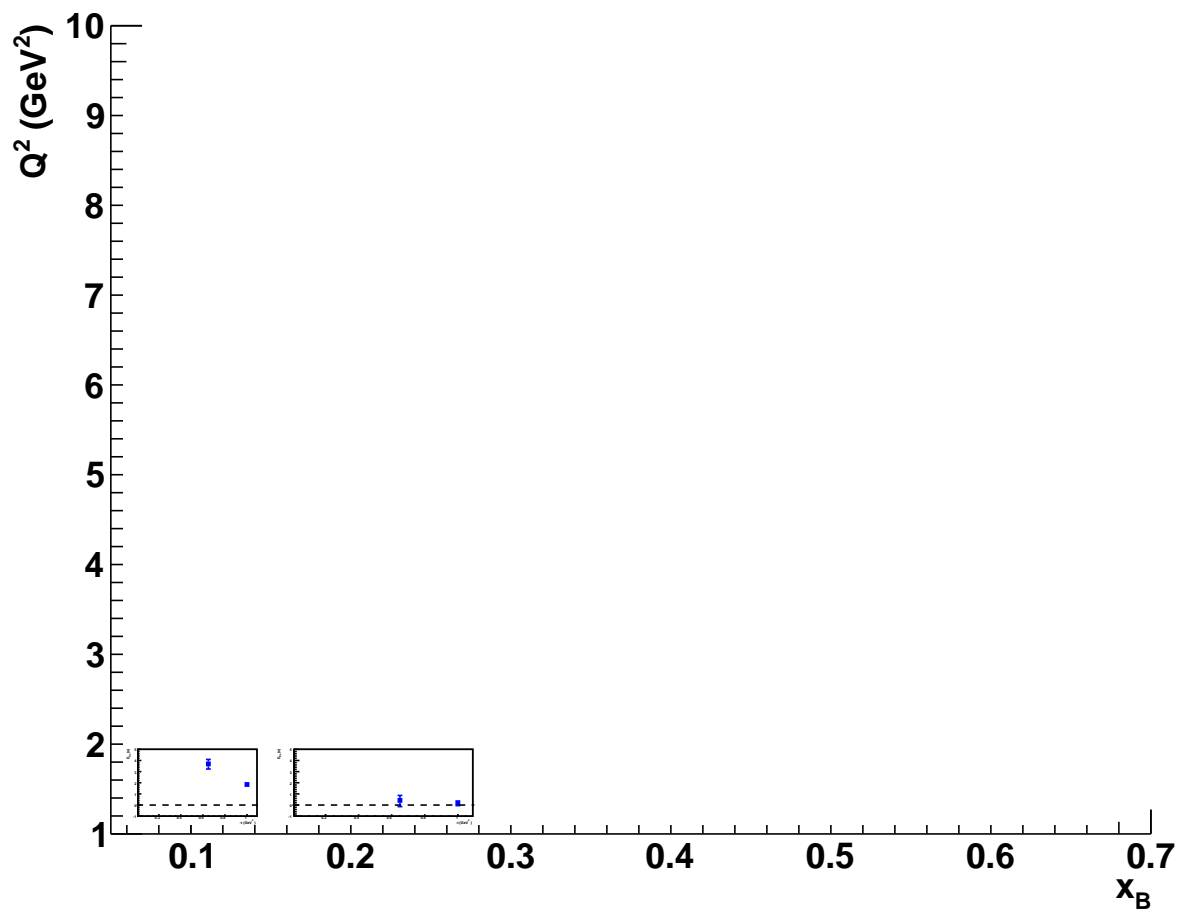


Figure 3.40: $E_{Re}(n)$ as a function of $-t$, for each bin in Q^2 and x_B . The y scale is common to all bins. The dashed line marks $y = 0$.

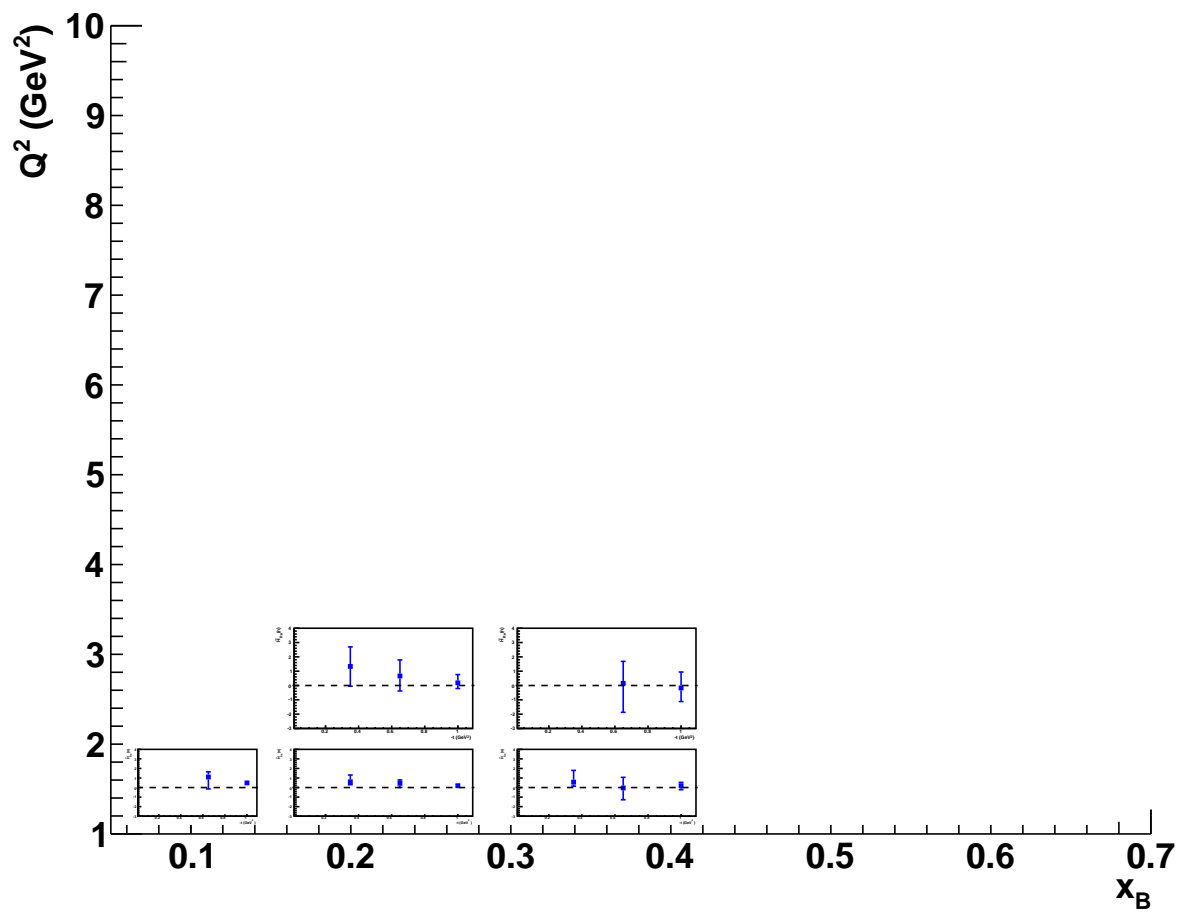


Figure 3.41: $\tilde{H}_{Re}(n)$ as a function of $-t$, for each bin in Q^2 and x_B . The y scale is common to all bins. The dashed line marks $y = 0$.

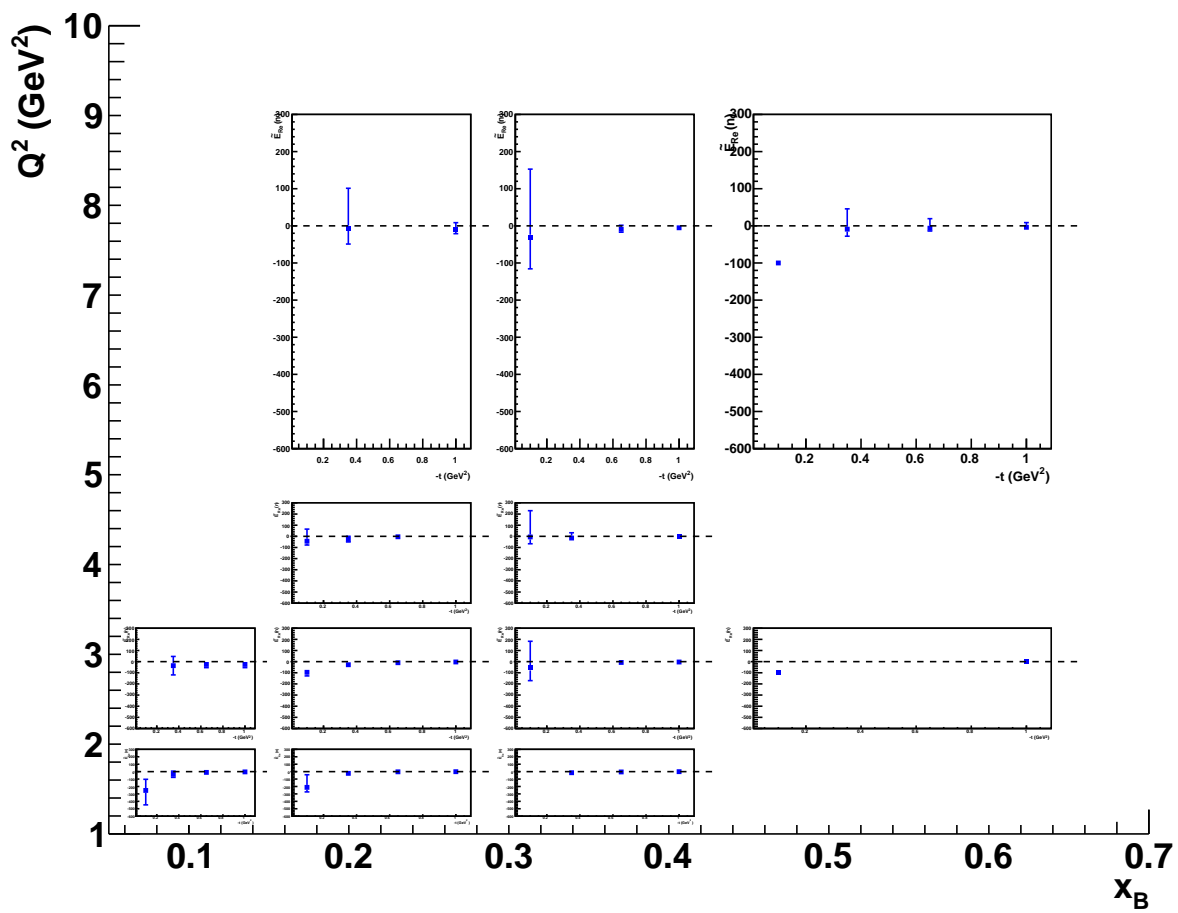


Figure 3.42: $\tilde{E}_{Re}(n)$ as a function of $-t$, for each bin in Q^2 and x_B . The y scale is common to all bins. The dashed line marks $y = 0$.

projected results for the pDVCS asymmetries that will be measured with CLAS12 [11], with the neutron CFF that were shown in Section 3.14⁸.

The flavor separation of the CFFs will represent a major step forward towards the unraveling of the contribution of the quarks' angular momentum to the total nucleon spin via Ji's sum rule [2]:

$$\sum_q \int_{-1}^{+1} dx x [H^q(x, \xi, t=0) + E^q(x, \xi, t=0)] = 2 J_{quarks}. \quad (3.33)$$

3.16 Systematic uncertainties

The goal of this experiment is to extract target and double-spin asymmetries, which are ratios of polarized cross sections. In the ratio, polarization-independent terms, such as acceptances, efficiencies, radiative corrections and luminosity, cancel out to a first approximation⁹. Remaining effects could come from the quantities entering in the asymmetry definitions, namely the procedure to evaluate the counts $N^{+(-)}$, the dilution factor, the π^0 contamination, as well as the beam and target polarizations.

Analyses performed at 6 GeV [15, 14] showed that the biggest contributor to the overall systematic uncertainty is the selection of exclusivity cuts adopted to identify DVCS events and the corresponding counts $N^{+(-)}$. This factor contributed about 10% (this and the following percentages for systematics are defined relatively to the average value of the TSA at 90°) to the total systematics uncertainty.

Another source of uncertainty will be the π^0 background estimation, which will depend on the accuracy of the description of the detector acceptance and efficiency and on the model used in the Monte-Carlo simulation to describe the $e n \pi^0(p)$ reaction (see Eq. 32). In order to account for this latter effect, 6-GeV analyses, performed on data taken on a polarized NH₃ target during the eg1-dvcs experiment [15, 14], evaluated this systematic by varying the contribution of the calculated background by ±30% (Section 3.9), and extracting the final asymmetries in correspondence with this increased/decreased background. The total effect turned out to be 4%, and a similar estimation can be assumed for the present experiment on ND₃.

While acceptance effects are expected to cancel in asymmetries, a residual effect could emerge due to the strong variations of the cross section inside the finite-size bins, that can

⁸In the case of E_{Im} , the figure must be taken only as an indication of the potential of the present experiment. In fact the measurement of $E_{Im}(p)$, and its uncertainties, depend strongly on the feasibility of the conditionally approved pDVCS experiment with transversely-polarized target [25].

⁹Afanasev *et al.* [52] have computed the radiative corrections for the DVCS and BH processes on for CLAS kinematics. It was found that, given the strict kinematic cuts adopted to select the final state, the undetected radiated photon can only have small energies. In this case, therefore, the main contribution to the radiative correction comes from spin-independent soft-photon emission that does not affect the polarization observables. The approximation of negligible contribution from the radiative corrections to the BSA, TSA and DSA, compared to the size of the asymmetries, was estimated to be valid at the 0.1% level [52].

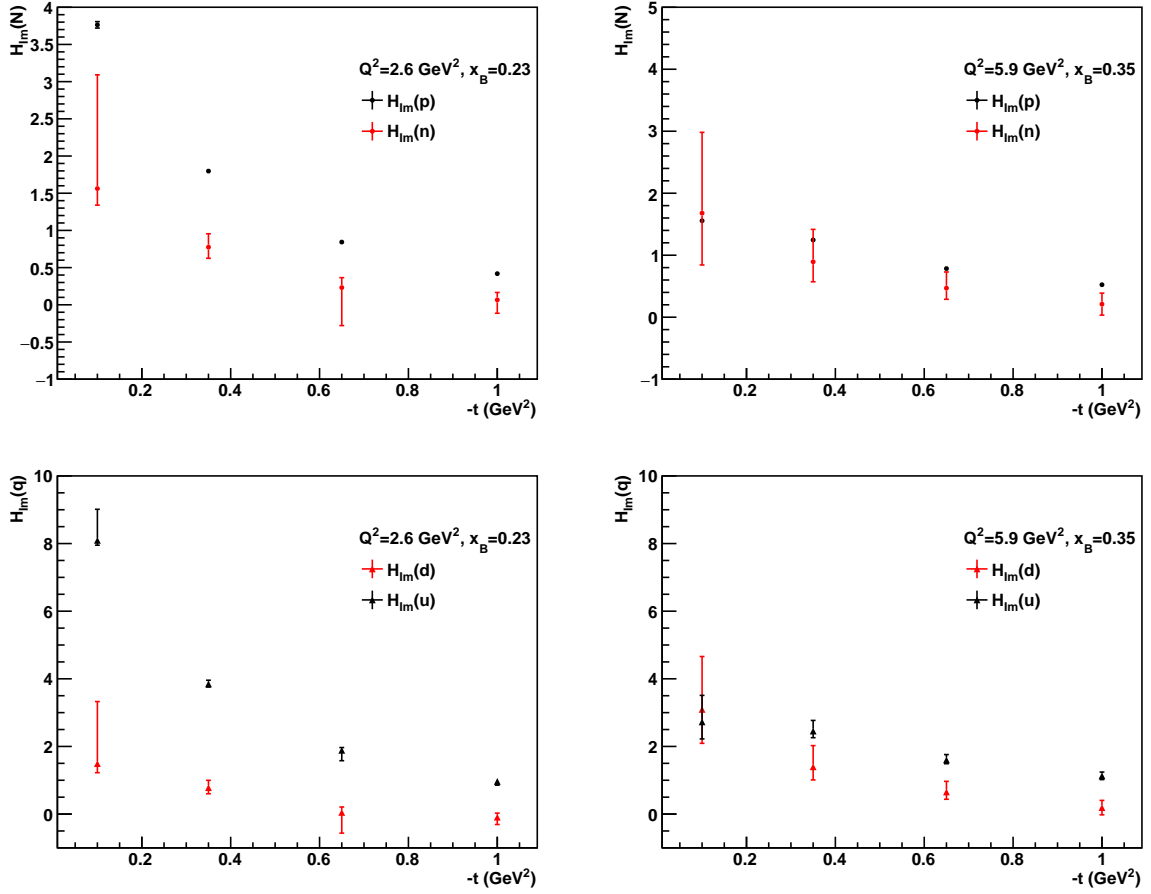


Figure 3.43: Top: $H_{Im}(p)$ (black), extracted from the projection for the approved and conditionally-approved proton-DVCS CLAS12 experiments, and $H_{Im}(n)$ (red), obtained from the projections of the proposed experiment, as a function of $-t$. Bottom: Quark-flavor separated H_{Im} , black for u and red for d . Two different bins in Q^2-x_B , indicated in the legends, are shown in the left and right columns.

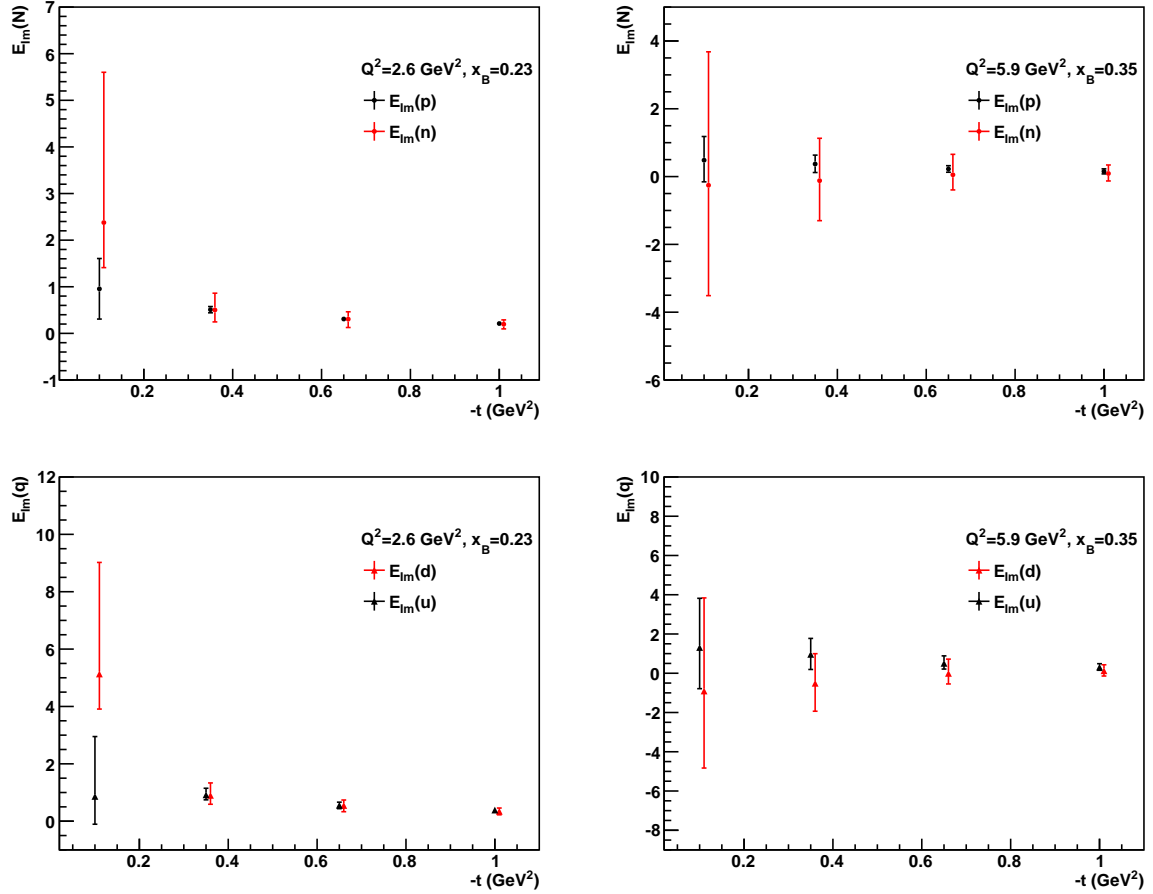


Figure 3.44: Top: $E_{Im}(p)$ (black), extracted from the projection for the approved and conditionally-approved proton-DVCS CLAS12 experiments, and $E_{Im}(n)$ (red), obtained from the projections of the proposed experiment, as a function of $-t$. Bottom: Quark-flavor separated E_{Im} , black for u and red for d . Two different bins in Q^2 - x_B , indicated in the legends, are shown in the left and right columns.

Source of error	Systematic uncertainty
Channel selection cuts	10%
Beam and target polarization	3%-4%
π^0 contamination	4%
Acceptance	1%
Dilution factor	3%
Accidentals	2%
Radiative corrections	Negligible
Total	12%

Table 3.3: Expected systematic uncertainties on the proposed measurement.

lead, in principle, to a non-exact cancellation of acceptance effects from the numerator and the denominator. Such an acceptance effect has been estimated to bring an additional 1% systematic error.

To evaluate the systematic uncertainties linked to the dilution factor determination, in the aforementioned eg1-dvcs pDVCS analysis the asymmetries were computed two more times, taking two different values of the dilution factor: $D_f + \Delta(D_f)$ and $D_f - \Delta(D_f)$, where $\Delta(D_f)$ is the statistical error that was estimated on this quantity. The resulting systematic uncertainties were found to be below the percent level. While studying the systematics on the exclusivity cuts, it was observed that changing the exclusivity cuts induces a variation of the dilution factors much bigger than the variations within the statistical errors described above. It was therefore decided, in order to avoid double-counting and therefore overestimation of systematics, to remove the contribution from the dilution factor computed according to its errors from the total systematic uncertainty. For this proposal, instead, a conservative estimate of the systematic uncertainty on the dilution factor of the order of 3%, consistent with previous assumptions [53], is assumed.

An additional 2% systematic effect is included in the total budget to account for the possible misedentification of neutrons due to accidental coincidences (Section 3.11.)

Finally, uncertainties in the knowledge of the beam and target polarizations (extracted, respectively, via Møller polarimetry measurements and via the NMR system) will propagate into the asymmetry measurements, and are expected to lead to contributions of, respectively, 3% and 4%.

A summary of the systematic uncertainties can be found in Table 3.3. The total systematic uncertainty will be of the order of 12%, averaged over all the kinematic bins (the π^0 -background uncertainty will actually vary depending on the bin).

Production data taking at $10^{35} \text{ cm}^{-2}\text{s}^{-1}$ on ND_3	50 days
Target work	6 days
Production data taking on ^{12}C target	6 days
Moeller polarimeter runs	3 days
Total beam time request	65 days

Table 3.4: Beam-time request for the extension of Run-group Cb.

3.17 Beam-time request

We request 50 new days of beam time for production running on the $^{14}\text{ND}_3$ target with an 11-GeV polarized electron beam, at 10 nA of current. These days will be added to the 50 already allocated for Run Group Cb. In order to acquire the roughly 10% of counts on ^{12}C that are necessary to estimate the dilution factor (Section 3.10) and to remove the nuclear background when studying the exclusivity cuts (Section 3.8.1), and given the maximum tolerable luminosity of CLAS12 of $10^{35} \text{ cm}^{-2}\text{s}^{-1}$, we request 6 additional days of running on a 2-cm-long ^{12}C target, also with a beam intensity of 10 nA. Six days will be spent, with and without beam, in target-related operation, as explained in Section 3.6.1. Including 3 days of Moeller runs to monitor the beam polarization the whole experiment will take 65 days for completion.

3.18 Conclusions

Our knowledge of the three-dimensional structure of the nucleon has become richer in the last few years thanks to the introduction of the formalism of the Generalized Parton Distributions and to the subsequent wealth of experimental results on Deeply Virtual Compton Scattering which have recently become available. After the pioneering experimental results on DVCS, which raised the interest in this reaction as a means to achieve a tomographic description of the nucleon, it became evident, thanks to the analysis of the second generation of proton-DVCS dedicated experiments and to the advancement in the theory and phenomenology of GPDs, how only the combined measurement of several DVCS observables in a vast kinematic space can allow one to disentangle the contributions of the various GPDs and their complex kinematic dependences. While our knowledge of the three-dimensional structure of the proton is progressing considerably - the first attempts at its tomographic description have recently been made thanks to CLAS data taken at 6 GeV [14, 22], and a vast experimental program of pDVCS is planned for JLab at 12 GeV - neutron GPDs remain a mostly virgin field at this stage. The importance of extracting neutron CFFs is paramount if we want to ultimately perform a flavor decomposition of the GPDs. We propose here to make the first ever nDVCS measurements of spin observables, target- and double-spin asymmetries, with a polarized target. We view the experiment as complementary to E12-11-003, which will measure the beam-spin asymmetries for nDVCS at the same kinematic

points, and which is currently listed as a "high-impact" 12 GeV experiment. The detector system will not require additions nor upgrades with respect to components which are currently under construction or already completed. The polarized target is already being developed and will be used also for other CLAS12 experiments. The expected statistical precision and coverage for TSA and DSA that can be achieved with 100 days of beam time will allow us to extract, fitting them together with the BSA from E12-11-00, various neutron Compton Form Factors in a model-independent way. Quark-flavor separation will be obtained by the linear combination of these neutron CFFs with the proton CFFs extracted from the pDVCS CLAS12 experiments.

Bibliography

- [1] D. Müller, D. Robaschik, B. Geyer, F.-M. Dittes, and J. Horejsi, *Fortschr. Phys.* **42** (1994) 101.
- [2] X. Ji, *Phys. Rev. Lett.* **78** (1997) 610; *Phys. Rev. D* **55** (1997) 7114.
- [3] A.V. Radyushkin, *Phys. Lett. B* **380** (1996) 417; *Phys. Rev. D* **56** (1997) 5524.
- [4] J.C. Collins, L. Frankfurt and M. Strikman, *Phys. Rev. D* **56** (1997) 2982.
- [5] K. Goeke, M. V. Polyakov and M. Vanderhaeghen, *Prog. Part. Nucl. Phys.* **47** (2001) 401.
- [6] M. Diehl, *Phys. Rept.* **388** (2003) 41.
- [7] A.V. Belitsky, A.V. Radyushkin, *Phys. Rept.* **418** (2005) 1.
- [8] S. Niccolai, V. Kubarovskiy, S. Pisano, and D. Sokhan, JLab experiment E12-11-003.
- [9] A.V. Belitsky, D. Müller, A. Kirchner, *Nucl. Phys. B* **629** (2002) 323-392.
- [10] M. Guidal, *Eur. Phys. J. A* **37** (2008) 319; M. Guidal, H. Moutarde, *Eur. Phys. J. A* **42** (2009) 71.
- [11] M. Guidal, H. Moutarde, M. Vanderhaeghen, *Rep. Prog. Phys.* **76**, 066202 (2013).
- [12] M. Vanderhaeghen, P.A.M. Guichon, M. Guidal, *Phys. Rev. D* **60**, 094017 (1999).
- [13] M. Guidal, M. V. Polyakov, A. V. Radyushkin and M. Vanderhaeghen, *Phys. Rev. D* **72**, 054013 (2005).
- [14] S. Pisano *et al.*, *Phys. Rev. D* **91**, 052014 (2015).
- [15] E. Seder *et al.*, *Phys. Rev. Lett.* **114**, 032001 (2015).
- [16] F.-X. Girod *et al.*, *Phys. Rev. Lett.* **100**, 162002 (2008).
- [17] S. Chen *et al.*, *Phys. Rev. Lett.* **97**, 072002 (2006).
- [18] M. Mazouz et al., *Phys. Rev. Lett.* **99**, 242501 (2007).

- [19] C. Muñoz Camacho *et al.* (Hall-A Collaboration), Phys. Rev. Lett. **97**, 262002 (2006).
- [20] S. Stepanyan *et al.* (CLAS Collaboration), Phys. Rev. Lett. **87**, 182002 (2001).
- [21] A. Airapetian *et al.* (HERMES Collaboration), JHEP06 **0806**, 066 (2008); A. Airapetian *et al.* (HERMES Collaboration), JHEP **06**, 019 (2010).
- [22] H.-S. Jo *et al.*, arXiv:1504.02009 [hep-ex].
- [23] C. Hyde-Wright, B. Michel, C. Munoz Camacho and J. Roche, JLab experiment E12-06-114.
- [24] F. Sabatié, A. Biselli, V. Burkert, L. Elouadrhiri, M. Garçon, M. Holtrop, D. Ireland, K. Joo, W. Kim, JLab experiment E12-06-119.
- [25] L. Elouadrhiri, H. Avakian, V. Burkert, M. Guidal, M. Lowry, L. Pappalardo, and S. Procureur, JLab experiment E-12-12-010, conditionally approved.
- [26] C. Munoz Camacho, C. Hyde-Wright, P.-Y. Bertin, JLab experiment E07-007.
- [27] C. Munoz Camacho, R. Paremuzyan, T. Horn, JLab experiment E12-13-010.
- [28] C.H. Hyde, P.-Y. Bertin, A. Camsonne, JLab Experiment E08-025.
- [29] Technical Design Report of the CLAS12 Forward Tagger, <http://www.ge.infn.it/~batta/jlab/ft-tdr.2.0.pdf>.
- [30] St. Goertz, W. Meyer, and G. Reichertz, Progress in Particle and Nuclear Physics **49** (2002) 403.
- [31] G.R. Court, D.W. Gifford, P. Harrison, W.G. Heyes, and M.A. Houlden, Nucl. Instr. Meth. **A 324**, 433 (1993).
- [32] G.R. Court, *et al.*, Nucl. Instr. Meth. **A 527**, 253 (2004).
- [33] C. Dulya, *et al*, Nucl. Instr. and Meth. **A 398** (1997) 109.
- [34] N. D. Kwaltine, PhD thesis, University of Virginia, 2013.
- [35] K. Slifer, “Proceedings of the 12th International Workshop on Polarized Ion Sources, Targets, and Polarimetry”, Upton, NY (2007) 330.
- [36] P. McKee, Nucl. Instr. Meth. **A 526**, 60 (2004).
- [37] R.T. Giles *et al.*, Nucl. Instr. Meth. **A 252**, 41 (1986).
- [38] E. Smith *et al.*, Nucl. Instr. Meth. **A 432**, 265 (1999).

- [39] V. Baturin *et al.*, Nucl. Instr. Meth. **A** **562**, 327 (2006).
- [40] M. Ungaro, private communication.
- [41] J.B. Birks, Proc. Phys. Soc. **A64**, 874 (1951).
- [42] D. Sokhan, <http://clasweb.jlab.org/wiki/index.php/Daria> .
- [43] S. Niccolai, [http://clasweb.jlab.org/rungroups/e1-dvcs/wiki/index.php/CLAS12_neutron_detector:update on simulation](http://clasweb.jlab.org/rungroups/e1-dvcs/wiki/index.php/CLAS12_neutron_detector:update_on_simulation) (September 2008).
- [44] A. El Aloui and E. Voutier, CLAS-NOTE 2009-024.
- [45] H. Avakyan, private communication.
- [46] M. Lacombe et al., Phys. Rev C **21** (1980) 861.
- [47] D. Sokhan, analysis underway.
- [48] P. Bosted <https://www.jlab.org/Hall-B/secure/eg1-dvcs/bosted/Exclusive/exclnote.pdf>.
- [49] R. De Vita, private communication.
- [50] A. Avakian *et al.*, JLab conditionally approved proposal C12-11-111.
- [51] S. Procureur, private communication.
- [52] A.V. Afanasev *et al.*, J. Exp. Theor. Phys. **102**, 220 (2006).
- [53] S. Kuhn, A. Deur, V. Dharmawardane, K. Griffioen, D. Crabb, Y. Prok, T. Forest, Jefferson Lab Experiment E12-06-109.
- [54] <https://www.jlab.org/Hall-B/clas12-web/clas12-expt1.jpg>.